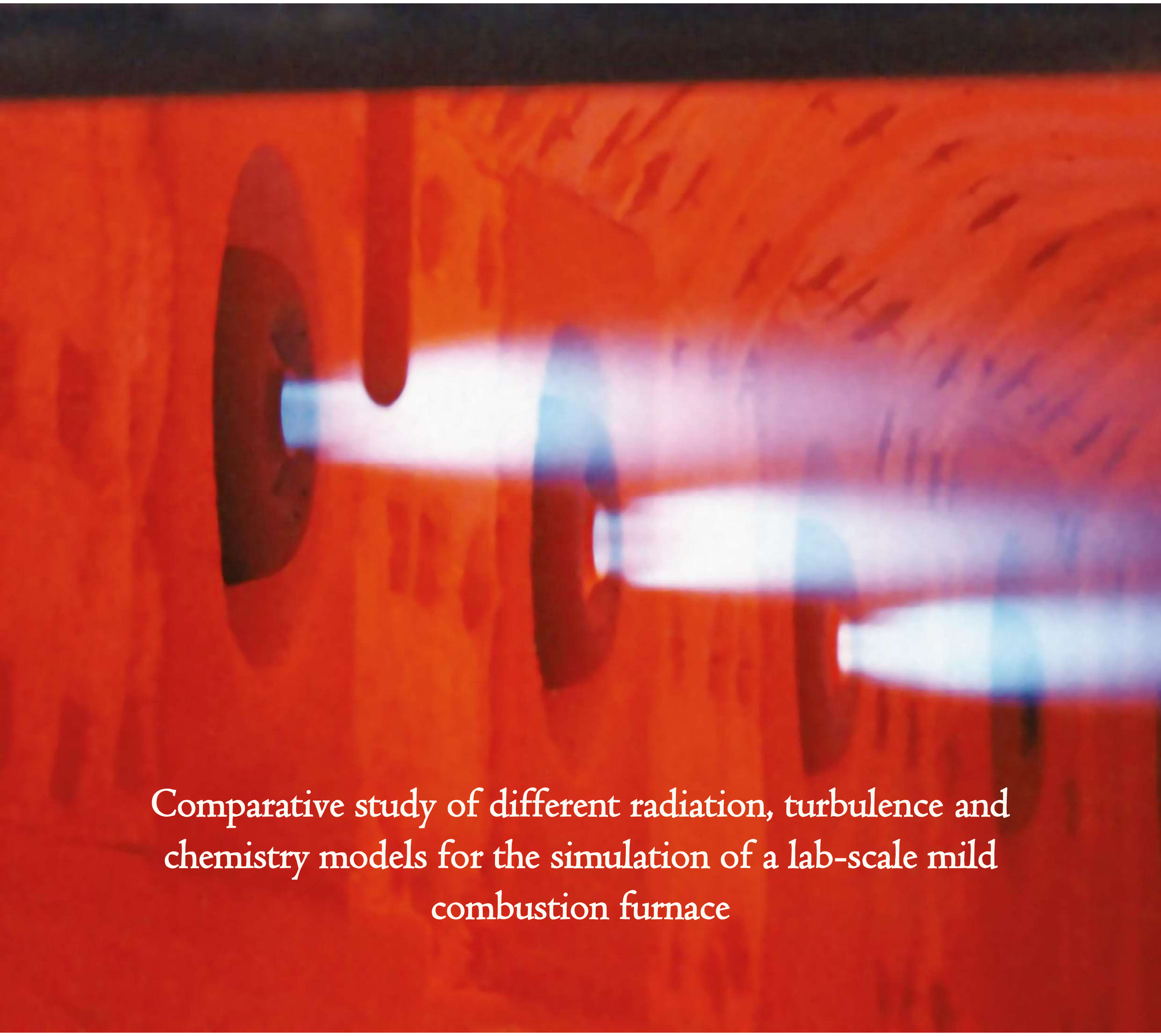

Comparative study of different radiation, turbulence and chemistry models for the simulation of a lab-scale mild combustion furnace

Georgios Alexandros Desypris

M.Sc. Mechanical Engineering

Report number: 3034

TU Delft

COMPARATIVE STUDY OF DIFFERENT RADIATION, TURBULENCE AND CHEMISTRY MODELS FOR THE SIMULATION OF A LABSCALE MILD COMBUSTION FURNACE

by

Georgios Alexandros Desypris

in partial fulfillment of the requirements for the degree of

Master of Science
in Mechanical Engineering

at the Delft University of Technology,
to be defended publicly on Friday November 20, 2020 at 14:00 AM.

Supervisor:	Prof. Dr. D.J.E.M. Roekaerts
Co-supervisor:	Ir. S. Silvestri
Thesis Commitee:	Dr. D. J. P. Lahaye
	Dr. Ir.M. J. Tummers

To my lovely sister, Ira
and my parents, Stefanos and Apostolia

ACKNOWLEDGEMENTS

On the very outset of this report, I would like to acknowledge the contribution of some people, who were always supporting me in this endeavor. This project required a large amount of work and dedication, however I would not be able to deliver it without their assistance, support and supervision.

First and foremost, I would like to express my honest gratitude to my supervisor Professor D.J.E.M. Roekaerts. His supervision was always beneficial and constructive, he was always available and understanding. His knowledge and his ability to explain all kinds of complex concepts, aided me in tackling all the demanding problems that I faced. Moreover, I would like to specifically mention that his feedback was pivotal for the completion of this project.

Additionally, I would like to thank my daily supervisor Simone Silvestri, for being a great mentor and friend. I honestly appreciate the time he devoted the past months, as well as his insights on my research. His supportiveness and advice helped me to overcome problems related to my thesis, as well as my personal life and motivated me to keep working.

Furthermore, I would like to extend a special thanks to my friends, for making this period more exciting and for me, as well as giving me courage until the end of this journey. Lastly, I would like to thank my parents and my sister for their unconditional support in every step of my life.

Georgios Alexandros Desypris
Delft, November 2020

ABSTRACT

Flameless combustion, or MILD combustion is a technology that enables stable combustion with high efficiency while maintaining very low NOx and soot emissions. It is characterized by uniform heat flux and can be achieved when fuel and preheated oxidant jets are mixed into a strong recirculating flow. It is a complex process which combines multiple physical phenomena such as, heat transfer and reactions in a turbulent flow and is difficult to capture numerically via simple Computational Fluid Dynamics (CFD) simulations. Therefore, appropriate turbulence, chemistry, radiation and turbulence-chemistry interaction models are required to address this combustion regime via computational modeling.

The present work tries to tackle this issue by conducting a comparative study of different radiation, turbulence and chemistry models for the simulation of a lab-scale MILD combustion furnace using RANS CFD simulations. This assessment was conducted in two steps. Firstly, the importance of radiative heat transfer in furnaces was investigated, by simulating an axisymmetric oxycombustion furnace using advanced radiation models. The SLW, Domain-based WSGG and Cell-based WSGG models were evaluated using simple chemistry and turbulence models. The results were validated based on the work of Webb et al and experimental results. It was concluded that detailed simulation of the radiative gas properties is important and directly influences the resulting temperature field, especially in the bulk flow region. Secondly, a detailed evaluation of a Dutch natural gas fired Delft lab-scale furnace that is operating in MILD combustion was conducted. For the turbulence modeling, the Standard, the Modified Standard, the Realizable $k-\varepsilon$ and the $k-\omega$ SST Models were compared firstly qualitatively, based on velocity and reaction field contours, and secondly, quantitatively, based on available LDA velocity measurements. The influence of the chemistry modeling was evaluated in two parts. Firstly, the qualitative effect of changing the C_ξ constant of the EDC model on temperature and reaction zones of the GRI-Mech 3.0, the DRM-19, the KEE58 and Chen mechanisms, was investigated. And secondly, the quantitative effect on the use of the GRI-Mech 3.0, the KEE58, Chen and Lu-30, based on CARS temperature measurements was researched. Lastly, the influence of the radiation model was investigated qualitatively and quantitatively using the standard 1-RTE domain based WSGG, a 4-RTE WSGG, a cell-based WSGG and the SLW model.

Out of the mechanisms coupled with the EDC, the GRI-Mech 3.0 performs well. Of the radiative properties models the domain based WSGG performs worse compared to the other models. The cell based WSGG performs similarly to the more advanced spectral and non-grey (4-RTE) models and has lower computational cost. For these reasons, the best overall combination for the studied flameless furnace is found to be the combination of Standard $k-\varepsilon$ model, standard EDC with GRI-Mech 3.0 and cell based WSGG.

CONTENTS

LIST OF FIGURES

NOMENCLATURE

Abbreviations

ALBDF	Absorption Line Blackbody Distribution function
CB	Cell Based
CDSD	Carbon Dioxide Spectral Databank
CFD	Computational Fluid Dynamics
DB	Domain Basted
DNS	Direct Numerical Simulation
DO	Discrete Ordinates Radiation Model
DTRM	Discrete Transfer Radiation
E-EDV	Extended EDC
EDC	Eddy Dissipation Model
EDM	Eddy Dissipation Moldel
FLOX	Flameless Oxidation
HiTAC	High Temperature Air Combustion
HiTEMP	High Temperature
JHC	Jet in Hot Coflow
LBL	Line-By-Line calculations
LES	Large Eddy Simulation
MILD	Moderate and Intense Low-oxygen Dilution combustion
NBM	Narrow Band Models
NE-EDC	New Extended EDC
PaSR	Partially Stirred Reactor
PEA	Partial Equilibrium Approximation

PFR	Plug Flow Reactor
PSR	Perfectly Stirred Reactor
QSSA	Quasi-Steady State Approximation
RANS	Reynolds Averaged Navier Stokes
RTE	Radiative Transfer Equation
SIMPLE	Semi Implicit Method for Pressure Linked Equations
SLW	Spectral-Line Weighted-sum-of-gray-gases
SST	Shear Stress Transport
TCI	Turbulence Chemistry Interaction
TRI	Turbulence Radiation Interaction
UDF	User Defined Function
WBM	Wide Band Models
WSGG	Weighted-Sum-of-Grey-Gases

Greek Symbols

α_η	spectral absorptivity
α_j	grey gas weight
α_l	species thermal diffusivity
$\beta_{j,i}$	polynomial coefficients
κ	absorption coefficient
κ_j	grey gas absorption coefficient
λ	thermal conductivity
μ	dynamic viscosity
μ_t	turbulent viscosity
ν_T	kinematic eddy viscosity
$\nu''_{j,r}$	reverse reaction species stoichiometric coefficient
$\nu'_{i,r}$	stoichiometric coefficient
Ω	solid angle

ρ	density
σ_k	turbulent Prandtl numbers for k
σ_ε	the turbulent Prandtl numbers for ε
τ^*	residence time
θ	zenith angle
ε	dissipation of the turbulent kinetic energy
φ	azimuthial angle
φ_g	gas thermodynamic state
ξ^*	size of the fine structure
δ_{ij}	Kronecker symbol
κ_η	spectral absorption coefficient
ω_k	angular velocity
Φ_η	scattering phase function
$\sigma_{s\eta}$	scattering constant
ε_{ijk}	Levi-Civita symbol
$\dot{\omega}_k$	molar species chemical production rate

Roman Symbols

$\dot{Q}$	radiative heat source
$\mathscr{A}$	absorptance
$\mathscr{R}$	reflectance
$\mathscr{T}$	Transmittance
$\mathrm{Sc}_{\mathrm{t,k}}$	turbulent Schmidt number
Pr_t	turbulent Prandtl number
A	area
C	species molar concentration
c	speed of light
$D_{k,i}$	mixture mass diffusion coefficient

D_{kl}	binary diffusion constant
E	emissive power
e	energy
E_b	monochromatic emissive power
h	enthalpy
h_k	specific enthalpy
I	radiative intensity
I_b	blackbody intensity
k	kinetic energy
L_e	the corrected effective mean beam length
M	mean molecular weight of the gas mixture
m	total mass of the gas
m_k	mass of the species
$M_{w,i}$	molecular weight of reactant
n	refractive index of midium
p	pressure
P_k	production of turbulent kinetic energy
q_i	energy flux
R	ideal gas constant
r	reaction
s	path length
T	temperature
u_i	three dimensional velocity field
V	volume
v	frequency
$V_{k,i}$	diffusion velocity of a species
w_i	quadrature weights associated with directions
X	mole fraction

Y	mass fraction
Y_i^*	fine-scale species mass fraction
Y_k	mass fraction
$\hat{s}_i$	discrete direction
$\hat{s}_j$	vector direction
C_{pk}	specific heat at constant temperature
S_{ij}	mean strain rate
$S_{k,chem}$	rate of production species
u_i	velocity of the center of mass
U_{cl}	centerline velocity
$u_{k,i}$	species valocity
$V_{k,i}$	diffusion velocity
$f_{k,j}$	net body force

Superscript

$*$	fine structure
-	Reynolds decomposition mean value
~	Favre averages mean value

Subscript

η	wavenumber
v	local
b	black body
g	gas
i	i-th component
k	species
loc	local
m	m-th component
ref	reference
y	y-th component

1

INTRODUCTION

Societies have an ever increasing need for more energy, year by year. This increasing energy production has supported the continuous population growth and industrialization around the globe. According to the International Energy Agency [1], most of this energy originates from fossil fuels in 2020. The Agency estimates that up to 2040, more than 60 % of the total worldwide energy production will continue to be produced by fossil fuels. Renewable energy has been recently a hot topic, and great strides in R&D have been made in this regard; however, due to the abundance of fossil fuels and limitations of renewables, fossil fuel consumption is not projected to end in the foreseeable future [2].

Fossil fuels have been used since antiquity, however only recently, since the Industrial revolution of the 19th, century combustion systems have been developed and researched. The efficiency of all combustion systems has been improving for decades and nowadays, it is significantly higher compared to renewable sources of energy. However, the use of fossil fuels comes at the great cost of pollution. Combustion products over time directly affect the public health and cause environmental issues. Pollution due to carbon emissions, was noted, as early as, the early industrialization of England. Excessive use of fossil fuels in the last century is directly linked to phenomena such as acid rain, smog and, of course, the greenhouse effect. Acid rain for example, is caused by nitrogen emissions that are mainly produced due to high temperatures in combustion applications.

Governments have raised great concern about the pollutants issue. The Paris Agreement is the most recent attempt to counter the environmental changes due to fossil fuel emissions through a “nationally determined contributions” policy. In 2016, in Paris, 196 countries agreed to increase the effort to keep the increase in global average temperature to well below 2 ^{o}C. The European Union in particular targets a 40% reduction in pollutant emissions compared to 1990, by 2030 [3].

Another general consensus is, that fossil fuel use cannot be halted overnight. Renewable energy systems based on wind and solar energy, are still not mature technologies and have intermittent energy production. Batteries are very expensive and other energy storage technologies are not proven in larger scales. A interim solution is to use the fossil fuel energy more efficiently and lower the emissions, while gradually transitioning to renewable sources. Therefore, apart from the research in renewable energy, some emphasis should be given in the optimization of current combustion systems. At the same time, introduction of other eco-friendly fuels for combustion can be also be investigated, such as bio-fuels or synthetic natural gas.

1.1. MILD COMBUSTION

Moderate and Intense Low-oxygen Dilution combustion, or in short MILD combustion is a modern and promising process that is commonly identified by the absence of a visible flame and is often called Flameless combustion. It is characterized by well-distributed chemical reactions that yield low temperature gradients, high stability, low NO_x and soot emissions and low acoustic oscillations. It is also highly efficient compared to ordinary flames due to flue gas recirculation [4].

This process, was firstly identified by Wünning and Wünning et al [5], when conducting experiments in a self recuperative burner in an enclosed furnace, and was termed Flameless Oxidation or, FLOX®. The core parameter of this study was the recirculation rate, defined as the mass flow rate of the internal recirculation gas over the total mass flow. For the methane experiments that were conducted, it was found that MILD combustion is only stable if the recirculation rate is over 3 and the furnace temperature is larger than 800 ^oC. Another early study was conducted by Katsuki et al [6], and focused on the fact that the process requires the inlet temperature of reactants to be higher than autoignition temperature of the mixture. For this reason it was named High Temperature Air Combustion, or HiTAC. The most used definition for this regime was proposed by Cavaliere and de Joannon et al [7]. They defined the term MILD combustion as the process that takes place "when the inlet temperature of the reactant mixture is higher than the mixture self-ignition temperature, whereas maximum allowable temperature increase with respect to inlet temperature during combustion is lower than mixture self-ignition temperature". While this definition is straightforward for premixed flames, it cannot be easily applied in non-premixed systems. In these systems, the inlet temperature is normally lower than the auto ignition temperature. The hot burnt gas preheats the oxidizer and the fuel to autoignition temperature. Such a case was clearly demonstrated by Kumar et al [8].

The MILD combustion regime operates presently on the principles of heat and flue gas recirculation. The recirculation of hot combustion products dilutes the oxidizer locally and increases the temperature of the reactants. This results in slowing down the reactions and ultimately leads to a well-distributed reaction zone. At some point, the amount of inert flue gases introduced by the recirculation is sufficient to alter the structure of the reaction zone which reaches the flameless combustion regime. Autoignition sustains the regime, which operates robustly, and distribution of release heat to a larger volume is achieved. This in turn results into a nearly uniform temperature distribution with reduced peak temperatures. As a consequence, the net radiation flux can be enhanced by as much as 30% compared to other regimes [9], and NO emissions are significantly lower than those produced by conventional flames, where the heat release of the reactions is mainly located in a thin flame front. Another benefit of this combustion regime is the elimination of "hot spots" in the combustion chamber and thus, quality of production can be improved in some industrial applications. For this reason MILD combustion can find potential application in the steel industry, ceramic industry, glass industry, chemical industry, combined heat and power, and gas turbines.

1.2. RESEARCH OBJECTIVES

The aim of this thesis is the formulation and evaluation of a comprehensive model for MILD combustion, through the use of Computational Fluid Dynamics (CFD). Since heat distribution is one of the core components of MILD combustion, the importance of accurate radiation treatment will also be investigated. The present work tries to achieve this goal by assessing the role of several closure models, in order to simulate the flameless labscale furnace of [10] using the Reynolds-Averaged Navier–Stokes formulation. A set of different radiation, turbulence and chemistry models will be evaluated qualitatively and quantitatively based on the experimental results.

1.3. THESIS OUTLINE

Chapter 2 introduces all the relevant theory that is required in order to understand the concepts behind the models. Firstly, the governing equations of a reacting flow are described. Then the models that were used to simulate those governing equations are presented and briefly described.

Chapter 3 presents a simulation of an axisymmetric oxycombustion furnace. In this case advanced radiation models are evaluated using simple chemistry and turbulence models.

Chapter 4 presents a comparative study of different radiation, turbulence and chemistry models for the simulation of a lab-scale MILD combustion furnace using RANS CFD simulations.

Chapter 5 makes a summary of the conclusions that were derived after the simulations and provides an outlook for further developments.

2

THEORY

Fluid mechanics draw conclusions about the motion of fluids using laws of physics and classic mechanics, by investigating the fluid flow in the macroscopic scale. Based on these laws, quantities are always conserved. The mass and momentum conservation of the fluid, the energy conservation, as well as the second law of thermodynamics, in conjunction with material balances, are employed in order to calculate the fluid's properties of interest. Simple flows can be described in a well-established manner using the Euler equation or the Bernoulli equation. However, in the case of reacting and turbulent flows more complex equations must be implemented in order to encapsulate the entirety of the phenomena.

In order to describe these phenomena, Computational Fluid Dynamics (CFD) is usually employed. CFD is the analysis of fluid flows using numerical solution methods since it is impossible to resolve the flow analytically. By using CFD, the analysis of complex problems involving fluid-fluid, fluid-solid or multiphase interaction is possible. This method of analysis is based on the discretization of the involved equations and their transformation into algebraic equations that are easier to efficiently solve numerically. These numerical schemes are then resolved by using iterative methods. With the rise of computing power in modern computing systems, better and better solutions are achieved, which are often required to tackle the most complex problems in all kinds of industries.

2.1. GOVERNING EQUATIONS

Firstly, it is important to understand the different equations that the computational fluid dynamic solvers have to solve. The conservation equations for reacting flows involve the conservation of mass, momentum and energy, as well as the conservation of species. It is important to note that the conceptual study of combustion requires the multidisciplinary understanding of thermodynamics, fluid dynamics and mechanical systems, as well as chemistry. In this brief overview the governing equations in combustion applications will be provided ([11], [12], [13]).

2.1.1. MULTI-COMPONENT MIXTURES

Reacting gases that participate in combustion involve a multitude of different species that transform through multiple chemical reactions. These species are usually expressed by mass fractions Y_k for $k = 1$ to N, where N is the number of different species present in the reacting gases. In turn a mass fraction is defined as:

$$Y_k = \frac{m_k}{m} \tag{2.1}$$

where m_k is the mass of the species k in the given volume V and m is the total mass of the gas inside the volume. The major difference between non-reacting and reacting flows is the number of conservation equations to be solved. In the case of a reactive flow a total of $N+5$ equations must be solved, in order to account for the different species that participate or are being created during the process. Except for those species, the flow variables must be calculated. Those are the density (ρ), the pressure (p), the temperature (T) and the three dimensional velocity field (u_i).

EQUATION OF STATE

In order to calculate all the flow variables an equation of state must be employed. The ideal gas law states:

$$p = \rho \frac{R}{M} T \tag{2.2}$$

where M is the mean molecular weight of the gas mixture and $R = 8.314$ J/(moleK). Since the gas consists of a mixture of species, it is more convenient to express the equation of state for each species separately. The total pressure of a mixture of gases is the sum of all the partial pressures. This can be expressed as:

$$p = \sum_{k=1}^{N} p_k \tag{2.3}$$

the density of each species can be calculated by using the mass fraction as:

$$\rho_k = \rho Y_k \tag{2.4}$$

and in turn the density of the mixture:

$$\rho = \sum_{k=1}^{N} \rho_k \tag{2.5}$$

Thus, the ideal gas law for each species can be expressed as:

$$p_k = \rho_k \frac{R}{M_k} T \tag{2.6}$$

Finally, the mean molecular weight is defined as:

$$M = \sum_{k=1}^{N} \frac{M_k}{Y_k} \tag{2.7}$$

and thus, the ideal gas law can be described as:

$$p = \rho R T \sum_{k=1}^{N} \frac{Y_k}{M_k} \tag{2.8}$$

2.1.2. MASS CONSERVATION

The mass conservation of a fluid is governed by the continuity equation. Therefore, for a fluid with three dimensional velocity components (for $i = 1$ to 3):

$$\frac{\partial \rho}{\partial t} + \frac{\partial \rho u_i}{\partial x_i} = 0 \tag{2.9}$$

The first term denotes the rate of change of mass inside the control volume, while the second term the difference between inflow versus outflow.

2.1.3. MOMENTUM CONSERVATION

In continuum mechanics, a Newtonian fluid is considered a fluid whose stress tensor is linear in respect with the strain tensor. Air and the usual combustion gases, i.e. methane, are commonly considered Newtonian fluids. In such fluids the viscous stress tensor is defined as:

$$\tau_{ij} = -\frac{2}{3}\mu \frac{\partial u_k}{\partial x_k}\delta_{ij} + \mu\left(\frac{\partial u_i}{\partial x_j} + \frac{\partial u_j}{\partial x_i}\right) \tag{2.10}$$

where μ is the dynamic viscosity and δ_{ij} is the Kronecker symbol, where $\delta_{ij} = 1$ only when $i = j$ and 0 in all other cases.

After having described the stress tensor in 2.10, the momentum equations can be specified. This equation is more commonly known as the Navier-Stokes equations and describe the motion of any moving fluid. They are derived by applying Newton's second law for a continuum material in an arbitrary infinitesimal fixed control volume. The Navier-Stokes equations are defined as follows:

$$\frac{\partial}{\partial t}\rho u_i + \frac{\partial}{\partial x_j}\rho u_i u_j = -\frac{\partial p}{\partial x_i} + \frac{\partial \tau_{ij}}{\partial x_i} + \rho \sum_{k=1}^{N} Y_k f_{k,j} \tag{2.11}$$

In the left hand side of 2.11 the first term describes the rate of change of momentum, whereas the second term represents the convection of momentum in the control volume.

The first term on the right hand side describes the effect of the pressure force motion due the the normal stresses. The second term captures the effect of the viscous stresses. The shear stress is responsible for turbulence and viscous flows e.g. creeping flows. Lastly, the final term represents the body forces. The net body force acting on a species k in the direction of j is $f_{k,j}$.

However, combustion directly influences the solution of the Navier-Stokes equations by changing density and dynamic viscosity. Density varies in a ratio from 1:8 to 1:10 and rapid expansion happening on the flame fronts increases all velocities by roughly the same ratio. Moreover, the dynamic viscosity also varies by the same ratio because of the temperature increase [11].

2.1.4. SPECIES CONSERVATION

During combustion reactants are consumed and new species are formed, which in turn can also be consumed to form the final products. The mass conservation of each species k is governed by:

$$\frac{\partial \rho Y_k}{\partial t} + \frac{\partial \rho u_i Y_k}{\partial x_i} = -\frac{\partial J_i^k}{\partial x_i} + S_{k,\text{chem}} \tag{2.12}$$

The first term on the left hand side of the equation describes the rate of the change of mass of a species k while the second term the convective transfer of its mass due to the fluid flow. On the left hand side the first term represents the species diffusion and is defined as:

$$J_i^k = \rho V_{k,i} Y_k \tag{2.13}$$

The diffusion velocity of a species k is defined as $V_{k,i} = u_{k,i} - u_i$ with $u_{k,i}$ the species velocity and u_i the velocity of the center of mass. The last term is known as the chemical production rate for a species k and is related to the molar species chemical production rate $\dot{\omega}_k$ as $S_{k,chem} = M_k \dot{\omega}_k$.

2.1.5. ENERGY CONSERVATION

In order to express the energy conservation in reacting flows, an awareness of the different effects that contribute to heat flux must be raised. The heat flux in the flow field is described from Fourier's law of heat conduction. However, there are two more effects that can contribute to the total heat flux in such systems. The first such contribution is called the interdiffusion heat flux ($q_{\text{interdiffusion}}$). This heat flux is created due to the natural diffusion of species in the flow field. When the average velocity of a specie k is different that the bulk velocity of the flow, diffusion of k occurs relative the the bulk mass of the mixture. In this case, there is an extra enthalpy flux carried by the k molecules that must be added. The second contribution is the energy flux created as a coupled effect of irreversible process due to the species concentration gradient. This phenomenon is called the Dufour effect and results in a temperature differences. In most cases this effect is very small and it is almost negligible in applications with flames. However, it will be presented for completeness. Thus the energy flux is:

$$\begin{aligned} q_i &= q_{\text{conduction}} + q_{\text{interdiffusion}} + q_{\text{Dufour}} \\ &= -\lambda \frac{\partial T}{\partial x_i} + \rho \sum_{k=1}^{N} h_k Y_k V_{k,i} + R_u T \sum_{k=1}^{N} \sum_{l=1}^{N} \left(\frac{C_l \alpha_l}{M_k D_{kl}} \right) (V_{k,i} - V_{l,i}) \end{aligned} \tag{2.14}$$

Here it must be noted that additional heat flux due to radiation is usually included as a volumetric heat source term. The specific enthalpy h_k is the sum of sensible and chemical enthalpy:

$$h_k = \int_{T_o}^{T} C_{pk} dT + \Delta h_{f,k}^{o} \tag{2.15}$$

where C_{pk} is the specific heat at constant temperature. The specific heat is also a function of temperature and it is usually computed by using empirical polynomial equations for different species.

Moreover, in equation 2.14, λ is the thermal conductivity, C is the species molar concentration, α_l is the species thermal diffusivity and D_{kl} is the binary diffusion constant.

With the heat fluxes defined, the total energy equation can be expressed by applying the conservation of energy for the fluid contained within a control volume:

$$\frac{\partial}{\partial t}\rho e + \frac{\partial}{\partial x_i}\rho u_i e = -p\frac{\partial u_j}{\partial x_j} - \frac{\partial q_i}{\partial x_i} + \tau_{ij}\frac{\partial u_i}{\partial x_j} + \dot{Q} + \rho\sum_{k=1}^{N} Y_k f_k V_{k,i} \tag{2.16}$$

The left hand side represents the increase of internal energy. The first term describes the rate of change of energy while the second term the transport of energy by the flow. On right hand side the first term expresses the work of the flow and the second term the heat flux in all spatial directions. The third term represents the dissipation created due to the viscous stresses in the flow and the fourth term any volumetric heat source (such as a radiation source). Lastly, the final term represents the work of body forces.

By using the definition of specific enthalpy $h = e + \frac{p}{\rho}$ the energy conservation equation can be presented in terms of enthalpy:

$$\frac{\partial}{\partial t}\rho h + \frac{\partial}{\partial x_i}\rho u_i h - \frac{\partial p}{\partial x_j} = \tau_{ij}\frac{\partial u_i}{\partial x_j} + \dot{Q} - \frac{\partial q_i}{\partial x_i} + \rho\sum_{k=1}^{N} Y_k f_k (V_{k,i} + u_i) \tag{2.17}$$

Since the specific enthaply as presented in 2.15 is only a function of temperature due to the fact that the ideal gas assumption was made, there are five conservation equations for the six variables presented in 2.1.1. Adding to those the ideal gas law (2.8), as well as the different species equations the system of equations can be resolved and thus, closed.

2.1.6. RADIATIVE TRANSFER

In the previous section, the heat source was mentioned as an input (or output) of energy into the energy equation in the form of radiation. As it is well known, the three modes of heat transfer are conduction, convection and radiation. However, there is a distinguishing feature between radiation and the other modes of heat transfer. Radiation exhibits a temperature dependency generally proportional to the fourth power, a fact that makes radiation more important in higher temperatures and even dominant in the very high temperatures which usually occur in combustion applications. This distinction lies with the way that molecules interact in the different modes of heat transfer. Normally, convection and conduction are local phenomena that stem from the collision between molecules, which is then translated into energy transfer. This in turn, enables the assumption that energy balances can be performed by using infinitesimally small volumes. Radiation however, transfers energy in the form of quanta (photons), which can travel from the range of atomic to cosmological distances, thus enabling us to observe the universe billions of light years away. In this context, it is impossible to confine the description of this mode of energy transfer to infinitesimal volumes and the entirety of the control volume must be considered.

Another layer of complexity that can be added when considering heat transfer via radiation, is the differences exhibited by the properties of radiative materials. While properties such as thermal conductivity and kinematic viscosity, relevant for conduction and convection, are usually well understood and described, radiative properties behave erratically and measuring them has proven challenging. More particularly, in gases, all radiative properties usually vary with wavelength thus, introducing the need to add another dimension to equations that govern radiation. Therefore, one can say that the analysis of radiative transfer is critical for combustion applications. The theory presented in the next sections is based on [14],[15],[16].

ELECTROMAGNETIC SPECTRUM

Radiative energy, as mentioned above, is the transfer of energy in the form of quanta. These can be conceptualized as electromagnetic waves or energy packets named photons. Photons travel at the highest possible depending on the medium in which they travel. In the case of vacuum, photons travel at the speed of light. In all other mediums photons travel with lower speeds, inversely proportional to the refractive index of the medium (n). Photons and waves in general are described by measuring their frequencies. Instead, waves can also be described using the:

frequency (ν)	-	units in Hz
wavenumber (η)	-	units in cm^{-1}
wavelength (λ)	-	units in μm

The relationship between the aforementioned quantities is:

$$\nu = \frac{c}{\lambda} = c\eta, \tag{2.18}$$

where c is the speed of light though a medium with refractive index n. Here, it must be stated that if light changes medium (i.e. from air to water), its frequency must remain constant due to energy conservation. This is not true however for the wavenumber and wavelength, since they depend on the speed of light and thus, the refractive index of the media.

The wavenumbers of electromagnetic radiation vary over a very large spectrum, which is promptly named the electromagnetic spectrum. Different wavenumbers have slightly different behaviour, however they can be grouped in a number of categories that are presented in Figure 2.1. The part of the spectrum that is important for radiative heat transfer is between 10^2 and $10^6\mathrm{cm}^{-1}$, (ultra-violet to near infrared) here labeled as the thermal radiation range.

EMISSIVE POWER

The interaction between electromagnetic waves and matter starts at the matter's surface. The waves hitting the surface of matter, can either be reflected totally,

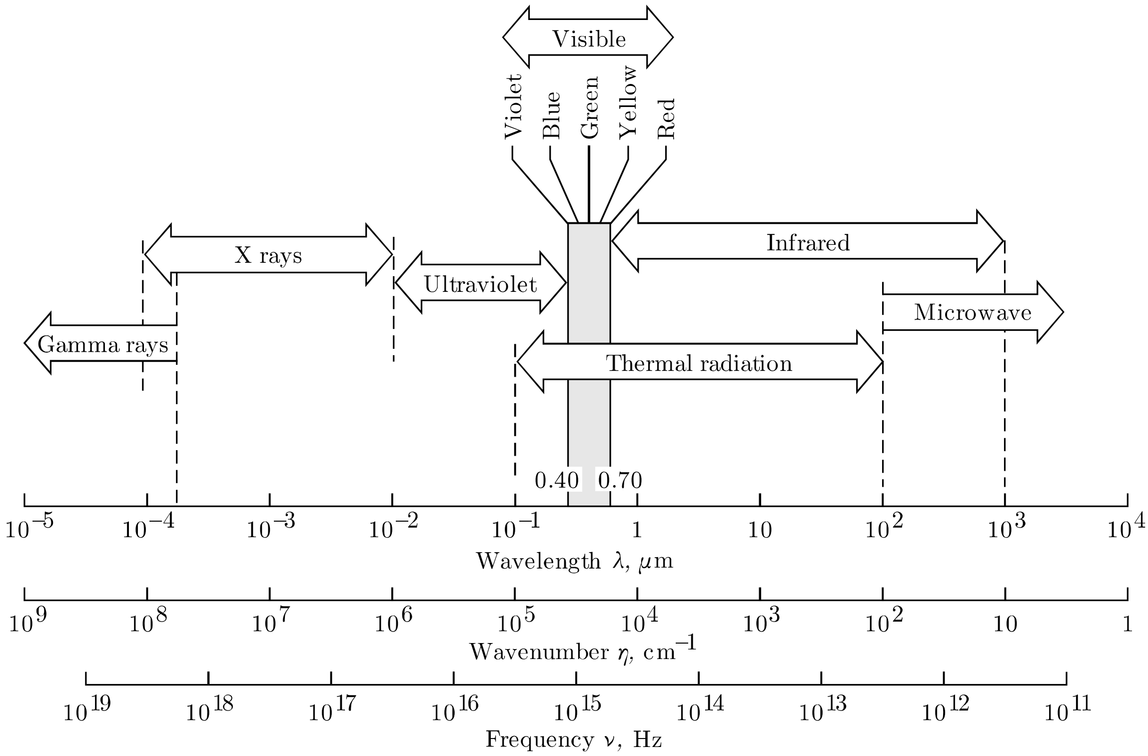

Figure 2.1: Electromagnetic wave spectrum [15].

or partially. The part that permeates the medium is in turn either absorbed, or it reemerges from another side. Materials that can completely absorb and reflect all incoming radiation and are called *opaque*. Metals are almost always opaque and non-metals can be opaque depending on their thickness. Opaque surfaces that absorb all radiation irrespective of wavelength or angle of incidence and do not reflect any, are referred to as *black surfaces*, since no radiation is reflected back to the eye of the observer they appear as black. A consequence of this definition is that all radiation that is absorbed by the medium is emitted by the source at every wavelength, in all directions. This makes the black surface the perfect absorber and emitter and it is usually used as a standard against which real surfaces are compared.

Real surfaces absorb and reflect the incident radiation. The amount of radiation that will be reflected or absorbed depends on four factors, namely: the angle of incidence, the surface and material condition, the wavelength of the incoming radiation and finally, temperature. For engineering calculations it is usually safe to assume, depending on the use of the surface (expected temperature, wavelength range etc.), average appropriate values. From these definitions three radiative properties can be defined as:

$$\text{Reflectance:} \qquad \mathscr{R} \equiv \frac{\text{reflected part of incoming radiation}}{\text{total incoming radiation}},$$

$$\text{Absorptance:} \qquad \mathscr{A} \equiv \frac{\text{absorbed part of incoming radiation}}{\text{total incoming radiation}},$$

$$\text{Transmittance:} \qquad \mathscr{T} \equiv \frac{\text{transmitted part of incoming radiation}}{\text{total incoming radiation}}.$$

And, because of the conservation of energy:

$$\rho + \alpha + \tau = 1. \tag{2.19}$$

From the definition of transmittance it can be concluded that, if the real surface in question is opaque, $\tau = 0$. Also in the case of a black surface, since no radiation is reflected or transmitted, $\tau = \rho = 0$ and $\alpha = 1$.

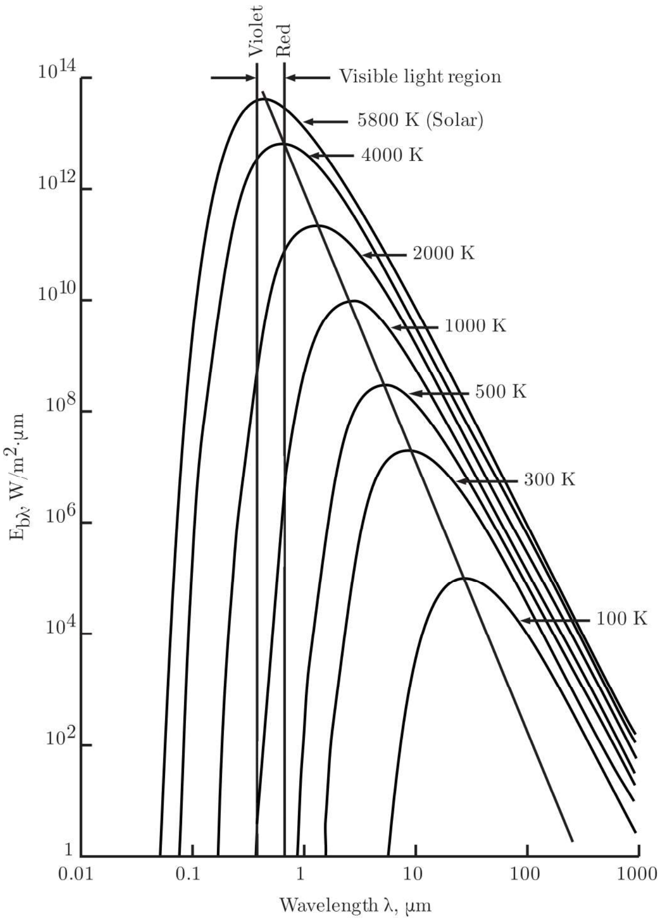

Figure 2.2: Blackbody emissive power spectrum [16].

Another fundamental radiative property is emission. All matter constantly emits radiation into all directions at random and at intervals that depend on the properties of the material, as well as the temperature. The radiant energy emitted per unit area of surface is named the emissive power, E. The emissive power can be also quantified at given frequencies as monochromatic or spectral emissive power, E_v. The emissive power of a black surface bounded by a transparent medium was firstly described by Max Planck, and stated that the increase of temperature causes the total radiated energy to increase and the peak of the emitted spectrum to shift to shorter wavelengths. Examples of the blackbody emissive power over the wavelength at different temperatures are displayed in Figure 2.2. The spectral blackbody emissive power as a function of temperature and frequency is:

$$E_{b\nu}(T,\nu) = \frac{2\pi h \nu^3 n^2}{c_0^2 [e^{h\nu/kT} - 1]}. \tag{2.20}$$

Since Planck's law can determine the monochromatic emissive power, the integration of over the whole spectrum can determine the total blackbody emissive power. That is:

$$E_b(T) = \int_0^\infty E_{b\nu} d\nu = \int_0^\infty E_{b\lambda} d\lambda = \int_0^\infty E_{b\eta} d\eta. \tag{2.21}$$

Equation 2.21 is true only if the refractive index is independent of frequency, wavelength and wavenumber, which applies for vacuum and is a good approximation for ordinary gases without particulates.

Since all surfaces are emitting thermal radiation, it is easy to define a fourth non-dimensional radiative property, the emittance. The emittance of a real surface is defined compared to the emitted energy of a black surface as:

Emittance: $$\varepsilon \equiv \frac{\text{emitted energy from a surface}}{\text{energy emitted by a black surface at the same temperature}}.$$

The emittance also varies between 0 and 1 and based on the definitions of the other properties the emittance of a blackbody is equal to its absorbance.

RADIATIVE INTENSITY

In engineering applications not all photons originate from a single surface. Therefore, the use emissive power in these problems is restricting because it does not vary with the directional element of radiation. Thus, the radiative intensity is introduced in order to include the directional dependence of the radiation field. The radiative intensity is defined as the heat flow that is emitted in the (θ, ϕ) direction per unit area normal to this direction and per unit solid angle about this direction. Thus,

$$I(\varphi,\theta) = \frac{d\dot{Q}}{dA \cos\theta d\Omega}. \tag{2.22}$$

where $d\dot{Q}$ is the radiation energy, φ is the azimuthial angle, θ is the zenith angle, dA is the infinitesimal area of a surface and $d\Omega$ the infinitesimal solid angle. Same as before, a distinction can be made between spectral intensity and total intensity. The spectral instensity is defined as the radiative intensity per wavelegth and they are related by:

$$I(\varphi,\theta) = \int_0^\infty \mathrm{I}_\eta(\varphi,\theta,\eta) d\eta. \tag{2.23}$$

Surfaces for which the emitted intensity is independent of direction are called diffusive surfaces.

RADIATIVE TRANSFER EQUATION

Within a medium, the usage of emissive power as defined above is not applicable because there is no surface to which to relate it. If a medium is not participating in any way, i.e it does not scatter, emit or absorb any radiation, then the radiative energy is constant along its path. However, in combustion systems that is almost never the case. As radiation travels through a layer of gas, it is gradually becoming attenuated by all the aforementioned ways. In order to calculate the change in intensity along an arbitrary path s, a radiative energy balance must be conducted, more commonly known as the radiative transfer equation.

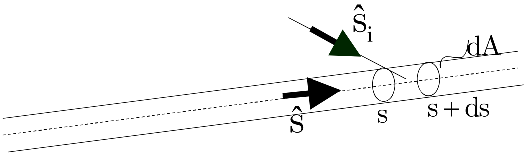

Figure 2.3: Schematic for the derivation of the RTE [17].

The radiative transfer equation (RTE) describes the radiative intensity within an enclosure as a function of a propagation vector, by using the angular variables φ and θ, and the wavenumber η along an arbitraty path s. To acquire the radiative heat flux, all the contributions irradiating from all directions for all the wavenumbers to the surface must be summarized and then integrated. This is in principle the application of the conservation of radiative energy on an control volume. According to this definition, the change in radiative intensity is:

$$\frac{\partial I_\eta}{\partial s} = \kappa_\eta I_{b\eta}(s,t) - \kappa_\eta I_\eta(s,\hat{s},t) - \sigma_{s\eta} I_\eta(s,\hat{s},t) + \frac{\sigma_{s\eta}}{4\pi}\int_{4\pi} I_\eta(s,\hat{s},t)\Phi_\eta(\hat{s}_i,\hat{s})d\Omega_i, \tag{2.24}$$

where on the right hand side the first term denotes the intensity increase due to emission, the second its decrease due to absorption, the third the scattering away from $\hat{s}$ and the last the scattering into the direction from other sources. The details for the directional aspects of are shown in 2.3 and κ_η, $\sigma_{s\eta}$ and Φ_η are namely, the absorption coefficient, the scattering constant and the scattering phase function. While in general, there are different coefficients for emission and absorption, equation 2.24 is presented under the usual assumption that in infinitesimal volumes there is local thermal equilibrium and thus, according to Kirchoff's law the emission and absorption coefficients are the same.

When only molecular gases are considered in the case of combustion, meaning that particulates are not created, the contribution of scattering is really small and usually neglected. In that case, the last two terms of 2.24 are neglected and therefore, only the absorption-emission process needs to be considered.

THE ABSORPTION COEFFICIENT

When radiation penetrates an absorbing medium it is continuously getting attenuated by absorption. This decay is exponential and it is usually referred as the

Beer–Lambert law. The transmissivity of a homogeneous isothermal gas layer can be described as,

$$\tau_\eta = e^{-\kappa_\eta s} \tag{2.25}$$

where s is the thickness of the gas layer and κ_η is the absorption coefficient. Moreover, since the gas medium is non-scattering, the spectral absorptivity can be specified as $\alpha_\eta = 1 - \tau_\eta$

In order to analyze the absorption coefficient, the spectral aspect of radiation must be explained. As mentioned in the previous section, when gas molecules are in the path of photons, they interact, either by absorbing the incoming photons and simultaneously exciting the molecules into higher energy states, or by scattering them into a different direction. At the same time, excited gas molecules can lower their energy randomly by emitting appropriate photons. For the calculation of the absorption coefficient, knowledge of all possible excitations (transitions) is important.

There are many factors that can contribute to the change of the internal energy in a gas molecule. In the moderate temperatures at which most common combustion processes occur, the most important transitions are called bound-bound transitions. These occur when the atoms that comprise the molecule spin around a different axis or when they vibrate relative to each other. According to quantum mechanics, the frequencies of rotation and vibration can only be changed by discrete amounts. Thus, these transitions must occur in discrete wavelengths and therefore absorption and emission of photons from molecules must happen at distinguishable spectral lines. These lines are grouped into the vibration-rotation bands and are present in the infrared spectrum. Some important combustion gases are presented in Figure 2.4.

The rotation-vibration can be approximated by classical mechanics using a spring-mass model, based on the fact that every particle can move in space as seen in the Figure 2.4. While moving in space, each particle has three degrees of freedom. In the case that more particles are connected into N molecules, each atom has the same three degrees of freedom and there are $3N-3$ degrees of freedom representing the relative motion inside the molecule. Thus, the molecule has a three dimensional translation and $3N-3$ internal degrees that are represented as rotation and vibration of the molecule. It must also be noted that not all molecules have rotational bands. For a rotational transition, a dipole moment is required and thus, diatomic molecules prevalent in combustion such as oxygen (O_2) and nitrogen (N_2) cannot go through these transitions.

As discussed in the previous section, the change of the internal energy of a molecule requires energy. The changes due to vibration need more energy in general and their spectral bands are usually in the infrared spectrum. Rotational energy changes on the other hand require less energy (and thus, are more common) and their spectral bands are found in the far infrared. However, the exact energies that the photons must provide slightly vary due to quantum uncertainty and that results into the broadening of spectral lines. The most prevalent phenomena that result in the broadening of the spectral lines are natural line broadening, collision broadening, Stark broadening and Doppler Broadening. In the temperatures of usual engineering

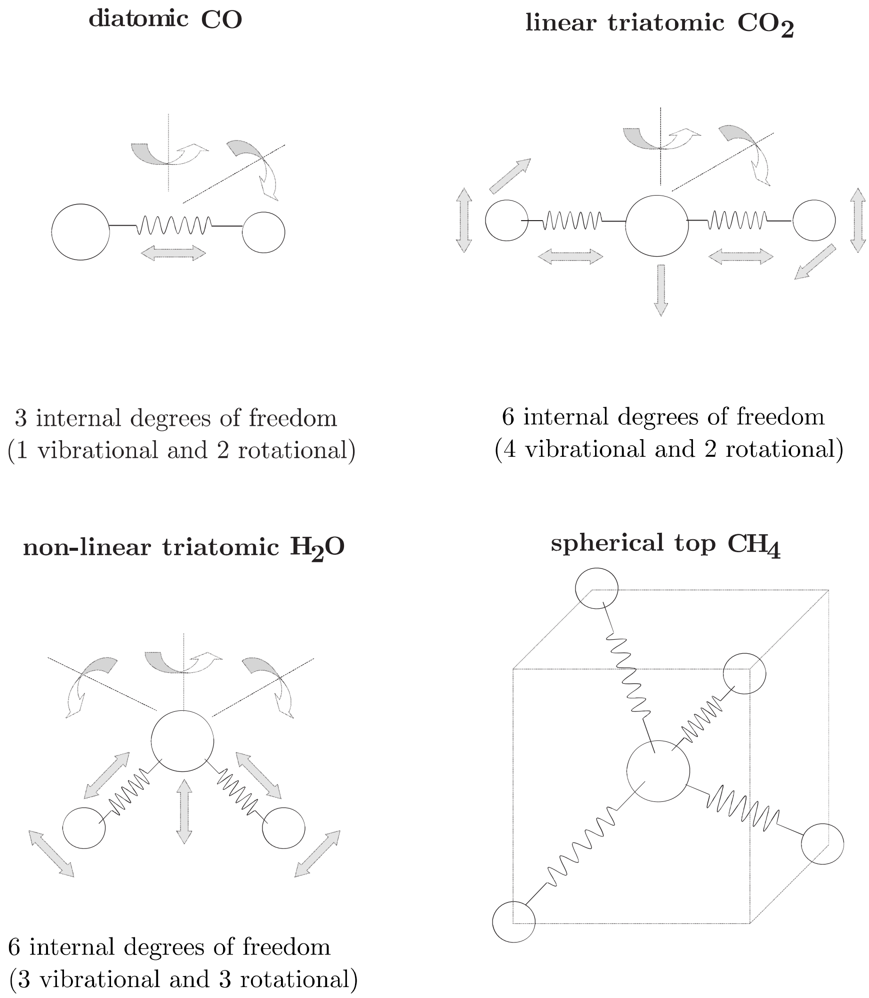

Figure 2.4: Vibrational and rotational degrees of freedom of principal combustion gas species [18].

applications the collision and, on a lesser extent, the Doppler broadening are most important.

Single spectral lines are completely characterized by their strength and their line width, in conjuction with the broading mechanism. The strengths widths and exact locations of spectral lines are well researched subjects and have been collected in numerous modern databases, the most notable of these the HITRAN Spectral database, the HITEMP and CDSD. An example of the pressure-based absorption coefficient of water vapor at 1000 K for a portion of its $6.3\mu m$ band is shown in Figure 2.5 based on the HITEMP database [19].

It can be undeniably observed that there are many, pronounced spectral variations of the absorption coefficient. In the presented part of the spectrum exist thousands of spectral lines that take up all the available bands. In this thermodynamic state, 9.5 million and 280,000 lines are shown in Figure 2.5 and its inline, respectively which are in fact a fraction of the available spectral variations. The HITEMP database contains the most important 111 million lines of water vapour at at the specified state. At higher temperatures, the spectral lines narrow considerably, thus decreasing the line overlap, and at the same time the strength of the

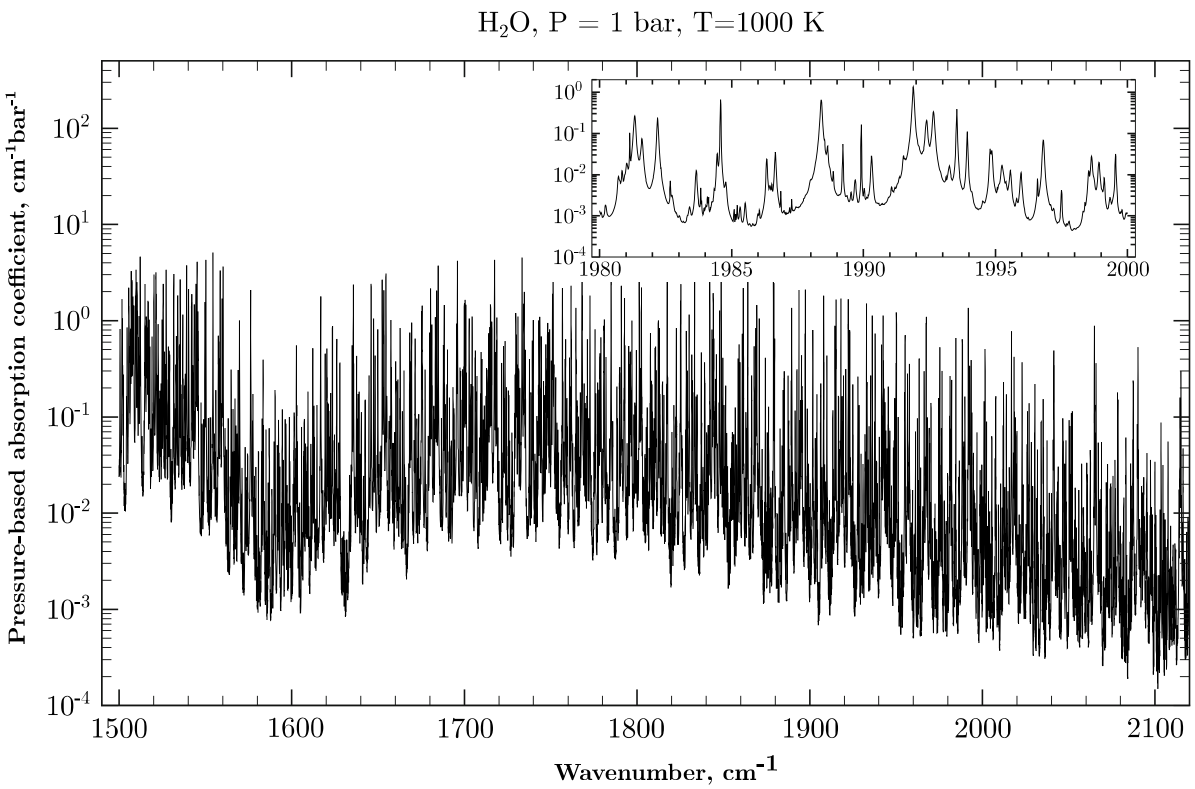

Figure 2.5: Pressure-based spectral absorption coefficient for small amounts of H_2O in nitrogen; partial 6.3μm band [19]

lines the lines that were most important at low temperatures decrease. In addition, many more lines appear which are known as the hot lines. These are created by molecules that exhibit higher vibrational levels [15]. Using these databases as a basis, many models are tuned, by using line by line calculations at it will described later, in Chapter 2.7.

2.2. TURBULENT COMBUSTION

When reactions are happening in a turbulent environment there is direct interaction between turbulence and combustion. This is actually occurring in the majority of combustion systems, such as internal combustion engines, furnaces, gas turbines and aircraft engines. Therefore, it is important to understand how turbulent combustion works and furthermore, model it, in order to improve these systems and even develop new ones that can satisfy future and contemporary needs.

TURBULENCE

Turbulence is a phenomenon of great importance for many scientific fields and in particular, for reacting fluid flows. Turbulence is mostly an open question, since it involves numerous time and length scales. Consequently, turbulent flows cannot be easily defined and the borders between laminar flows and transition to turbulence are blurry. It is generally accepted that turbulent flows are unsteady flows that have irregular fluctuations in all three spacial directions. They are irregular; however, they are not random, but possess certain structure and coherence. These spacial structures are called eddies and exist for brief periods of time. Large eddies can contain smaller eddies which in turn can contain even smaller ones. This phenomenon is explained as the transfer of kinetic energy in the flow. The main flow provides kinetic energy which is in turn transferred to the large eddies. The large eddies in turn break up into smaller and smaller eddies thus, cascading the energy into the smallest scales. This continues until the energy is transferred to the smallest scale of eddies, commonly known as the Kolmogorov scale. In this scale, opposite forces the fluid's viscosity dissipates the kinetic energy into heat in a phenomenon called dissipative heating.

COMBUSTION

Combustion can be defined as the chemical reactions occurring between molecules acting as fuel and an oxidizing agent, that produces energy which is usually translated into heat light. The fuel and the oxidizing agent are mixed (or in some cases are already mixed) due to a flow field and subsequently react forming products. Depending on the abundance of the oxidizing agent, combustion can be called [13]:

- rich: when there is oxidizer is abundance,
- lean: when the oxidizer is not enough to completely consume the available fuel,
- stoichiometric: when exactly enough oxidizer is provided to completely react with all of the existing fuel.

Combustion is a very complicated sequence of elementary radical reactions. Another additive layer to this complex process is, that it also involves a vast range of different chemical scales in length and time. In order to differentiate between different combustion regimes, the combustion processes are categorized into several distinct categories. At first, it is useful to categorize them upon whether the fuel and oxidizer are firstly mixed and react at a later stage or if mixing and reacting occurs simultaneously. There categories are named premixed and nonpremixed combustion respectively. Both of these categories are then subdivided based on the fluid flow, in laminar and turbulent. Examples of laminar premixed combustion are Bunsen flames and flat flames, of turbulent premixed are spark-ignited engines, of laminar nonpremixed are candles and wood fires, and of turbulent nonpremixed are Diesel engines and turbines [13].

TURBULENCE COMBUSTION INTERACTION

During turbulent combustion there is direct interaction between turbulence and chemistry. Heat release induces strong flow accelerations and thus, strongly affects turbulence. Moreover, large changes in kinematic viscosity occur, due to temperature changes, further influencing turbulence. This mechanism can generate turbulence, or even damp it, and is commonly called “flame-generated turbulence”. At the same time, the flame structures are in turn affected by turbulence. Turbulence can alter the flame structure, which can enhance combustion by providing additional mixing of chemical elements or can even completely inhibit it, leading to flame blowout. The main hurdles that are most commonly associated with turbulent reacting flows are three [20]:

1. The vast range of temporal and spatial scales which are in the order of meters down to micrometer, where mixing and viscous dissipation takes place.
2. The range of species reacting at different timescales.
3. The highly non-linear behaviour of chemical reactions with the highly variable local temperature.

2.2.1. CFD APPROACHES FOR TURBULENT COMBUSTION

Chemically reacting turbulent flows at the high Reynolds numbers, which are typical in engineering combustion systems, exhibit a wide dynamic range of time and length scales. The largest length scales are usually fixed by the size of the system in question and the smallest correspond to the Kolmogorov scale discussed above. While theoretically it is possible to resolve all the mentioned scales explicitly, their enormous number makes such task computationally challenging. In order to reduce the computational cost, Computational Fluid Dynamics (CFD) simulations are usually conducted either by using probabilistic approaches, or filtering. In order to calculate turbulent combustion in a numerical scheme, there are three major approaches.

DNS

The Direct Numerical Simulation (DNS), since its introduction a few decades ago and with the exponential increase of computer power in recent years, provides an appealing choice when considering CFD calculations. It involves the complete numerical simulations of three-dimensional balance equations that describe the flow and chemistry without the inclusion of chemistry or turbulence models. However, the simulation of chemically reacting flows with the inclusion of multispecies transport, realistic thermodynamics and complex chemistry adds layers of complexity that make the choice of this method prohibitive due to the enormous computational cost. However, it can still be used as a tool in a supportive role, along with experiments and theoretical analysis to investigate fine details, in conjunction with other approaches.

RANS

Reynolds Averaged Navier Stokes (RANS) are based on solving the mean values of all quantities involved. This approach was the first possible approach because the computation of the instantaneous flow field in a turbulent flame was simply not possible. In a turbulent flame, the estimate of the local mean value of any quantity can be calculated by averaging over a long time. That is, because turbulent flows generally can be statistically stationary. The derivation of the RANS equations can happen by decomposing any physical quantity into the sum of its local mean value and a fluctuation with respect to that mean. However, by implementing this method several unclosed terms appear that require closure. In order to resolve this issue, the need arises for a turbulence model, to deal with the flow dynamics and a turbulent combustion model, to describe the chemical species reactions and the subsequent heat release.

LES

The last approach is the Large Eddy Simulation (LES). LES can be considered as compromise between the explicitly solved DNS and the averaged RANS. In this method, the larger eddies are explicitly calculated using the same method implemented in DNS, whereas the smaller subgrid scales require modeling, much like the RANS approach. In order to achieve that, the balance equations are filtered in the physical space, by using filter functions, or in the spectral space, by using Fourier transformed fields. The LES should be implemented in a sufficiently fine mesh. While computationally more expensive than the usual RANS approach, it is preferred in cases in which unsteady fields are modeled such as spark ignition and blowoff. It should be noted that while this approach presents similarities with the RANS approach, they are in principle completely distinct. LES is based on the separation of scales with large kinetic energy containing eddies and small energy dissipation eddies, whereas RANS is simply based on the averaging procedure that will be discussed later.

2.3. REYNOLDS AVERAGED GOVERNING EQUATIONS

In this section the decomposed turbulent combustion governing equations will be provided. In the Reynolds decomposition, any variable $\Xi(x,y,z,t)$ over a long time can be decomposed into the sum of two variables, an average $\overline{\Xi}(x,y,z)$ and a fluctuation $\Xi'(x,y,z)$. By definition the average of the fluctuation is equal to zero $(\overline{\Xi'}(x,y,z)=0)$. Thus,

$$\Xi = \overline{\Xi} + \Xi' \tag{2.26}$$

In the case of compressible gases a different procedure is implemented, Favre averaging. This procedure enables the separation of turbulent fluctuations from the mean-flow. In Favre averaging, all momentum and scalars with the exception of density are decomposed using Favre-averaged means and fluctiations as described below. In principle, all variables are density weighted in order to capture the influence of density changes.

$$\Xi = \widetilde{\Xi} + \Xi'' \tag{2.27}$$

where the Favre averaged term can also be expressed as:

$$\widetilde{\Xi} = \frac{\overline{\rho\Xi}}{\overline{\rho}} \tag{2.28}$$

In some cases incompressible ideal gas can be approximated, based on the Mach number. It must be noted that in the case of incompressibility the Favre averaging is the same as the Reynolds averaging. Thus for completion, the Favre averaged governing equations will be presented based on the aforementioned decomposition method.

- The continuity equation:

$$\frac{\partial\overline{\rho}}{\partial t} + \frac{\partial\overline{\rho}\widetilde{u_i}}{\partial x_i} = 0 \tag{2.29}$$

- The Navier-Stokes equations:

$$\frac{\partial}{\partial t}\overline{\rho}\widetilde{u_i} + \frac{\partial}{\partial x_i}\overline{\rho}\widetilde{u_i}\widetilde{u_j} = -\frac{\partial\overline{p}}{\partial x_i} + \frac{\partial}{\partial x_j}\left(\overline{\tau}_{ij} - \underbrace{\overline{\rho}\widetilde{u_i''u_j''}}_{(1)}\right) \tag{2.30}$$

- The species transport equation:

$$\frac{\partial\overline{\rho}\widetilde{Y_k}}{\partial t} + \frac{\partial\overline{\rho}\widetilde{u_i}\widetilde{Y_k}}{\partial x_i} = -\frac{\partial}{\partial x_i}\left(\underbrace{\overline{V_{k,i}Y_k}}_{(2)} + \underbrace{\overline{\rho}\widetilde{u_i''Y_k''}}_{(3)}\right) + \underbrace{\overline{S}_{k,\mathrm{chem}}}_{(4)} \tag{2.31}$$

- The energy equation:

$$\begin{aligned}\frac{\partial}{\partial t}\overline{\rho}\widetilde{e} + \frac{\partial}{\partial x_j}\overline{\rho}\widetilde{u_j}\widetilde{e} = &-\frac{\partial}{\partial x_j}\overline{p}\widetilde{u_j} + \frac{\partial}{\partial x_j}\overline{u_i\tau_{ij}} \\ &-\underbrace{\overline{u_j''\frac{\partial p}{\partial x_j}}}_{(5)} - \frac{\partial}{\partial x_j}\left(-\underbrace{\overline{q_j}}_{(6)} + \underbrace{\overline{\rho}\widetilde{u_i''e''}}_{(7)}\right) + \underbrace{\overline{\dot{Q}}}_{(8)}\end{aligned} \tag{2.32}$$

The terms in underbraces presented in (2.29-2.32) are the unclosed terms of the Favre averaged equations. These terms require closure and in order to resolve the system they must be modeled. These terms are, in order of appearance:

1. *The Reynolds stresses* $\overline{\rho}\widetilde{u_i''u_j''}$.

Due to the decomposition of the stress tensor, six unknown quantities need to be closed. These terms are closed by the turbulence model. The most common models, such as the $k-\epsilon$ and the $k-\omega$, were developed for turbulent, non-reacting fluid flows. Thus, heat release effects might not be captured correctly. The models that will be explored as part of this thesis are based on the Boussinesq hypothesis, in which the turbulent viscosity μ_t is assumed as an isotropic scalar quantity. More details will be provided in Section 2.4.

2. *The species laminar fluxes $\overline{V_{k,i}Y_k}$.*

Laminar mass diffusion in turbulent flows is modeled as it would in laminar flows:

$$\overline{V_{k,i}Y_k} = \overline{\rho D_{k,i}\frac{\partial Y_k}{\partial x_i}} \approx \overline{\rho}\,\overline{D}_{k,i}\frac{\partial \widetilde{Y}_k}{\partial x_i} \tag{2.33}$$

where $D_{k,i}$ is the mixture mass diffusion coefficient for the species k in the gas mixture [21].

3. *The species turbulent fluxes $\overline{\rho}\widetilde{u_i''Y_k''}$.*

Turbulent mass diffusion can be modeled by assuming a gradient:

$$\overline{\rho}\widetilde{u_i''Y_k''} = -\frac{\mu_t}{Sc_{t,k}}\frac{\partial \widetilde{Y}_k}{\partial x_i} \tag{2.34}$$

where $\mathrm{Sc}_{\mathrm{t,k}}$ the turbulent Schmidt number for species k and μ_t is the turbulent viscosity, as estimated from the turbulence model. The default Sc_t is 0.7. Generally, turbulent diffusion overwhelms laminar diffusion, and the specification of detailed laminar diffusion properties in turbulent flows is not usually necessary [21].

4. *The mean species chemical production rate $\overline{S}_{k,\mathrm{chem}}$.*

Modeling the species production rate in the turbulent regime is the main focus of the turbulent combustion research. It has to be modeled, as it is the driving force of turbulent combustion. The turbulence chemistry interaction and the way it is modeled will be discussed in Section 2.5.

5. *The pressure velocity correlation $\overline{u_j''\frac{\partial p}{\partial x_j}}$.*

The pressure velocity correlation appears in the energy equation and it is commonly neglected in most RANS codes [11]. However, the omission of this term is disputed for turbulent reactive flows [22]. Since ANSYS Fluent does not allow the modeling of this term, this research was conducted without it.

6. *The laminar diffusion of energy $\overline{q_i}$.*

The terms that comprise the energy flux were discussed in Section 2.1.5. By neglecting the last two terms and introducing the effective conductivity the result is:

$$\overline{q_i} = \overline{\lambda}\frac{\partial \widetilde{T}}{\partial x_i} \tag{2.35}$$

with $\overline{\lambda}$ the mixture thermal diffusivity.

7. *The turbulent diffusion of energy $\overline{\rho}\widetilde{u_i''e''}$.*

In order to model the turbulent diffusion of energy, the turbulent Prandtl number was introduced (Pr_t). Similar to the definition of the Prandtl number (defined as the ratio of momentum diffusivity to thermal diffusivity), the turbulent Prandtl number is defined as the relationship between the extra shear stress (Reynold's stresses) and the turbulent diffusion of energy. Thus,

$$\overline{\rho u_i''e''} = -C_p\frac{\mu_t}{\mathrm{Pr}_t}\frac{\partial \widetilde{T}}{\partial x_i} \tag{2.36}$$

The default value for the turbulent Prandtl is 1.

8. *The source term* $\overline{\dot{Q}}$.

The source term captures all the additional energy that is provided to the system. In turbulent combustion this includes the heat created by the chemical reactions and is captured by the combustion model and the heat tranfered by radiation as a radiation source term [21]. The radiation modeling will be discussed in detail in Section 2.7.

2.4. TURBULENCE MODELING

As mentioned in Section 2.1.3, the Navier-Stokes equations fully describe the flow fields in all fluid flows. However, in order to be able to resolve these equations, the aforementioned Reynolds stresses must be modeled. In this section the different models that were used in the context of this thesis will be introduced.

As it is evident in equation 2.30, the right hand side consists of three terms, which can be described as, the isotropic stress from the mean pressure field, the viscous stresses and finally, the adeptly named Reynolds stresses that result from the Reynolds averaging procedure. Thus, it can be considered that as the viscous stress is created from momentum transfer to the smallest possible scales, the Reynolds stresses should stem from the momentum transfer by the fluctuating velocity field. This thought process is named the turbulent viscosity hypothesis, also known as the Boussinesq hypothesis. This hypothesis is relating the Reynolds stresses to the mean velocity gradients as [21] [23]:

$$-\overline{\rho u_i' u_j'} = -\overline{\rho}\widetilde{u_i'' u_j''} = \mu_t\left(\frac{\partial \widetilde{u_i}}{\partial x_j} + \frac{\partial \widetilde{u_j}}{\partial x_i}\right) - \frac{2}{3}\left(\overline{\rho}k + \mu_t \frac{\partial \widetilde{u_k}}{\partial x_k}\right)\delta_{ij} \tag{2.37}$$

By using this assumption, the only terms that need to be modeled are the turbulent kinetic energy k and the turbulent viscosity μ_t. This in turn, requires the construction of the so-called two equation models that can lead to the eventual closure of the equations.

An alternative approach to the modeling of the Reynolds stresses is to solve separate transport equations for each of the unclosed terms of the stress tensor i.e the Reynolds Stress Model. Using this approach five additional equations must be solved for two dimensional approaches and seven additional for three dimensional approaches (one extra equation to determine the scales is normally required). While this is a more detailed approach, the models based on the turbulent viscosity hypothesis usually perform adequately and the additional computational resources required for this approach can be considered excessive.

In the subsequent sections the two equation models that were used for the scope of this thesis will be discussed, namely, the standard $k-\varepsilon$ model, the realizable $k-\varepsilon$ model, a standard $k-\varepsilon$ model with modified constants and the $k-\omega$ SST model.

2.4.1. THE STANDARD $k-\varepsilon$ MODEL

The first of the two-equation models, which is also considered the simplest one, is the standard $k-\varepsilon$ model. After its introduction by Spalding and Launder [24] and its later refinement by the same authors [25] it has become the basic turbulence model for numerous engineering applications. It's main goal is to calculate the turbulent kinetic energy k and the turbulent viscosity μ_t using the transport equations:

$$\frac{\partial}{\partial t}(\overline{\rho} k)+\frac{\partial}{\partial x_i}(\overline{\rho}\widetilde{u}_i k)=\frac{\partial}{\partial x_i}\left[\left(\mu+\frac{\mu_t}{\sigma_k}\right)\frac{\partial k}{\partial x_i}\right]+P_k+\overline{\rho}\varepsilon \tag{2.38}$$

$$\frac{\partial}{\partial t}(\overline{\rho}\varepsilon)+\frac{\partial}{\partial x_i}(\overline{\rho}\widetilde{u}_i\varepsilon)=\frac{\partial}{\partial x_i}\left[\left(\mu+\frac{\mu_t}{\sigma_\varepsilon}\right)\frac{\partial \varepsilon}{\partial x_i}\right]+C_{\varepsilon 1}\frac{\varepsilon}{k}P_k+C_{\varepsilon 2}\overline{\rho}\frac{\varepsilon^2}{k} \tag{2.39}$$

where the ε is the dissipation of the turbulent kinetic energy, $C_{\varepsilon 1}$, $C_{\varepsilon 2}$ are models constants, σ_k and σ_ε are the turbulent Prandtl numbers for k and ε respectively, and P_k is the the production of turbulent kinetic energy. The production of kinetic energy is modeled based on the Boussinesq hypothesis as such:

$$P_k=\mu_t\left(\frac{\partial\widetilde{u_i}}{\partial x_j}\right)^2 \tag{2.40}$$

And the modeling constants are in order of appearance:

$$\sigma_k=1.0,\ \sigma_\varepsilon=1.3,\ C_{\varepsilon 1}=1.44 \text{ and } C_{\varepsilon 2}=1.92$$

These are empirical values, set based of the works of Launder [24], and are considered appropriate to plane jets and mixing layers.

The use of 2.38 and 2.39 enables the calculation of the turbulent viscosity using the formulation:

$$\mu_t=\overline{\rho}C_m\frac{k^2}{\varepsilon} \tag{2.41}$$

where C_μ is a model constant and is equal to 0.09.

2.4.2. THE MODIFIED STANDARD $k-\varepsilon$ MODEL

The standard $k-\varepsilon$ has been found to work fairly well for a wide range of wall-bounded and free shear flows over decades of research [21]. A common problem however, noted from the creators of the model is its inability to adequately estimate the flow field of axisymmetric jets [25], [26]. The standard model tends to overpredict the spreading rate and decay rates of round jets.

In order to tackle these known issues, several proposals have been made that involve the remodeling of the constants $C_{\varepsilon 1}$, $C_{\varepsilon 2}$ and C_μ. One of such modifications is the modification of the $C_{\varepsilon 1}$ constant, proposed by Rodi et al [26]. It is based on the argument that the decay rate affects only the scale of eddies characteristic of a cross section of the jet and not the lateral length scale distribution. Thus, a modification on ε-equation is implemented by introducing a retardation parameter to the $C_{\varepsilon 1}$ constant:

$$C_{\varepsilon 1} = 1.14 - 5.31 \frac{y_{1/2}}{U_{cl}} \frac{dU_{cl}}{dx} \tag{2.42}$$

where $y_{1/2}$ is the distance from the axis where the velocity is half of the centerline value and U_{cl} is the centerline velocity.

This formulation can be applied in plane and round jets. According to [26] the introduced parameter takes a value of -0.087 for a round jet, while for a plane jet the parameter is -0.055. This means the $C_{\varepsilon 1}$ constant will take the values of ***1.44*** *in plane jets* and ***1.6*** *in round jets* [27]. This solution is found to adequately capture the effects of round jets in turbulent phenomena, however by introducing such modification the generality of the model standard model is abandoned [28].

2.4.3. THE REALIZABLE $k-\varepsilon$ MODEL

Another model created to overcome the shortcoming of the standard $k-\varepsilon$ model is the realizable $k-\varepsilon$ model. The two core differences of this model compared to the standard one are that the realizable $k-\varepsilon$ model introduces a new formulation for the turbulent viscosity and a new transport equation for the dissipation rate ε [29].

The term realizable stems from its consistency to the physics of turbulent flows, due to the fact that it meets certain mathematical constrains on the Reynolds stresses. Based on this definition the standard $k-\varepsilon$ model is not "realizable" [30].

A major benefit of the realizable model is that can more accurately predict the spreading rate and decay rates of round jets. It can also accurately predict flows that include rotation, recirculation and boundary layers under pressure gradients and separation [21]. The modeled transport equation for k is the same as 2.38 and the new equation for ε is:

$$\frac{\partial}{\partial t}(\bar{\rho}\varepsilon) + \frac{\partial}{\partial x_i}(\bar{\rho}\widetilde{u_i}\varepsilon) = \frac{\partial}{\partial x_i}\left[\left(\mu + \frac{\mu_t}{\sigma_\varepsilon}\right)\frac{\partial \varepsilon}{\partial x_i}\right] + \bar{\rho}C_1 S\varepsilon + C_2\bar{\rho}\frac{\varepsilon^2}{k\sqrt{\nu\varepsilon}} \tag{2.43}$$

where the constant C_1 can be found from:

$$C_1 = \max\left[0.43, \frac{\eta}{\eta+5}\right] \tag{2.44}$$

with $\eta = S\frac{k}{\varepsilon}$ and $S = \sqrt{2S_{ij}S_{ij}}$. S_{ij} is the deformation tensor and C_2, σ_k and σ_ε are again, model constants. The model constants are carefully selected so the model performs well for canonical flows [21]. They are in order of appearance,

$$\sigma_k = 1.0,\ \sigma_\varepsilon = 1.2 \text{ and } C_2 = 1.2$$

The second difference for the standard model is the calculation of the turbulent viscosity. The same formulation as in the standard $k-\varepsilon$ is used (2.41), however in this case C_μ changes depending on:

$$C_\mu = \frac{1}{A_0 + A_s \frac{kU^*}{\varepsilon}} \tag{2.45}$$

where U^* can be described as

$$U^* \equiv \sqrt{S_{ij}S_{ij} + \widetilde{\Omega_{ij}}\widetilde{\Omega_{ij}}} \tag{2.46}$$

The last term on the right hand side can be analyzed as $\widetilde{\Omega_{ij}} = \Omega_{ij} - 2\varepsilon_{ijk}\omega_k$ where $\Omega_{ij} = \overline{\Omega}_{ij} - \varepsilon_{ijk}\omega_k$. $\overline{\Omega}_{ij}$ is the mean rotation rate viewed in a rotating reference frame with the angular velocity ω_k and ε_{ijk} Levi-Civita symbol. Moreover, in 2.45 $A_0 = 4.04$ is a model constant and $A_s = \sqrt{6}\cos\phi$, where $\phi = \frac{1}{3}\cos^{-1}\left(\sqrt{6}\frac{S_{ij}S_{jk}S_{ki}}{\sqrt{S_{ij}S_{ij}}^3}\right)$ and the mean strain rate defined by $S_{ij} = \frac{1}{2}(\frac{\partial u_j}{\partial x_i} + \frac{\partial u_i}{\partial x_j})$.

2.4.4. THE $k-\omega$ SST MODEL

Wilkox et al decided to reassess the original closure approximations for two equation models. Since it was not evident what the best choice of dependent variables are, the specific dissipation rate ω was introduced [31]. This led to the creation of the $k-\omega$ model. This model was more successful in terms of robustness and accuracy. It can better capture the adverse pressure gradient condition effects and it is far more stable numerically-wise since it does not contain damping functions [32]. However, this model has also has several shortcomings, namely it does not correctly predict the asymptotic behavior turbulence in the free stream. Menter et al [33],[34], tried to resolve this issue by combining the $k-\varepsilon$ with the $k-\omega$ model in the $k-\omega$ SST model. The SST (Shear Stress Transport) model is identical to the Wilkox model in the inner 50% of the boundary-layer but changes gradually to the standard $k-\varepsilon$ model (in a $k-\omega$ formulation) towards the boundary-layer edge. The new model is also virtually identical to the $k-\varepsilon$ model for free shear layers . The equations of the $k-\omega$ SST model are:

$$\frac{\partial k}{\partial t} + U_j\frac{\partial k}{\partial x_j} = P_k - \beta^* k\omega + \frac{\partial}{\partial x_j}\left[(\nu + \sigma_k\nu_T)\frac{\partial k}{\partial x_j}\right] \tag{2.47}$$

$$\frac{\partial \omega}{\partial t} + U_j\frac{\partial \omega}{\partial x_j} = \alpha S^2 - \beta\omega^2 + \frac{\partial}{\partial x_j}\left[(\nu + \sigma_\omega\nu_T)\frac{\partial \omega}{\partial x_j}\right] + 2(1-F_1)\sigma_{\omega 2}\frac{1}{\omega}\frac{\partial k}{\partial x_i}\frac{\partial \omega}{\partial x_i} \tag{2.48}$$

where the kinematic eddy viscosity can be calculated from:

$$\nu_T = \frac{a_1 k}{\max(a_1\omega, SF_2)} \tag{2.49}$$

and the production of kinetic energy:

$$P_k = \min\left(\tau_{ij}\frac{\partial U_i}{\partial x_j}, 10\beta^* k\omega\right) \tag{2.50}$$

In the $k-\omega$ SST model the $k-\omega$ equations are multiplied by F_1 and the $k-\varepsilon$ equations by $(1-F_1)$ and then are added together to result the equations 2.47 and 2.48. ϕ_1 represents any constant in the original model $(\sigma_{k1},...)$, ϕ_2 any constant in the transformed $k-\varepsilon$ model (σ_{k2},...) and ϕ the corresponding constant of the new model (σ,...) and the relation between them is $\phi = \phi_1 F_1 + \phi_2(1-F_1)$. The function F_1 is designed to be one in the near wall region (activating the $k-\omega$) and zero away from the surface. The functions F_1 and F_2 are:

$$F_1 = \tanh\left\{\left\{\min\left[\max\left(\frac{\sqrt{k}}{\beta^*\omega y}, \frac{500\nu}{y^2}\omega\right), \frac{4\sigma_{\omega 2}k}{CD_{k\omega}y^2}\right]\right\}^4\right\} \tag{2.51}$$

$$F_2 = \tanh\left[\left[\max\left(\frac{2\sqrt{k}}{\beta^*\omega y}, \frac{500\nu}{y^2\omega}\right)\right]^2\right] \tag{2.52}$$

where $\beta^* = \frac{9}{100}$ is a model constant, y is the distance to the next surface and $CD_{k\omega}$ is:

$$CD_{k\omega} = \max\left(2\rho\sigma_{\omega 2}\frac{1}{\omega}\frac{\partial k}{\partial x_i}\frac{\partial \omega}{\partial x_i}, 10^{-10}\right) \tag{2.53}$$

The constants of set 1 and 2 are:

$$\alpha_1 = 5/9,\ \beta_1 = 3/40,\ \sigma_{k1} = 0.85,\ \sigma_{\omega 1} = 0.5$$
$$\alpha_2 = 0.44,\ \beta_2 = 0.0828,\ \sigma_{k2} = 1,\ \sigma_{\omega 2} = 0.856$$

2.5. COMBUSTION MODELING

As it was mentioned before, the main problem that arises from the mathematical modeling of turbulent combustion is how to approximate the interactions between the flow and the chemical reactions, the so-called turbulence combustion interaction. The mean species chemical production rates $\overline{S}_{k,\mathrm{chem}}$ that appears as source terms in 2.31 have to be modeled, as they are the driving force of turbulent combustion. The two models that were used in this thesis to model these rates will be briefly discussed, i.e the Eddy Dissipation Model (EDC) and the Eddy Dissipation Concept (EDC).

2.5.1. THE EDDY DISSIPATION MODEL

The majority of the fuels are fast burning. Due to the fact that the chemical reactions in most of these cases are very fast, it can be a valid assumption that the rate of combustion will be determined by the rate of intermixing provided by turbulence. In the case of non premixed flames, turbulence gradually mixes the fuel and the oxidizer into the main reaction zones, where they interact very fast. In the case of premixed flames turbulence provides the needed heat by slowly mixing the cold reactants and hot products into reaction zones, where reactions also occur very fast. Both of these cases are mixing-limited, and thus the complex, and often difficult to model, chemical kinetic rates are neglected.

The model that is founded on this assumption is called the eddy dissipation model and it is based on the work of Magnussen and Hjertager et al [35]. Thus, the net rate of production of species i due to reaction r, $\overline{S}_{i,r}$, can be given by the smaller (i.e., limiting value) of the two expressions below:

$$\overline{S}_{i,r} = \nu'_{i,r} M_{w,i} A\rho \frac{\varepsilon}{k} \min_R \left(\frac{Y_R}{\nu'_{R,r} M_{w,R}} \right) \tag{2.54}$$

$$\overline{S}_{i,r} = \nu'_{i,r} M_{w,i} AB\rho \frac{\varepsilon}{k} \frac{\sum_P Y_P}{\sum_j^N \nu''_{j,r} M_{w,j}} \tag{2.55}$$

where $\nu'_{i,r}$ is the stoichiometric coefficient for the reactant i in reaction r, $M_{w,i}$ is the molecular weight of reactant i, ε and k are the dissipation of the turbulent kinetic energy and the turbulent kinetic energy calculated by the turbulence model, Y_R is the mass fraction of the particular reactant R, $\nu''_{j,r}$ is the reverse reaction species stoichiometric coefficient, Y_P is the mass fraction of any product species P and, A and B are empirical constants equal to 4.0 and 0.5, respectively.

While this model is easily implemented and does not require intensive chemistry modeling, it is limited to one or two step mechanisms. More detailed mechanisms can be introduced, but usually this model produces incorrect solutions. Moreover, since every reaction has the same rate based on turbulence, kinetically controlled species such as radicals cannot be predicted. In order to overcome these deficiencies the eddy dissipation concept is introduced.

2.5.2. THE EDDY DISSIPATION CONCEPT

The EDC model was firstly introduced by Magnussen et al [36]. It is based on the assumption that combustion is infinitely fast and occurs inside fine structures. These fine structures are concentrated in isolated regions whose entire volume is but a small fraction of the total volume of the fluid. They are assumed to be in the same scale of magnitude as the Kolmogorov scale. These structures are governed by turbulence, and inside them it is assumed that reactants will be mixed at the molecular scale.

Therefore, in this model, the volume of the computational domain is effectively divided in two separate regions, the fine structures, where the reactants combust, and the surrounding volume. In the original formulation of the model, the fine structures are treated as Perfectly Stirred (PSR) Reactors since reactants are mixed on a molecular scale and mass is exchanged with the surroundings. However, ANSYS Fluent seems to treat the fine structures as Plug Flow Reactors (PFR) in order to reduce computational costs. Fluent is calculating the fine structure residence time based on Arrhenius rates that are integrated numerically in time [37]. The definition of the PFR model, involves the assumption that the fine structures are assumed spatially isolated structures in the fluid only evolving in time. Thus the solution of ANSYS Fluent is closer to PFR than PFR. The difference between the PSR and the PFR and its effects is mentioned in [38], [37], [39] and investigated in more detail by Bösenhofer et al [40].

In the EDC model, the net rate of production of species i due to reaction r, $\overline{S}_{i,r}$ is modeled as:

$$\overline{S}_{i,r} = \frac{\rho(\xi^*)^2}{\tau^*\left(1-(\xi^*)^2\right)}(Y_i^* - Y_i) \tag{2.56}$$

where ξ^* is the size of the fine structure, τ^* is its residence time and Y_i^* is the fine-scale species mass fraction after reacting over the time τ^*. These variables are based on the energy cascade concept and calculated as:

$$\xi^* = C_\xi \left(\frac{\nu\varepsilon}{k^2}\right)^{1/4} \tag{2.57}$$

$$\tau^* = C_\tau \left(\frac{\nu}{\varepsilon}\right)^{1/2} \tag{2.58}$$

where the volume fraction constant is $C_\xi = 2.1377$ and the timescale constant is $C_\tau = 0.4082$. These constants were refined by Ertesvag et al [41] and Gran et al [42].

Recently, efforts are being made to apply the EDC to MILD combustion simulations. The first approaches tried to modify the EDC model constants manually to improve results. However, these modifications were only applicable for specific cases and any notion of generality is lost [39]. However, Parente et al. [43] proposed a more sophisticated approach to adapt the EDC to the MILD combustion regime. In this model the model constants are position dependent variables, calculated via a local turbulent Reynolds number and a local Damköhler number. This models is called Extended-EDC, or E-EDC. Lastly, an improvement on Parente's E-EDC was proposed by Bao et al [44] and was named New Extended EDC, or NE-EDC. Based on Parente's idea and procedure and by eliminating the expression of laminar speed, a quantitative relation for the local model constants was derived. Results in a simulated furnace using the E-EDC and NE-EDC where reported by Romero-Anton et al [45].

2.6. COMBUSTION MECHANISMS

In order to accurately describe real combustion systems, a full description of the chemical reactions participating in flames must be made. However, chemical reactions during combustion may involve hundreds of species and thousands of reactions between them. Usually, the sheer number of variables in question demands the creation of combustion mechanisms to model these applications. There are three basic reasons that prohibit the resolution of real chemistry in CFD. Firstly, for each new specie introduced, an additional mass balance must be introduced as well. For example, a n-heptane, iso-octane and toluene detailed kinetic model for the simulation of gasoline surrogate fuels includes about 1550 species and 6000 reactions, thus 1150 more specie conservation equations to be solved [46]. Secondly, the reaction rates and the transport coefficients in chemical reactions are functions of temperature as well as mass fractions. With so many different realizable reactions the computational cost rises substantially. Lastly, the chemical reactions that occur during combustion have a wide range of time scales. This is a problem even for laminar flames, however, stiff equation solvers have been developed for it. Thus, the coupling between turbulence and combustion becomes increasing difficult since not a single turbulent time can be used and stiffness is introduced in the system.

Luckily, regardless the application, combustion mechanisms exhibit several characteristic properties, and their understanding can lead to simplifications of the chemical mechanisms by eliminating steps that are irrelevant at the applications conditions. These simplifications are usually referred as the quasi-steady state approximation and the partial equilibrium approximation [13],[47].

- *Quasi-steady state approximation (QSSA)*: Intermediate radicals that are very reactive can be assumed to react right after they are formed. They have reached an equilibrium state. Consequently, these species are not evolving anymore, their mass fractions can be considered constant and their reactions rates are negligible.

- *Partial equilibrium approximation (PEA)*: Analyses at high temperatures show that the reaction rates of forward and backward reactions are adequately fast and a partial equilibrium can be assumed. This way, the concentrations of very reactive species that are difficult to measure can be deduced from the knowledge of the stable species that are easier to measure.

In order to simplify the numerical treatment of the chemical kinetics, many methods have been devised, such as the assumption of an infinite reaction rate or one-step chemistry. These simple, few step mechanisms are called global mechanisms. While simple, the consideration of few reactions and species requires less usage of computer memory and leads to a very fast computation. Several tries have been made to create global reaction schemes for hydrocarbon combustion. Most notable contributions are from Jones and Lindstedt [48] and Franzelli [49]. Several attempts were made to optimize and compare global mechanisms [50], [51], [52]. However, pollutant formation (NO, soot, unburned hydrocarbons), as well as ignition and extinction are kinetically controlled processes, and oversimplified chemical schemes are not able to capture them. Thus, there is a need to create methods which simplify the chemistry mechanisms while still retaining the essential dynamic features of the reaction system. The global schemes nonetheless, provide decent and fast initial estimates for typical engineering applications.

For simple molecules, such as H_2 and CH_4, detailed mechanisms can created due to the fact that the number of possible species and reactions are limited. The most well-known detailed mechanisms are the GRI mechanisms created by the University of California at Berkeley [53]. GRI-Mech was calibrated and optimized in order to represent natural gas flames and ignition. It is essentially a list of elementary chemical reactions and their associated rate constant expressions. The majority of the reactions have been studied in the university's laboratory and thus, the rate constant parameters have have been the result of direct measurements. There are three versions of the mechanism. The GRI-Mech 1.2 is the oldest and consists of 32 species participating in 175 reactions [54]. Nowadays it is considered outdated and newer versions are suggested. The subsequent version 2.11 contains the chemistry identical to that of version 1.2 but adds 102 reactions of 17 additional nitrogen-containing species. It was developed in order to capture prompt NOx emissions for modern combustion systems. It has a total 49 species participating in 277 reactions [55]. Lastly, the latest version is GRI-Mech 3.0. It is an optimized mechanism designed to model natural gas combustion, including NO formation and reburn chemistry. Compared to the 2.11 version, several improvements were made to update the relevant kinetics with recent literature results, expand the mechanism and examine its sensitivity to the thermodynamics. Acetaldehyde and vinoxy chemistry are included to better describe ethylene oxidation and also because usually natural gas contains propane, a minimal set of propane kinetics was included. It consists of 53 species that participate in 325 reactions [56].

Using the aforementioned detailed mechanisms as a basis, the so-called skeletal or reduced mechanisms can be derived, either by identifying unimportant species or using the QSSA and PEA approaches. Various different approaches have been proposed over the years with the goal of determining the unimportant species or reaction paths [57],[58],[59]. Their main target is to propose a detail reaction mechanism and then thoroughly and systematically reduce it in size and stiffness. Because of the wide research room in this topic numerous mechanisms have been proposed in literature. Many of those have used the GRI mechanisms as a starting point due to its wide availability. Direct descendants of the GRI-Mech 1.2 are the DRM-19 and DRM-22 mechanisms. DRM-19 is a skeletal mechanism that consists of 19 species participating in 84 reactions and DRM-22 that contains 22 species and in total 104 reactions. Lu and Law [60] have also created several mechanisms, most notable for methane a 19 specie, derived from a 30 species and 184 reaction skeletal mechanism for methane-air reduced from the GRIMech 3.0. Notable early contributions where made by Smooke [61], with the creation of a 16-specie, 25 reaction mechanism and Kee [62], with the creation of the KEE58 mechanism, with 17 species and 58 reactions. Lastly, automatic chemical kinetic models and algorithms have been recently proposed with the creation of a 27 species mechanism based on laminar flame speeds by Chen [59].

2.7. RADIATION MODELING

In Section 2.1 the RTE was introduced as a means to calculate the radiative heat flux in a participating medium. A medium can be characterized by its optical thickness as $\tau_\eta = (\kappa_\eta + \sigma_{s\eta})s$, where s is the path length. An optically thin medium has $\tau_\eta << 1$ and an optically thick medium $\tau_\eta >> 1$. In order to solve the RTE, several solution methods were developed over the years for both optically thin and optically thick mediums.

2.7.1. SOLUTION METHODS

The most common methods to solve the radiative heat transfer problems are the Optically thin approximation, the Discrete transfer radiation model (DTRM), the P-1 radiation model, the Rosseland radiation model and lastly, Discrete Ordinates radiation model (DO).

The optically thin is pretty simplistic, and does not require the solution of the RTE. The optically thin approximation relies on the assumption that radiation in a thin medium is not scattered or self-absorbed. It provides a prediction of the radiative source term usually based on the Planck-mean absorption coefficient. While this method is computationally efficient and easy to implement, it should not be used if accurate radiative treatment is required [63].

The discrete transfer radiation model is a ray tracing method. The main assumption is that, after the discretization of a numerical domain, each surface element emits from its centre radiation, in certain discretized angles that can be can be approximated by single rays. At each radiating face, rays are fired at discrete values of the polar and azimuthal angles. The ray paths are pre-calculated and evaluated after each iteration along the incremental paths. The summation of the change in intensity along the path of each ray is the radiation source in the energy equation. A major drawback of this method is that it requires an adequately fine computational grid of radiating faces in order to satisfactory predict the radiative heat flux through the medium, since the number of rays coursing through each control volume cannot be quantified. However, it can be used in a wide range of optical thicknesses and its accuracy can be increased at the expense of computational cost by increasing the number of rays.

Another common method of treating the RTE is the spherical harmonics method. The most well-know approach is the so-called P-1 radiation model. The P-1 is the simplest case of the more general P-N model which is based on the use of spherical harmonics in order to transform the RTE into a set of partial differential equations. Any scalar function on the surface of a sphere of unit radius can be expressed in terms of a two-dimensional generalized Fourier series. In the P-1 model four terms in the series are used yielding one partial differential equation that is integrated over all directions. A great advantage of this method is that the transformed equations are relatively simple, however, low-order approximations are usually only accurate in media with near-isotropic radiative intensity. The higher order approximation of P-3 yields 16 equations and thus can be substantially more computationally expensive [15],[63].

The Rosseland model, or the diffusion approximation, is valid only for optically thick media, preferably with optical thickness over 3. It is based on the assumption that for thick enough media, radiative transfer can be modeled by an effective heat conductivity of the matter and can be can be approximated as an isotropic "diffusion" process [64]. With several approximations it can be derived from the P-1 model equations [21].

In the next section, the discrete ordinate method will be presented separately, as it is one of the most commonly used approximations when non-grey gas approximations are required.

2.7.2. THE DISCRETE ORDINATES METHOD

The discrete ordinates method is used in order to transform the radiative transfer equation (equation 2.24) into a set of partial differential equations. Its main goal is to transform the directional variation of intensity into a finite number of discrete solid angles, each associated with a vector direction $\hat{s}_j$ fixed in the global Cartesian system ($s = (x, y, z)$), that total the solid angle of 4π around a point in space. Then the finite differences or the finite volume approach can be used in order to solve the transformed directional intensity transport equations. The solution method is identical to the one used for the fluid flow and energy equations. In practice, equation 2.24 is solved for a set of n discrete directions $\hat{s}_i$, where $j = 1,2,...,n$ [15].

$$\begin{aligned}\frac{\partial I_\eta(s,\hat{s}_i)}{\partial s} =& \kappa_\eta I_{b\eta}(s) - \kappa_\eta I_\eta(s,\hat{s}_i) \\ & - \sigma_{s\eta} I_\eta(s,\hat{s}_i) + \frac{\sigma_{s\eta}}{4\pi}\sum_{j=1}^{n} w_j I_\eta(s,\hat{s}_j)\Phi_\eta(\hat{s}_j,\hat{s}_i)d\Omega_i,\end{aligned} \tag{2.59}$$

where w_i is the quadrature weights associated with the directions $\hat{s}_i$ [15].

The accuracy of the discrete ordinates method depends on the spacial and angular discretization methods employed. While the spacial discritization as described above can be a simple finite differences or finite volume scheme a careful approach must be considered concerning the angular discretization. For this purpose ANSYS Fluent employs octants in 2D and 3D space. Each octant of the angular space 4π is discritized into $N_\theta \times N_\phi$ solid angles called control angles. Due to symmetry only 4 octants need to be are solved. The angles θ and ϕ are the polar and azimuthal angles respectively, and the control angles for $\Delta\theta$ and $\Delta\phi$ are constant. Thus, for two dimensional systems $4N_\theta N_\phi$ directions will be solved in total. For three dimensional systems this due to symmetry again $8N_\theta N_\phi$ directions are solved. Moreover, in case of the employment of non-gray models the directions must be solved for multiple bands and thus, the computational cost is increased substantially [21].

2.7.3. RADIATIVE PROPERTIES OF GASES MODELING

All combustion applications involve multitudes of gases and other participating media. Thus, the modeling of radiative heat transfer with participating media is the the scope of many analyses to date [65], [66], [67]. This can be quite challenging because of the nature of the molecules involved. As mentioned before, molecular gases below dissociation temperature exhibit strong spectral variation of radiative properties. In order to model these properties several models have been introduced, mainly divided in four categories, the line-by-line calculations (LBL), the narrow band models (NBM), the wide band models (WBM) and the global models.

Line-by-line Calculations are is the most accurate way to calculate the radiative properties of gases. This method requires the detailed knowledge of every spectral line, which is usually obtained by spectral databases, resolves the RTE for each line and then integrates over the whole spectrum. Because of the extreme variability of the absorption coefficient, the RTE must be solved hundreds of thousands, or even millions of times, thus requiring enormous amounts of computational power. As it can be understood, the resolution of that many equations is prohibitive considering the fact that in turbulent combustion radiative transfer is only a part of the required computational power. However, this method is currently being used a benchmark in order to evaluate the accuracy of other models and the credibility of their assumptions.

Narrow Band Models are based on the division of the spectrum into bands and replacing it with averaged values of the required coefficients over the band. Their main assumption lies on the fact that in short spectral intervals, the Planck function can be considered constant. The RTE is solved with the coefficients of each division and then integrated over the whole spectrum. They can be very accurate and more computationally efficient than LBL calculations, however they are challenging to apply to nonhomogeneous gases, which is usually the case in combustion. The main narrow band approaches are the statistical band model and the correlated-κ distribution method. The correlated-κ distribution method is based on the fact that the absorption coefficient over the narrow band spectrum has the same value several time and therefore the RTE solution is the same. Taking this into account the integral over the spectrum can be represented by an integral over the absorption coefficient, with the advantage that the second integral is a smooth [68].

Wide Band Models rely on the assumption that across the entire vibration-rotation bands, the blackbody intensity does not vary substantially. The spectral lines of molecular gases are concentrated into certain regions and outside of these regions they do not interact with radiation. These models were very popular in the past because of their simplicity, the low computational needs and the lack reliable spectral data. On the other hand, they use an approximate shape of the bands and present an average error of 30% [15].

Global Models in contrast to the other models presented above attempt to calculate the total intensity of radiation $I(s)$ instead of the spectral intensity of radiation $I_\eta(s,\eta)$. That means, that RTE is firstly integrated over the whole spectrum and reduces to an equation for the total intensity and then is solved for the total intensity using spectrally integrated radiative properties. In the next sections the global models that were used for the scope of this thesis will be discussed.

2.7.4. THE WEIGHTED-SUM-OF-GREY-GASES MODEL

The simplest global model is the grey gas model. In this model the absorption coefficient is represented as a single value and it does not depend on wavenumber as seen in equation 2.24. For a detailed combustion analysis the simplification of a grey participating medium is not considered a good assumption since it fails to capture the influence of the vibration-rotation band, which in many cases make the value of the absorption coefficient wavelength dependent. Therefore, its use may lead to significant errors in the analysis of real gases.

The weighted-sum-of-grey-gases (WSGG) model was firstly presented by Hottel and Sarofim [69], within the framework of the zonal method, as a way to tackle the deficiencies of the simple grey gas model. This model involves the replacement of the gas with a multitude of grey gases and then independently calculates their emissivity. Subsequently, the emissivities are multiplied by weight factors and added together, so that the total emissivity can be obtained. It is considered a reasonable compromise between the oversimplified grey gas model and a complete absorption coefficient model which takes into account particular absorption bands.

In principle the WSGG models the total emissivity ε. The basic assumption is that the total emissivity of a gas layer of thickness s at a temperature T can be approximated using:

$$\varepsilon = \frac{1}{I_b(T)} \int \varepsilon_\eta I_{b\eta}(T) \approx \sum_{j=1}^{n} \alpha_j(T)(1 - e^{\kappa_j p s}) \tag{2.60}$$

where α_j is the grey gas weight, corresponding to each gas j, with $j = 0, 1, .., n$ based on gas temperature, T, and κ_j the grey gas absorption coefficient. The variable α_j can be interpreted as the summation of the blackbody spectral regions in which the effective pressure absorption coefficient is given by κ_j divided by the total blackbody radiation. P denotes the sum of the partial pressures of all absorbing gases. In the case of $j = 0$, the absorption coefficient is set to zero, to account for low absorption regions of the spectrum and the grey gas weight can be found from,

$$\alpha_0 = 1 - \sum_{j=1}^{n} \alpha_j \tag{2.61}$$

The emissivity weighting factors are temperature dependent and they are usually approximated as:

$$\alpha_j = \sum_{i=1}^{I} \beta_{j,i} T^{i-1} \tag{2.62}$$

The variables $\beta_{j,i}$ are polynomial coefficients that are estimated along with the absorption coefficients κ_j by fitting the emissivity equation 2.60 to emissivity experimental values. Thus the WSGG models result depends on the gas temperature, as well as its partial pressure.

Although the emissivity is soundly based on a summation of contributions from different bands, the standard use of this emissivity is to associate it with a 'total absorptivity'. For this to happen, a typical length scale, or 'mean beam length' must be adopted. This will be described in the next section.

WSGG RTE MODEL

Modest et al has demonstrated that the concept of weighted sum of grey gases may be generalized for use with any arbitrary solution method i.e. discrete ordinates [65]. In the presented comparisons of sample results with exact results, it was proven that the weighted-sum-of-grey-gases approach is equivalent, and moreover, that even very simple fits give very accurate results. In particular, it was shown that the parameters presented by Hottel et al, α_j and κ_j, appear as the coefficients in the RTE of a gray gas with constant absorption coefficient κ_j, with blackbody intensity I_b replaced by a weighted intensity $\alpha_j I_b$. Thus, the RTE for the j-th gas takes the form:

$$\frac{dI_j}{ds} = \kappa_j\big(\alpha_j \frac{\sigma T^4}{\pi} - I_j\big) \tag{2.63}$$

After it is solved by any standard solution method, the total intensity can be found by a simple summation over all grey gases. With this approach the very complicated case of an arbitrary non grey gas mixture can be reduced to the simultaneous solution of three or four representative grey media.

In order to calculate the required model coefficients, ANSYS Fluent uses the emissivity data obtained by [66], [70], [71]. These WSGG coefficients are derived for specific H_2O/CO_2 partial pressure ratios that correspond to complete combustion of different fuels under one atmospheric pressure. Smith et al. developed those formulations for pressure ratios of H_2O/CO_2 $p_{H_2O} = p_{CO_2} = 1$ and for temperatures between 600 and 2400 K. Fluent has integrated coefficients for 4 RTE WSGG formulations.

However,in his work, Hottel et al [69] states that for many purposes, a one-gray, one-clear gas approximation is adequate. Thus, instead of solving four RTEs as was the case in the original WSGG formulations, Fluent's domain-based WSGG model solves only one RTE to reduce the computational power needed. It uses the WSGG coefficients to calculate the gas mixture total emissivity using 2.60 and when the radiative intensity is calculated a single gray gas mixture absorption coefficient is used in the RTE solution estimated by [21]:

$$\kappa = -\frac{\ln(1-\varepsilon)}{s} \tag{2.64}$$

where $s = L_e$ is the corrected effective mean beam length calculated by:

$$L_e = 3.6\frac{V_{tot}}{A_{tot}} \tag{2.65}$$

with V_{tot} the total volume and A_{tot} the total surface area of the simulation domain.

Additionally, ANSYS Fluent offers the option to specify the gas layer thickness s. While the mean beam length is the recommended approach, especially when the modeled medium is homogeneous medium, a cell-based approach can be used by providing s based on the average length of the cells. However, in that case the predicted values of κ will be mesh dependent.

Fluent also allows users to solve multiple RTEs via a user defined function (UDF). Thus, a four-RTE WSGG model can be used in any arbitrary RTE solution method. This thesis uses both the built in method of the domain-based 1 RTE method and a 4-RTE method implemented via UDF.

2.7.5. THE SPECTRAL LINE-BASED WEIGHTED SGG MODEL

The spectral line-based weighted sum-of-grey-gases model (SLW) can be considered as an extension of the WSGG model. The main difference is that the absorption coefficients and their corresponding gas weights are evaluated from a line-by-line database. The calculation of these parameters is based on a global distribution function, named the absorption line blackbody distribution function or, in short, ALBDF [72].

ABSORPTION LINE BLACKBODY DISTRIBUTION FUNCTION

The ALBDF is the backbone of the SLW model and, in fact, constitutes most of the preliminary work of spectral integration, which makes the SLW a spectral model.

The creation of the ALBDF is conducted from high resolution absorption spectroscopic data (HITRAN or HITEMP) in advance, and is available in for different gas species, either in the form of mathematical correlations or, tabulated data.

The ALBDF is defined as the fraction of the blackbody emissive power $E_b(T_b) = \sigma T_b^4$ that lies in the part of the spectrum where the the absorption cross section $C_\eta(T_g)$ at the gas thermodynamic state φ_g is less than the prescribed value C [72]:

$$F\left(C, \varphi_g, T_b\right) = \frac{1}{E_b(T_b)} \int\limits_{\left\{\eta : C_\eta(\varphi_g) < C\right\}} E_{b\eta}(T_b)\, d\eta \tag{2.66}$$

where $\varphi_g = \left\{T_g, X, p\right\}$, with T_g the temperature of the gas, X the mole fraction and p the total pressure. Additionally, T_b is the source temperature.

The molar absorption cross-section is related to the absorption coefficient by:

$$C_\eta = \frac{RT_g}{pX} \kappa_\eta \tag{2.67}$$

with R the universal gas constant [19].

The ALBDF is a strictly increasing function, and thus, by inversing it, an ALBDF function $C\left(F, \varphi_g, T_b\right)$ of the independent variable F is created, which can be considered as a reordered absorption cross section. The visualization and geometrical meaning of the ALBDF and the inverse ALBDF are illustrated in Figure 2.6.

THE SLW MODEL

In order to construct the SLW spectral model, the subdivision of the continuous gas absorption cross-section must be implemented into a number n of discrete grey gases. This is achieved by introducing supplemental cross sections ($\tilde{C}_j$) which are discretized logarithmically based on a minimum (C_{min}) and maximum value (C_{max}). These values are chosen in such way that they capture the variation of the entire absorption cross section. Thus, the supplemental cross sections $\tilde{C}_j$ that exist between $\tilde{C}_0 = C_{\text{min}}$ and $\tilde{C}_n = C_{\text{max}}$ are calculated as [66]:

$$\widetilde{C_j} = C_{\text{min}}\left(C_{\text{max}}/C_{\text{min}}\right)^{j/n}, j = 0, 1, ..., n \tag{2.68}$$

A graphical representation of this procedure is illustrated in Figure 2.7

In media that are isothermal at uniform temperature T_g and homogeneous with mole fraction X, the integration of the spectral RTE over the wavenumbers corresponding to the gray gases results the multiple gray gas form of the RTE 2.63. Thus,

$$\begin{gathered} \frac{dI_j}{ds} = -\kappa_j I_j + \alpha_j \kappa_j I_b, \quad j = 1, ..., n \\ \frac{dI_j}{ds} = 0, \quad \text{for a clear gas} \end{gathered} \tag{2.69}$$

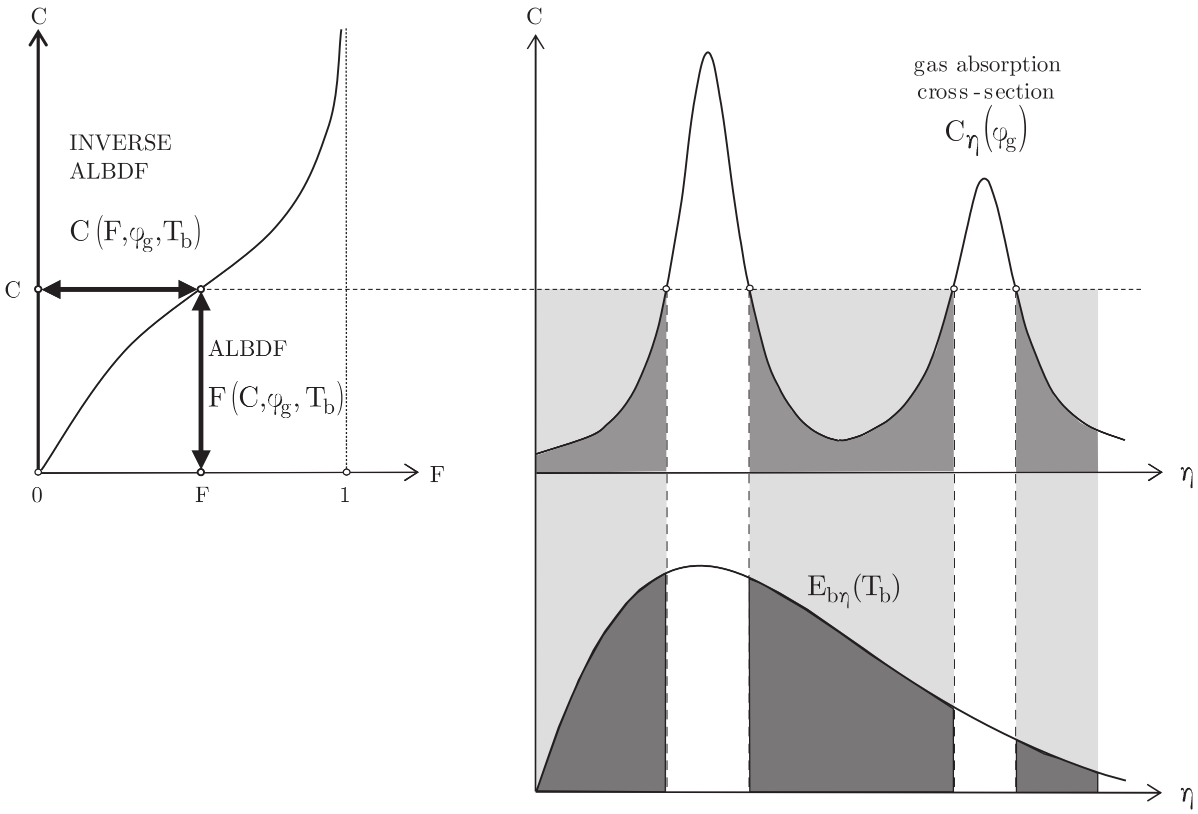

Figure 2.6: Definition of the direct ALBDF and its inverse [18].

2

where the created supplemental cross sections are used in order to calculate the absorption coefficient by:

$$\begin{aligned} \kappa_j &= NX\sqrt{\tilde{C}_{j-1}\tilde{C}_j}, \quad j = 1,...,n \\ \kappa_0 &= 0, \quad \text{for a clear gas} \end{aligned} \tag{2.70}$$

and the grey and clear gas weights for $T_b = T_g$ are calculated based on the inverse ALBDF as:

$$\alpha_j = F\big(\tilde{C}_j, \varphi_g, T_g\big) - F\big(\tilde{C}_{j-1}, \varphi_g, T_g\big) \text{ and } \alpha_0 = F\big(\tilde{C}_0, \varphi_g, T_g\big). \tag{2.71}$$

Subsequently, the RTE is resolved for the number of grey gases selected, the resulting intensities are added and the total intensity is finally computed.

REFERENCE APPROACH

The method presented so far is only applicable for uniform media. In order to use the SLW model in cases with non-uniform media, such as in most combustion applications, an extension to the model must be developed. The added complexity in non-uniform media comes from the fact that the absorption coefficient varies with spatial location, since the thermodynamic gas state φ_g also varies with location.

The grey gas wavenumber intervals are denoted in Figure 2.7 as $\Delta\eta_{i-j}$ and are the wavenumbers corresponding to the selected gray gases. In the case of variance in φ_g with fixed supplemental cross-sections, different wavenumber intervals appear: $\Delta\eta_j(s_1) \neq \Delta\eta_j(s_2)$, where s_1 and s_2 refer to positions with different thermodynamic state (e.g temperature) leading to complicated extra terms (Leibnitz terms). In order to tackle that problem, a possible solution is to use constant fixed spectral intervals must be specified. The fixing of grey gas intervals can be implemented by choosing different supplemental cross sections at different location in such a way that they define the same spectral intervals for all locations. This approach is called the reference approach and is based on the assumption of correlated spectra, or ideal spectra behaviour [66].

The ideal spectral behaviour assumes that any arbitrary state can be correlated with a reference state, such that for a value of the reference cross section C^{ref} exists a local state C^{loc} such that the wavenumber intervals are the same. This practically means that since the intervals are equal, the values of the ALBDF for C^{ref} and C^{loc} will be the same for $T_b = T_{\text{ref}}$, thus:

$$F\left(\tilde{C}_j^{\text{loc}}, \varphi_{\text{loc}}, T_{\text{ref}}\right) = F\left(\tilde{C}_j^{\text{ref}}, \varphi_{\text{ref}}, T_{\text{ref}}\right) \tag{2.72}$$

In practice the reference approach can be implemented by choosing a reference thermodynamic gas state $\varphi_{\text{ref}} = \{T_{\text{ref}}, X_{\text{ref}}, p_{\text{ref}}\}$ and a set of reference supplemental cross sections $\tilde{C}_j^{\text{ref}}$. Then the local supplemental cross sections $\tilde{C}_j^{\text{loc}}$ can be calculated using the inverse ALBDF. Furthermore, the local grey gas absorption coefficients can be calculated using:

$$\kappa_j(s) = N(s)X(s)\sqrt{\tilde{C}_j^{\text{loc}}\tilde{C}_{j-1}^{\text{loc}}} \tag{2.73}$$

and the local weights,

$$\alpha_j(s) = F\left(\tilde{C}_j^{\text{ref}}, \varphi_{\text{ref}}, T(s)\right) - F\left(\tilde{C}_{j-1}^{\text{ref}}, \varphi_{\text{ref}}, T(s)\right) \tag{2.74}$$

and finally, the gray gas RTE can be solved as before for each gray gas and the summized.

In the case multitudes of gases are present in the simulation, the SLW method transforms them into a single gas with absorption coefficient defined as [73]:

$$\kappa_{\eta,\text{mix}} = N X_m C_{\eta,m} \tag{2.75}$$

with $m = 1,2,..,k$ and k the number of species participating in radiative heat transfer.

Supported gases of the SLW Reference approach used in this thesis are CO_2, H_2O and CO.

The SLW code that was used in the context of this thesis was developed and provided by professor Brent W. Webb. It is coupled with ANSYS Fluent using a User Defined Function and other ancillary files. It includes capability for RA-SLW and other SLW models.

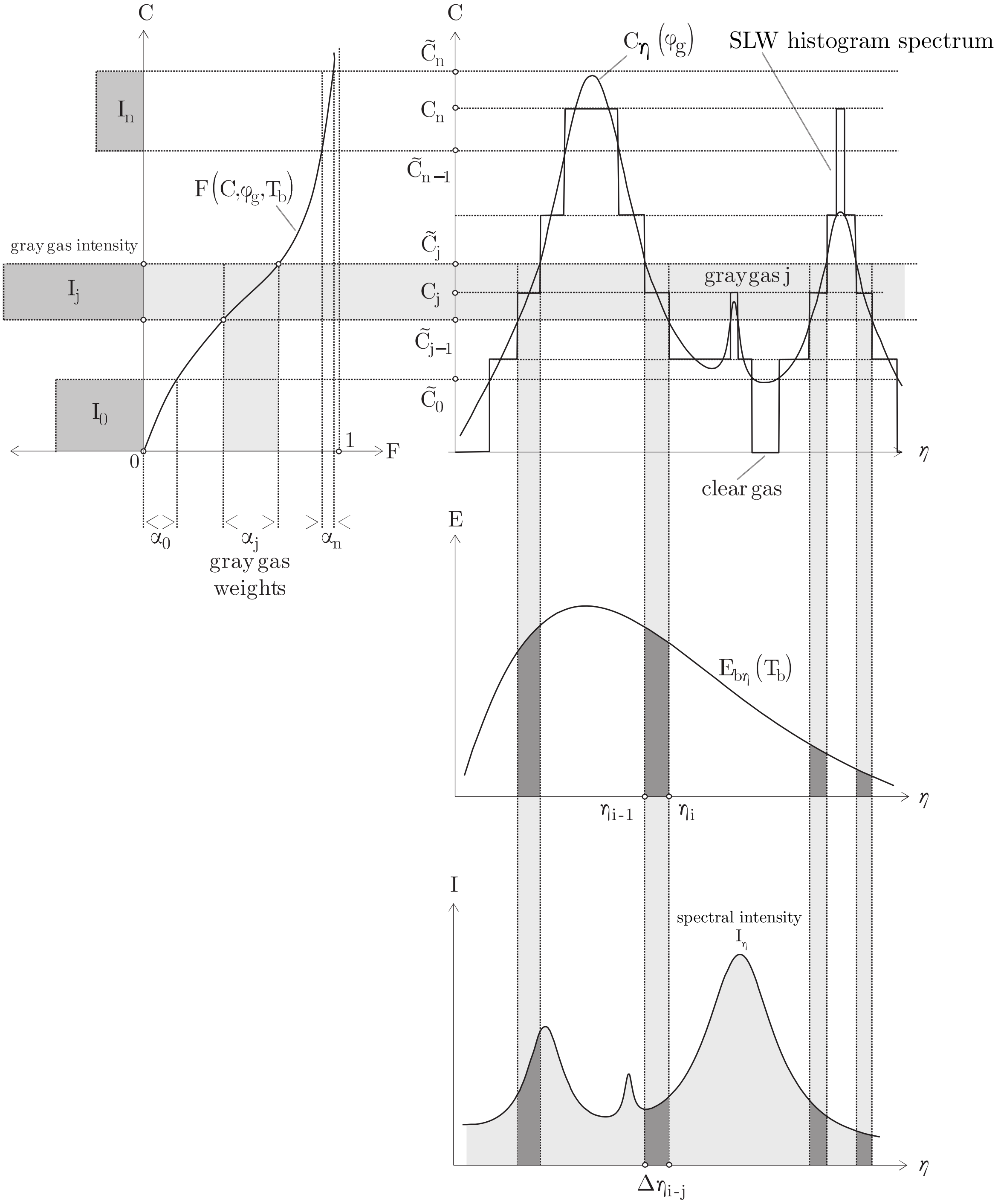

Figure 2.7: Graphical illustration of the SLW model [18].

3

CFD RADIATION ANALYSIS OF AXISYMMETRIC FURNACE

The objective of this thesis is the comparison of different radiation, turbulence and chemistry models, and their assessment for use in the flameless combustion regime. While the effect of turbulence and chemistry models have been investigated in previous works, ([4], [39], [74], [75]), the effects of accurately modeling the gas properties have not been evaluated thoroughly. In order to evaluate them, an axisymmetric oxy-combustion furnace was simulated.

Oxy-combustion or oxy-fuel combustion is considered as one of the best candidates to replace the current combustion systems and has been investigated for a number of years for various types of fuel. In principle, in an oxy-combustion system an oxygen stream is introduced instead of air. Sometimes, it is diluted with CO_2 which acts a diluent but also acting as an oxidizing agent to react with the fuel. The exhaust gases produced by oxy-fuel combustion are, thus, primarily CO_2 and H_2O. After combustion, the produced water vapour can be condensed and thus, the remaining high CO_2 concentration stream can later be sequestered, recycled, reintroduced into the combustion chamber, or used for different applications.

In most simulations of furnaces the detailed modeling of radiative heat transfer is omitted and instead, more detailed simulations of turbulent mixing and reactions are preferred. This stems from the fact, that the consideration of spectral variations of radiation properties increases the difficulty of an already extremely difficult problem and usually makes its numerical solution considerably more computer-time intensive. For this reason simpler and more accessible models are usually used to model these properties, such as the WSGG model, which is usually already built into commercial CFD codes.

However in recent years, some studies have assessed the performance of more detailed radiation models in combustion systems [76], [77]. Yin et al investigated an advanced WSGG model based on an exponential wide band model [78]. Krishnamurthy et al conducted experiments and numerical studies in coal-fired oxy-combustion systems and investigated the effect of gray and non-gray radiation modeling use [79], [80]. Porter et al evaluated solution methods, as well as grey and non-grey models [81]. Chu et al evaluated a multitude of models that estimate the radiative properties of gases at various pressures: among them line-by-line, SLW and WSGG models. In his work in a laboratory-scale furnace, combustion calculations of an axisymmetric jet diffusion flame where conducted [82].

Andersson et al [83] reported experimental results from a 100 kW test facility, located in the Chalmers University of Technology. This facility consists of a cylindrical refractory-lined furnace which includes a burner that creates a fuel lance surrounded by cylindrical primary and secondary feed registers. Fuel and oxidant are supplied via supply pipes at the required pressures and temperature. The gases flow in parallel, the oxidizing agents are swirled and meet towards the tip of the burner. Due to the design of the burner, the combustion regime is non-premixed combustion. These experiments were designed to explore soot formation and its effect on radiative transfer. However, in one occasion the flame was not luminous and thus, radiation was not influenced by soot, making it an interesting case in order to investigate the contribution of radiating gases to the overall radiative transfer. Similar studies in this furnace where conducted by Hjartstam et al [84], Gunnarsson et al [85] and Webb et al [86], [87]. The study that will be presented in this chapter was based on the study of Webb et al [86] with the objective of evaluating the importance of detailed radiation analysis in a non luminous, soot-free combustion regime.

3.1. AXISYMMETRIC OXY-COMBUSTION FURNACE

The Chalmers 100 kW oxy-fuel test apparatus consists of a cylindrical furnace with an inner height of 2400 mm and inner diameter of 800 mm. Inside the furnace, four water-cooled tubes are placed symmetrically close to the wall, so that the furnace temperature can be adjusted to simulate conventional combustion processes. The swirl burner is mounted at the top and is fired downwards. The burner consists of a central gas lance, from which fuel is introduced, and two annular primary oxidizing agent feeds that have swirl angles of 45° and 15° for the primary and secondary air feeds, respectively. The fuel inlet has a diameter of 34 mm, the primary feed an outer diameter of 52 mm and the secondary feed an outer diameter of 92 mm. The gases flowrates are controlled by high precision mass flow. Several measurement ports (M) are located at different axial distances, or planes, allowing ease of access for measurements. The apparatus also allows for flue gas recirculation and it can be operated in oxy-fuel mode, in which nitrogen in the air is replaced by carbon dioxide from the flue gases. Moreover, the addition of other compounds, i.e. NO or SO_2, can be achieved and thus, allowing investigation of the influence of such additives in combustion. Detailed schematics of the apparatus and the burner are presented in Figures 3.1a and 3.1b.

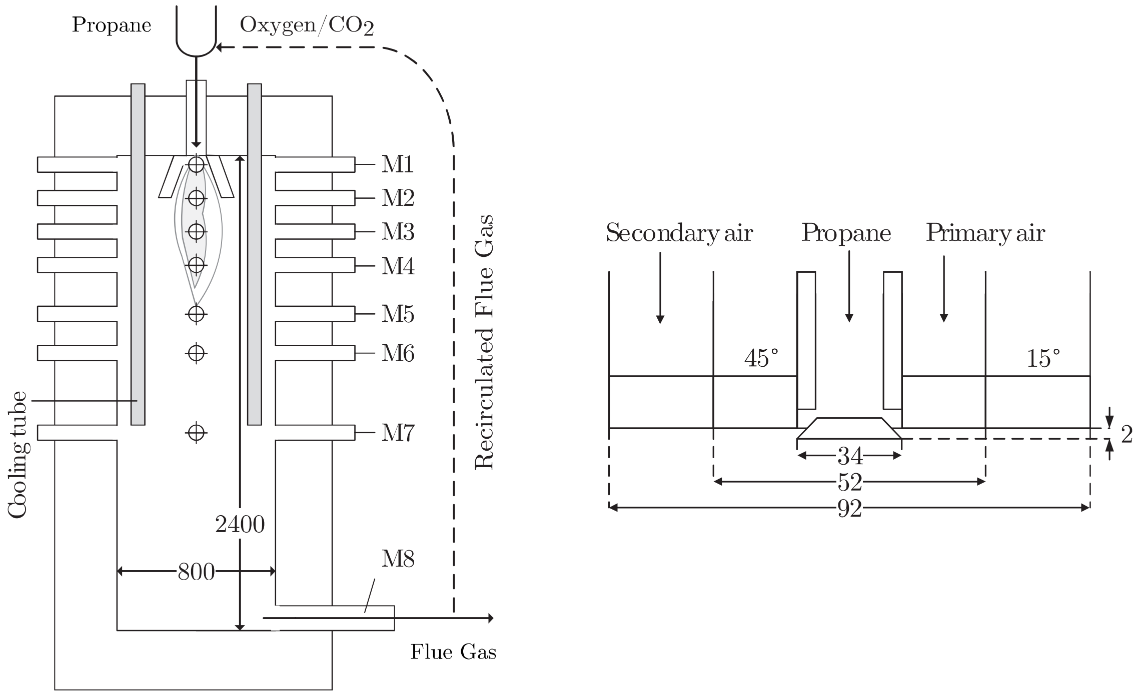

(a) (b)

Figure 3.1: a. Schematic of the Chalmers 100 kW test apparatus. b. Schematic of the swirl burner with swirl angles and dimensions in mm [85].

3.2. CASE DESCRIPTION AND MODEL CONFIGURATION

3.2.1. CASE DESCRIPTION

In this apparatus, oxy-combustion experiments were conducted using propane as fuel. Three different sets of experiment are reported, of which the two are conducted in oxy-fuel mode and one with air [83]. In particular, in the oxy-fuel mode the recirculated flue gas system was used to supply the feed stream. The oxidizing agent, that is injected through the burner, is created as such: After combustion, the resulting flue gases pass through a flue-gas cooler, a fabric filter and a condenser, where it is cooled to 20–30 ^oC. Part of the resulting gas is then mixed with fresh oxygen and fed to the combustion chamber through the primary and secondary registers of the burner. All of the experiments were conducted at a stoichiometric ratio (λ) of 1.15.

Of the total three experiments, the two presented highly luminous flames and thus, the effect of soot cannot be considered negligible. The single case that did not present a luminous flame was fed with 21% oxygen in oxy-fuel mode. This case can be considered very interesting in terms of accurately modeling the gas role in radiative heat transfer, since nitrogen, which is radiatively non-participating, is absent and oxy-combustion involves very high concentrations of CO_2, which is radiatively participating . Thus, accurate treatment of the gas properties of CO_2, is expected to play a pivotal role in the calculation of radiative heat transfer. In the context of this thesis, this case was analyzed and modeled, focusing on the contribution of radiating gases to the overall radiative transfer. The contribution of soot was assumed to be negligible and therefore is not included in the calculations of turbulent combustion. The experiment's conditions are presented in Table 3.1.

Table 3.1: Experimental variables

Fuel			**Feed gas**		
C_3H_8	98.30	[vol %, dry]	O_2	21.00	[vol %,]
Butanes, Ethane,etc	1.70	[vol %, dry]	CO_2	79.00	[vol %]
Stoichiometric ratio	1.15		Primary feed gas flow	37	[m_n^3/h]
			Second. feed gas flow	54	[m_n^3/h]
Swirl settings			**Gas Temperatures**		
Primary register fin angle	45	[°]	Fuel Temperature	300	[K]
Secondary register fin angle	15	[°]	Feed Temperature	300	[K]

During the experiments, temperature and gas composition were measured. The radial profiles of the flame temperature were measured using a water-cooled suction pyrometer equipped with a type B thermocouple. In order to minimize radiation losses from the thermocouple junction, a suction velocity of about 150 m/s was applied. The gas samples were collected with a water-cooled suction probes, were dried and analyzed using a gas analyzer.

3.2.2. MODEL CONFIGURATION

For the modeling of this case the commercial CFD code ANSYS Fluent 19.2 was used. Due to the symmetrical nature of the Chalmers apparatus, a 2D axisymmetric geometry can be assumed. Using this geometry RANS modeling studies are conducted in order to estimate the furnace temperature, the gas concentrations and the effect of the radiative heat source. A similar study was conducted by Webb et al [86], [87] in order to demonstrate the use of the SLW model and assess its accuracy. The computational domain for this thesis is created in ANSYS Design Modeler and is presented in Figure 3.2.

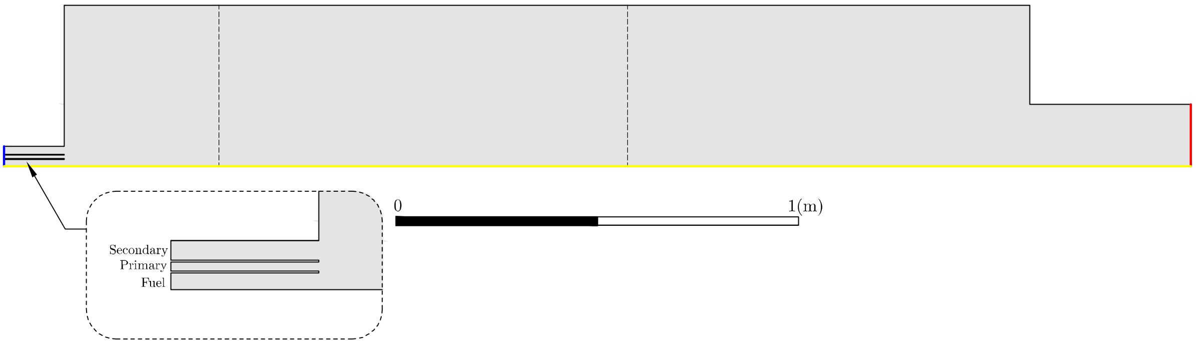

Figure 3.2: Geometry used for the axisymmetric simulation.

In order to take advantage of the axisymmetry, only half of the domain is created in the radial direction. The computational domain is one half of the vertical midplane of the furnace and extends for 2400 mm in the axial direction and 400 mm in the radial direction. Moreover, the inlet is extended upstream by 150 mm to let the flow fully develop by the time it reaches the combustion chamber. Furthermore, due to the fact that the wall thickness between the fuel inlet, the primary inlet and the secondary inlet is not specified in the original study, a 2 mm gap is introduced. Finally, the outlet is extended downstream by 400 mm in order to avoid reverse pressure gradients inside the combustion chamber. In Figure 3.2 solid walls are indicated in with black colour. The symmetry axis is indicated with yellow colour and the outlet with red. The dashed lines represent the $x = 384$ mm and $x = 1400$ mm planes, on which most of the results will be represented.

Mesh

One of the most essential components in any RANS simulation is an adequately fine mesh. For this case a quadrilateral constructed mesh was created, parts of which are presented in Figure 3.3. This grid was constructed in ANSYS Fluent Meshing tool. To guarantee better accuracy in the simulation results, 145950 high-quality quad mesh cells were created with clustering in the flame region. Combustion is expected to occur after the gases start to mix in the region upstream of the fuel, primary and secondary inlets. Due to the swirling nature of the flow, the clustering is extended radially up to 150 mm. This is shown in Figure 3.3a. The detailed clustering is presented in Figure 3.3b.

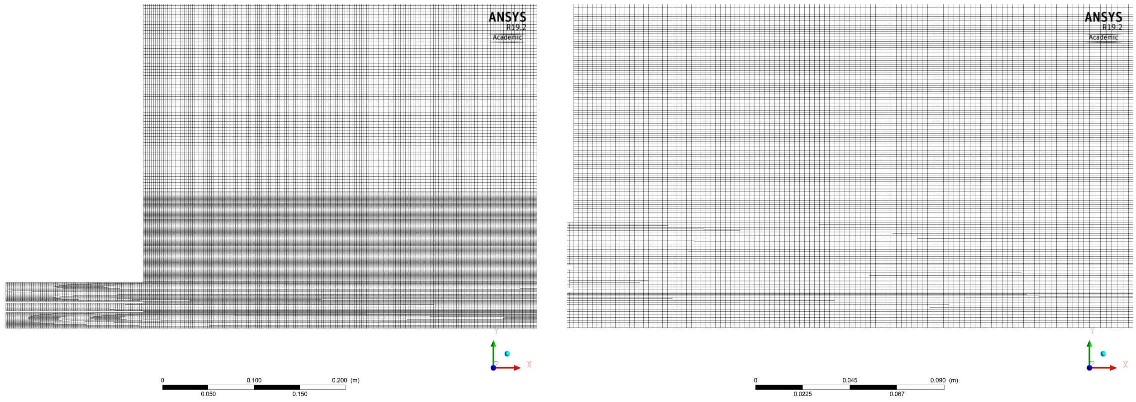

(a) Grid in flame area.

(b) Clustering in the flame area.

Figure 3.3: Grid used for the simulation of the axisymmetric furnace.

A grid independence study is conducted in order to assess the importance of the grid discretization on the solution. The very fine mesh of $145,950$ cells is reduced to a fine mesh of $58,390$ cells and further reduced in a coarse mesh of $19,360$ cells. The results on the radial temperature profiles are presented in Figure 3.4. It can be observed that, on a coarser grid, the temperature profile trends remains similar. All cases in 3.4a present a raise in temperature at approximately $y = 0.05$ m and then a sharp drop. The coarse mesh presents lower temperatures overall, however the difference is very small. Similarly for 3.4b, in all meshes the trend remains similar and the coarse mesh presents a slightly lower temperature overall. Since these changes do not significantly alter the solution, the results can be considered mesh-independent. The difference in computational expense for all the aforementioned grids is not great and since simple models are used for the turbulence and chemistry modeling, the very fine mesh is used for the remainder of the simulations. For comparison, Webb et al, while simulating the same case with similar settings used a mesh of $67,611$ cells [86].

Boundary Conditions

The inlet is illustrated in Figure 3.2 with blue color. The propane enters the computational domain from the fuel inlet and the required propane amount is calculated

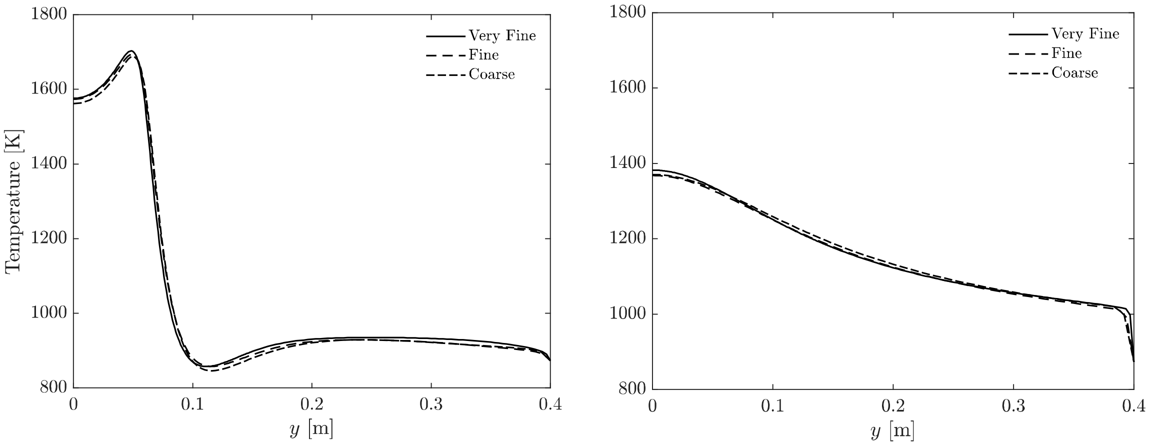

(a) $x = 384$ mm

(b) $x = 1400$ mm

Figure 3.4: Mesh effects on the temperature calculations

from the primary and secondary oxidazing agent for stoichiometric ratio, $\lambda = 1.15$. For the case simulated in the context of this thesis, the recycled flue gas is 21% oxygen and 79% carbon dioxide (by volume) and is injected into the burner at 300 K. The flow rate for the primary oxidant register is 37 m^3/h and for the second register is 54 m^3/h, both at standard conditions. The flow rate of propane was determined based on the density of the recycled flue gas mixture which was calculated using REFPROP at 300 K at 1.669 Kg/m^3. The calculated mass flowrate was approximately 1.638 g/sec. The content of the fuel stream was assumed 100% propane.

In order to accurately simulate the swirl angles, the primary and secondary feeds are specified using a direction vector. For the primary feed, the axial component of the flow direction is 0.707 and the tangential is 0.707, based on the 45^o angle and for the secondary feed the axial component 0.9659 and the tangential 0.2566 for the 15^o angle. The fuel feed was specified as normal to boundary. For the turbulence specification method, the turbulence intensity and the hydraulic diameter were specified. The hydraulic diameter was calculated based on the annular diameters. The Turbulent Intensity was calculated as described in the ANSYS Fluent guide using the Reynolds number based on the hydraulic diameter as such [21]:

$$I = 0.16(\mathrm{Re}_{D_H})^{-1/8} \tag{3.1}$$

Using this equation, the resulting turbulent intensity that is used for all inlets is 5%.

Inside the furnace, which has refractory-lined walls, there are four cooling tubes of unknown dimensions. These cooling tubes were inserted axially along the walls and were used in order to adjust the flame temperature. However, no wall temperature or wall emissivity was reported. Thus, to effectively simulate the furnace, an arbitrary wall temperature and emissivity must be assumed. The assumed temperature and gray emissivity are 873 K and 0.8 respectively and were elected after evaluating the first simulations. For these values, the calculated temperatures near the wall did not affect the solution. Additionally, the burner wall surface and the inlet extension was assumed adiabatic. Finally, the shear condition in all walls was assumed no-slip.

Models

Due to the fact that this case is based on the work of Webb et al, the same turbulence and chemistry models are employed. As such, the standard $k-\varepsilon$ model was used to model the turbulent flow field. ANSYS Fluent provides the possibility to change the model constants, however this option was not exercised. In conjunction with the standard $k-\varepsilon$ model, standard wall functions were assumed, in order to treat the flow near the walls. The chemistry was modeled using a simple two-step global model for propane reaction. The two-step mechanism involves the creation of carbon monoxide (CO) and is one of ANSYS Fluent's proposed models for simple propane combustion denoted as propane-2-step. The chemical reactions are:

$$C_3H_8 + 3.5O_2 \rightarrow 3CO + 4H_2O \tag{3.2a}$$

$$CO + 0.5O_2 \rightarrow CO_2 \tag{3.2b}$$

The gases that participate in these reactions were assumed ideal gases and all their properties were obtained based on ideal gas mixing laws, with the exception of the radiative properties which will be discussed below. The reactions are volumetric and in order to model the turbulence-chemistry interaction the eddy dissipation model (EDM) was used.

The solution of radiative heat transfer equation was calculated using the discrete ordinates method. In order to model the angular discretization needed for the DO method, four θ and ϕ divisions and two θ and ϕ pixels were chosen. Moreover, 10 energy iterations are performed for each radiation iteration to speed up the solution. The radiative gas properties modeling, which is the focus of this study, was conducted using the domain-based WSGG, a 10-RTE (10 grey gases) SLW model with tabulated ALBDF data [18] and a cell-based WSGG, in which the gas layer of thickness s is provided by the average length of the cells. A case with no radiation treatment was also created, in order to provide a benchmark for comparisons between the different models.

Lastly, it is important to mention all the discretization schemes used for the solution of the case. The pressure-velocity coupling was computed using the SIMPLE algorithm. The spacial discretization for the gradient was evaluted with the least squares cell based method, in which the solution is assumed to vary linearly. For the spacial discretization of the pressure, density, momentum, swirl velocity, turbulent kinetic energy, turbulent dissipation rate, energy, discrete ordinates and species, the second order upwind scheme was employed. The simulations were run until the residuals for all resolved quantities became constant over a couple of thousand iterations. The residuals of all the variables decreased for up to five orders of magnitude. In addition to that, the convergence was monitored via checking the resulting contours of the turbulent flow to ensure steady state.

3.3. RESULTS AND DISCUSSION

In this section, the results of the simulated case are presented and compared. In Figure 3.5, a temperature contour, resolved with the use of the domain-based WSGG, is presented. In this Figure the cold fluid enters the domain and combusts. The flame structure is visible and additionally two planes PL1 and PL2 are presented, at $x = 348$ mm (PL1) and $x = 1400$ mm (PL2), on which the numerical data will be later described. These contours can be used to draw some qualitative remarks regarding the simulated reacting flow. In Figure 3.5, (i) an ignition region can be observed where the fuel firstly interacts with the primary oxidant, (ii) a cooling blanket where the primary and secondary oxidant are still not fully mixed with the fuel, (iii) a core in which reactions are taking place and (iv) a cylindrical region with the highest temperature and where, near stoichiometric combustion is taking place. The first plane, PL1, is crossing the main combustion region and therefore, high temperatures are expected to be present. The second plane, PL2, is right at the tip of the end of the combustion region and thus, a more uniform temperature profile is expected.

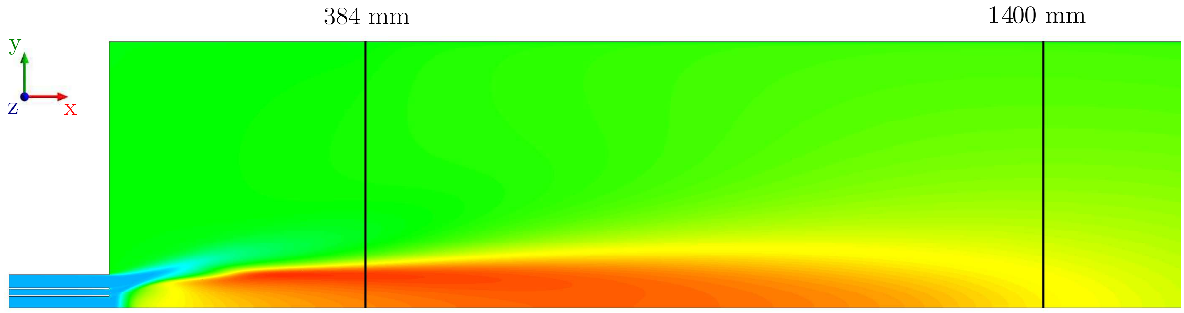

Figure 3.5: Temperature contour denoting the planes represented in the results. The radiation properties model is the domain-based WSGG.

In Figures 3.7, to 3.12, the temperature profiles, the species mole fractions and the radiative heat source will be presented using:

1. A domain-based WSGG model (DB).
2. A 10-RTE SLW model with tabulated ALBDF data (SLW).
3. A cell-based WSGG model with the average cell length (CB).
4. A WSGG model extracted from Webb et al (DB-Webb).
5. A SLW model extracted from Webb et al (SLW-Webb).
6. A case with no radiation treatment (No-Rad)
7. The experimental results

The DB results are represented with red lines, DB-Webb with red dashed lines, SLW with blue lines, SLW-Webb with blue dashed lines and CB with yellow lines. Furthermore, the case with no radiation treatment is represented with black dashed lines and will be provided as a benchmark. The experimental data reported by Andersson et al [83] are presented as grey points. Additionally, it was reported that H_2O and CO_2 concentrations were at the stoichiometric values for complete combustion at PL2, and are represented by grey lines. Here, it must be noted that the experimental values are included in the figures to provide a more complete view of the actual variations of the measured variables. However, the aim of this current work is not to comprehensively predict the combustion process. Rather than that, the goal is to identify the differences among the aforementioned radiation models and to determine the importance of modeling the radiative properties of the participating gases in detail.

Generally, as it will be evident in the following sections, the CFD predictions differ from the experimental measurements by a large margin. This difference can be explained by several factors.

- Firstly, one of these factors is the lack of adequate burner design description. Therefore, the fuel inlet temperature and actual fuel flow had to be estimated.
- Another factor is the use of simple models for the chemistry and turbulence modeling. The two-step global mechanism, while adequate to get an engineering estimate in a time efficient matter, fails to capture the entirety of the complex turbulent combustion phenomenon. Moreover, due to the lack of information about the flow field (i.e. velocity profiles, a pressure profile) the choice of a turbulence model cannot be easily justified.
- Lastly, the use of the EDM for turbulence chemistry interaction assumes that the rate of reaction is controlled by turbulent mixing. While this can be the case for ordinary flames, in the case of non-luminous, oxy-combustion flames, the more complex EDC model, or other more advanced models are preferred.

In order to better understand the effects of the absorption coefficient modeling that will be presented in the following sections, the contours of the absorption coefficient for the cell-based WSGG method and the domain based WSGG are presented (Figure 3.6).

The contour of the the SLW model is similar to the contours of DB WSGG model (except at certain regions) and is not presented for brevity. As it is evident from the aforementioned contours, the cell based method estimates absorption coefficients that are two orders of magnitude greater than the domain based method. Especially for the region that the flame is not present, and thus is mostly carbon dioxide and water, the absorption coefficient is 0.3 and 13.5 for the DB and CB, respectively. Higher absorption coefficients indicate more radiative heat transfer and thus, in the case of the cell based WSGG more uniform temperatures are generally expected, as well as higher absolute radiative heat source.

3.3.1. Effect on temperature

Figures 3.7, 3.8a and 3.8b show the temperature profiles along the axis and along the planes PL1 and PL2. In terms of estimating the temperature, modeling radiative properties seems to have a strong influence on the temperature profile.

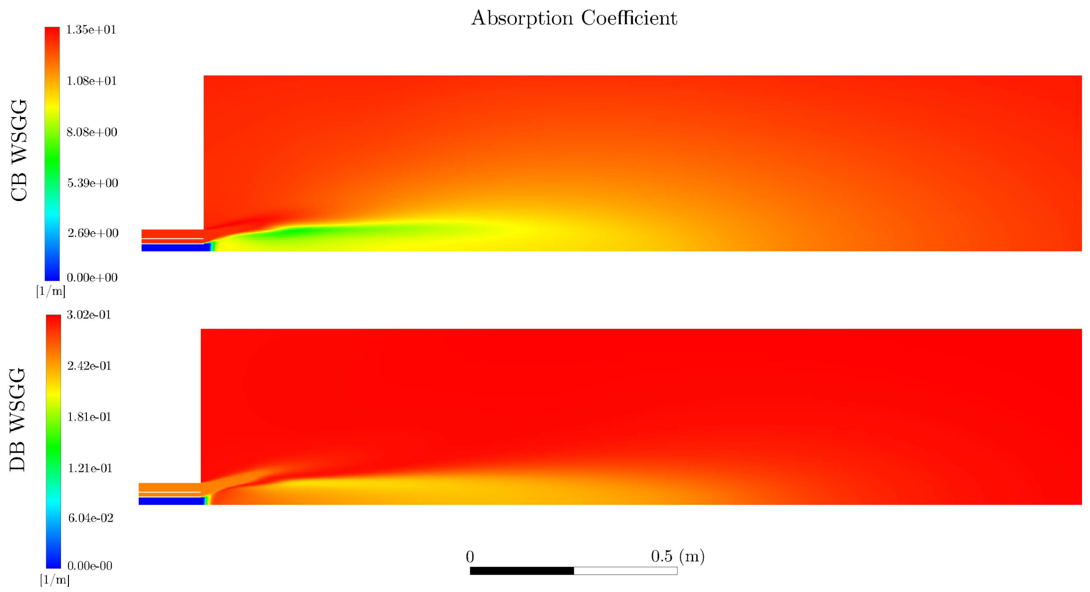

Figure 3.6: Absorption coefficient contour for the DB and CB WSGG model.

In Figure 3.7, all simulations present a steep increase in temperature which is then followed by a decrease due to the mixing with the bulk flow. The DB and the SLW models show small differences to one another, both in this work and on the work of Webb et al. In his work, the decrease is steeper and the overall resulting temperature is lower. The CB method, due to the overall higher absorption coefficients, predicts a flatter profile and more uniform temperatures compared to the other models. Inversely, in the case when the radiation is not treated, the resulting temperature is extremely high and remains high in the whole domain. As it is evident, the temperature along the axis depends heavily on the treatment of the radiative properties, with the CB model resulting in lower temperatures overall.

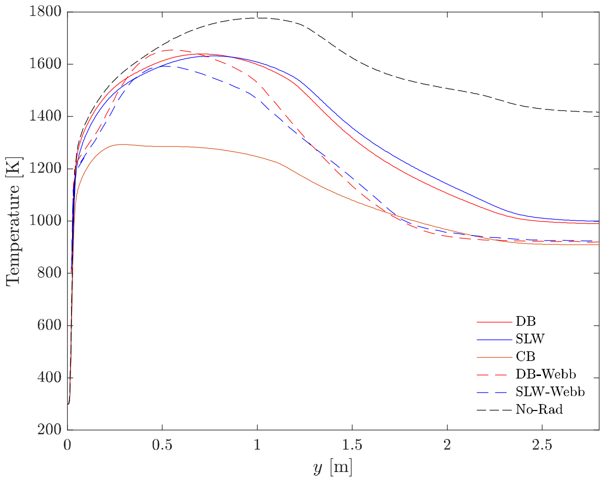

Figure 3.7: Temperature along the axis.

In Figure 3.8a, the gas temperature for PL1 is presented. Here, the experimental results from Andersson et al are included. As it can be observed, none of the models is able to capture the correct temperature profile as measured in the experiments. This probably stems from the fact that the eddy dissipation model was used and not a detailed chemistry model with a coumpled detailed chemistry mechanism. All models present a peak around $y = 0.05$ m, where the cylindrical region in which stoichiometric combustion is taking place is located. The DB and SLW models are again producing similar results, however the SLW model seems to better capture a more even heat distribution and thus, presents slightly lower temperatures. However, in the results Webb et al reports, the SLW model predicts even lower temperatures in the combustion region and higher in the bulk flow region. The CB model predicts much lower temperatures in the combustion region and higher temperatures in the mixing regions within the bulk flow from $y = 0.07$ m to $y = 0.2$ m. Here again, higher absorption coefficients tend to flatten the temperature gradients in the radial direction. The no radiation treatment shows higher temperatures in the combustion region, however the difference is not great. This is propably because the residence time in the peak temperature zone is low. This suggests that low absorption coefficients do not affect the near stoichiometric combustion process by a large margin. Unlike the combustion region however, the No-Rad case presents very high temperatures throughout the bulk flow region. This again suggests that, in general, a more detailed radiation treatment can plays an important role in heat distribution of the case.

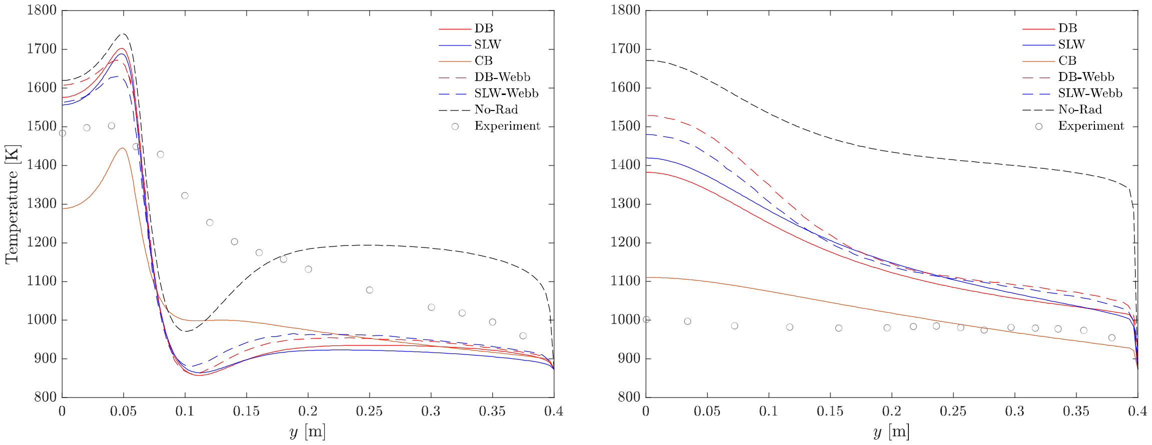

(a) $x = 348$ mm

(b) $x = 1400$ mm

Figure 3.8: Temperature profiles in the radial direction for the $x = 348$ mm and $x = 1400$ mm planes

In Figure 3.8b, the gas temperature for PL2 is presented. The DB and the SLW models present a maximum difference of approximately 45 K. The overall temperature differences between the SLW and the DB contours can be viewed in Figure 3.9c (SLW minus DB). As it can be seen in all the DB and SLW models, elevated temperatures are present starting from the axis and decrease radially. The data from Webb present higher temperatures for both models that decrease more steeply and reach the bulk flow temperature at $y = 0.07$ m. Another difference arises from the fact that the SLW-Webb predicts lower temperatures than the DB-Webb model. In contrast, in the present simulations the SLW model predicts higher temperatures than the DB model. This can be explained by the following reasoning.

In Figures 3.9a and 3.9b, where the predicted CO concentration by the SLW and DB WSGG models are illustrated, the two models present a difference in the CO concentration along the PL2. This can be interpreted as an extended flame structure to the x direction in the case of the SLW model. A possible explanation behind this observation, is the fact that this model accounts for the additional radiative heat transfer introduced by the CO earlier in the domain. As it can be observed in Figure 3.9c, earlier in the flow, there a significantly lower temperature predicted when the oxidant firstly meets the propane near the inlet. This is where near stoichiometric combustion is happening and a lot of CO is produced. Additionally, in the rest of the flame area the SLW predicts lower temperatures. This temperature descrease, is due to added radiative heat distribution by the CO. Thus, these lower temperatures can lead to less fuel being combusted and therefore, a longer flame structure.

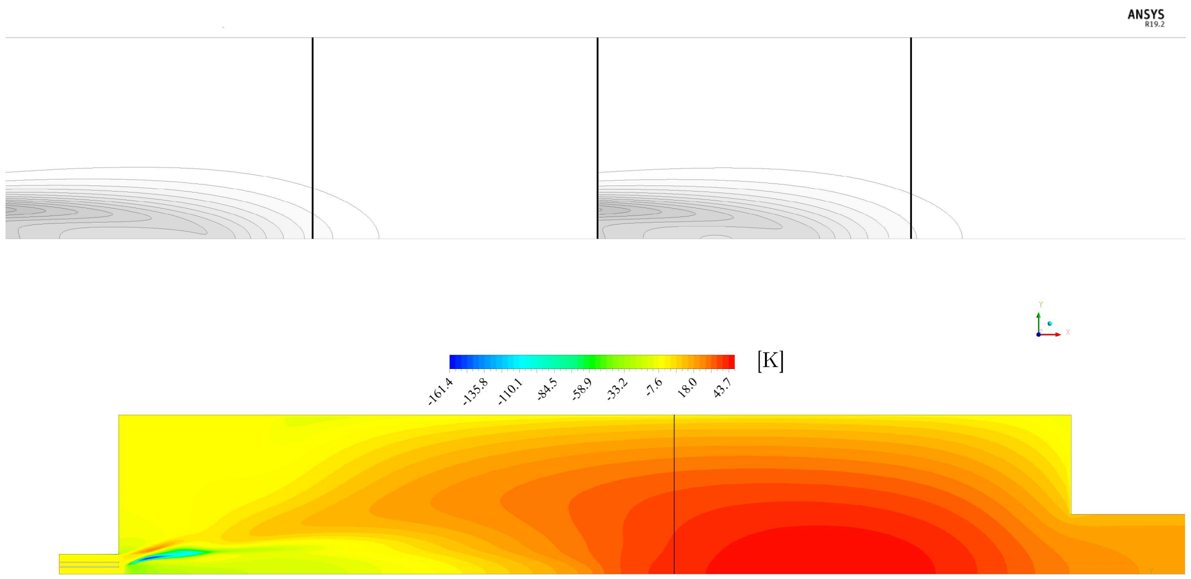
(a) SLW model

(b) Domain Based WSGG model

(c) Temperature Difference

Figure 3.9: Molefractions of the produced CO calculated by the (a) SLW and (b) DB model and their resulting temperature differences. (c) Temperature difference between the SLW and DB models (SLW minus DB).

Additionally, in 3.8b the CB model predicts a more uniform temperature profile, which is in fact close to the experimental results. In contrast, the No-Rad approach overpredicts the temperature by more than 400 K in the majority of PL2. This suggests that more detailed radiation treatment can directly impact the bulk flow temperature in this case.

3.3.2. Effects on species concentrations

Figures 3.10 and 3.11 present the radial profiles in PL1 and PL2 for the CO_2 and H_2O molefractions. As it is evident in both planes, there is little difference in all the models concerning the concentrations of either CO_2 or H_2O. This is especially pronounced by the fact that in both planes, even in the extreme scenario of not treating radiation at all, the resulting concentrations are the same throughout the radial direction.

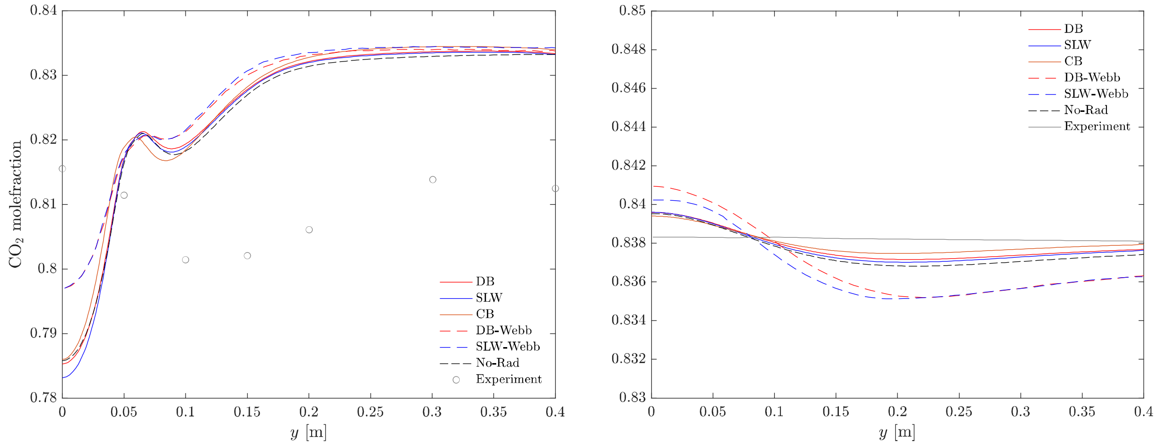

(a) $x = 348$ mm **(b)** $x = 1400$ mm

Figure 3.10: CO_2 profiles in the radial direction for the $x = 348$ mm and $x = 1400$ mm planes.

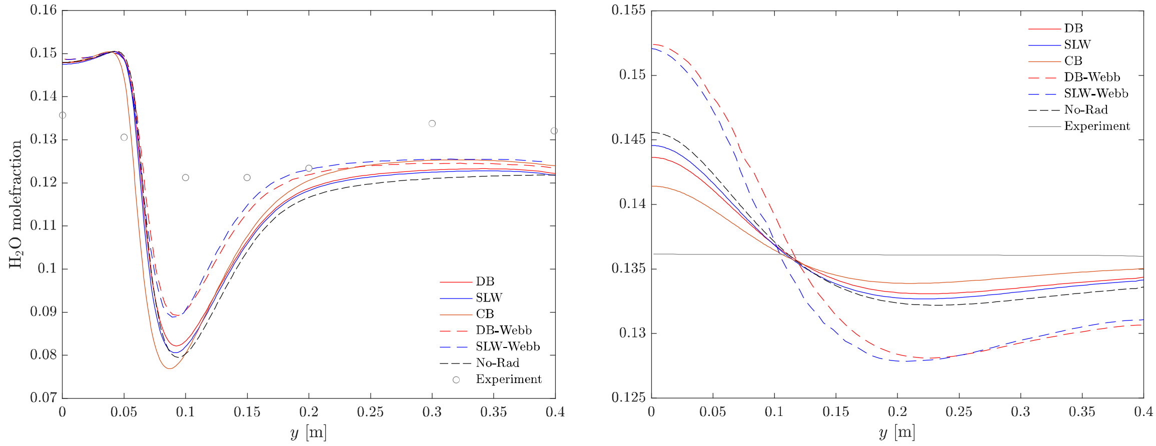

(a) $x = 348$mm **(b)** $x = 1400$mm

Figure 3.11: H_2O profiles in the radial direction for the $x = 348$ mm and $x = 1400$ mm planes.

In 3.10a the CO_2 molefraction presents a steep increase of 4% up to $y = 0.06$ m. This means that combustion is taking place in this region and this, in turn, results in the creation of new CO_2. The slight drop afterwards suggests further mixing with the oxidant. This coincides with the creation of H_2O in Figure 3.11a. In the same region there is a sharp drop, due to the introduction of the oxidant and the subsequent dilution of the H_2O stream. Again the difference from the experiments in both 3.10a and 3.11a is clearly evident, which suggests more detailed chemistry modeling is required. In the P2 plane there is a small overprediction and then an underprediction in both CO_2 and H_2O, however the differences between the different models are well within the margin of error.

In most of the cases extracted from Webb et al, overpredictions of the species concentrations (except the ones mentioned above) are observed compared to the results presented in this thesis. These discrepancies most likely stem from using slightly different inlet mass flows. This fact can also explain the difference in flame length mentioned in the previous section, since the introduction of less fuel can lead to lower temperatures overall [88].

Based on the results presented so far, as it can be seen in 3.9, modeling radiative gas properties can result in big temperature differences especially in the cylindrical region were near stoichiometric combustion takes place. Knowing that, it can be assumed that these differences can play a significant role when more complex detailed chemistry mechanisms are used, since the temperature profile can affect the creation of species significantly. Moreover, it should be noted that an advantage of the SLW model is that it also accounts for CO instead of only CO_2 and H_2O which is the case for the WSGG models. Thus, in cases that involve incomplete combustion or involvement of CO, the SLW model might provide better results than the WSGG model.

3.3.3. EFFECTS ON THE RADIATIVE HEATING SOURCE

Figure 3.12 illustrates the volumetric radiative heat source in the PL1 and P2 planes. The negative sign is explained by the fact that in this region combustion takes place and thus, the resulting radiation is emitted to the bulk flow. The positive sign after that, illustrates the radiation absorption by the oxidant. In Figure 3.12a the difference between the SLW and the DB models is pronounced around the $y = 0.06$ m where, as stated before, the stoichiometric combustion takes place as well as, around the mixing region around $y = 0.1$. In the rest of PL1 there is no difference between the predicted flux divergence using the DB and SLW models. In SLW-Webb, this difference in radiative heat source seems to persist towards the axis, where it is almost double the SLW value, whereas in the DB and DB-Webb it is the same. The CB model predicts a four times larger radiative heat source in the peak region. That again highlights the importance of rigorous treatment of the radiative transfer particularly around the flame region. Higher absorption coefficients calculated in the flame region directly impact the increase in bulk temperatures.

In Figure 3.12b there is no deviation between the DB and SLW model, whereas for the DB-Webb and SLW-Webb there is a difference of approximately 100 $\mathrm{kW/m^3}$. This again can be explained by the discrepancy in the flame length. It also show the sensitivity of the radiative heat flux on the temperature difference. In Figure 3.8b the temperature difference is 44 K and higher temperatures can lead to differences in the calculation of the absorption coefficient of the SLW model. This also highlights the dependence of the radiative heat flux on temperature. A change in temperature which is in the order of magnitude of 3% will influence the emitted energy by approximately 12%. The CB model predicts almost two times the higher values compared to the DB and the SLW models.

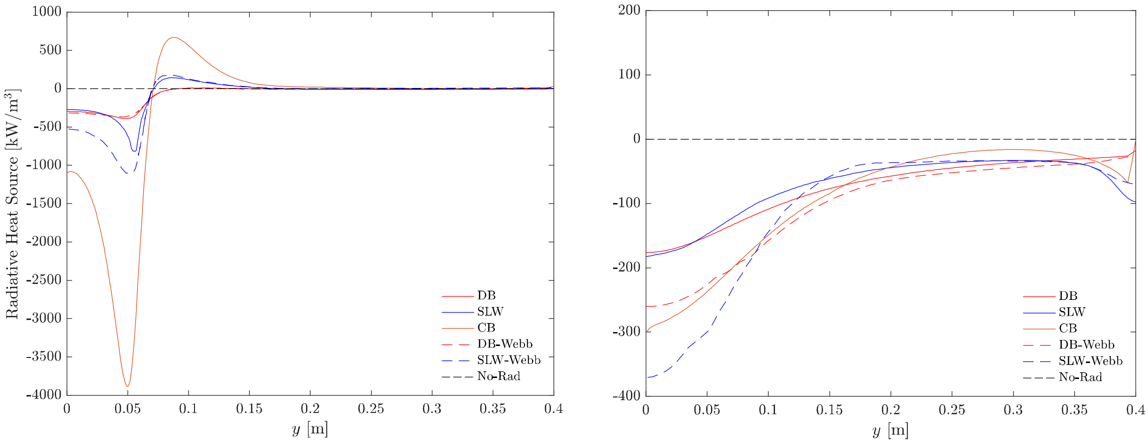

(a) $x = 348$mm **(b)** $x = 1400$mm

Figure 3.12: Radiative heat source profiles in the radial direction for the $x = 348$ mm and $x = 1400$ mm planes.

From this analysis it is evident that modeling the radiative heat transfer can play a pivotal role when simulating a furnace. First of all, it was shown that detailed radiative gas properties modeling plays a significant role in the distribution of heat in the bulk region of the computational domain. The simulation of the radiative gas properties is important and directly influences the resulting temperature field. Moreover, in section 3.3.1, it was observed that more accurate radiation treatment can alter the flame temperatures. This can possibly have an effect in more detailed chemistry mechanisms. While this furnace does not operate in MILD combustion conditions, detailed radiation treatment is suggested in MILD combustion, since calculating the recirculatory bulk flow temperature in this regime is very important. Additionally, better radiation treatment leads to more even heat distridution, which is a key aspect of MILD combustion in general.

4

FLAMELESS COMBUSTION FURNACE

As it was highlighted in section 1.1, MILD combustion has the potential to be applied in a wide variety of industries. However, a big hurdle in its practical implementation is the limited understanding of many of its fundamental aspects. To overcome this barrier, in recent years, extensive numerical and experimental work has been conducted in this field.

Much of the research on MILD combustion was centered around burners and the simulation of JHC flames [7], [89], [90]. Moreover, successful attempts have been made to combine oxyfuel combustion with MILD combustion [91], [92], [93], [94]. However, the observations of the researchers on these flames represents only a fraction of the multitude of phenomena that occur inside a furnace. The correlation among these types of flames and the flow inside a furnace is still unclear [95]. Compared to JHC burners, the internal recirculation patterns needed to sustain MILD combustion are more faithfully represented in enclosed furnaces. Moreover, the effects of radiative heat transfer between the flame and the walls are taken into account.

Many burners have been numerically modeled with multitudes of models. Notable examples are by Graça et al, who focused on the different chemistry models, including the EDC, and modeled the turbulent flow via the realizable $k-\varepsilon$ model [96], Rebola et al, who employed the standard $k-\varepsilon$ to assess the impact of EDM on MILD combustion [97], and Galleti et al who used the modified version of $k-\varepsilon$ with the EDM [98].

Throughout the years however, several researchers made comparisons between different numerical models, in order to simulate flameless combustion in furnaces. Li et al conducted a jet momentum and NOx study and employed the EDC model coupled with the GRI-Mech 3.0 mechanism [99]. Lupant et al used the standard version of the $k-\varepsilon$ and evaluated the differences between the EDC and EDM models [100]. A study by Fortunato et al introduced a new partial stirred reactor concept

(PaSR) and using the modified $k-\varepsilon$ model, compared it to the EDC coupled with the KEE58 and GRI 3.0 mechanisms [101]. More recent developments include a study by Chinnici et al, using the standard $k-\varepsilon$ and the standard EDC model with a skeletal mechanism [102], and also, a study by Ferrarotti et al which compares the PaSR with the EDC model coupled with 3 different chemistry mechanisms and the standard $k-\varepsilon$ and with the $k-\omega$ SST [103]. Finally, a very detailed study by was conducted Fortunato et al [75]. This study included five different turbulence models, i.e the standard, modified, renormalization group, realizable $k-\varepsilon$ and RSM models. Moreover, the EDC model was evaluated based on its coupling with the 4 different mechanisms, among them the GRI-Mech 3.0 and the KEE58 mechanism.

Generally, there is no clear consensus reached on which chemistry and turbulence models should be used in order to effectively simulate MILD combustion. Moreover, there is no research that includes detailed radiation analysis using advanced models.

Concerning the radiation modeling, Christo et al [104] on his work on unconfined JHC flames, concluded that the inclusion of thermal radiation in the models does not play a significant role in the simulation of MILD combustion. This claim was also supported by De et al [7] who worked on the Delft-Jet-in-Hot-Coflow flame. These suggestions made many researchers refrain from using advanced radiation models, due to the additional computational costs. However, in the work of Christo et al, it was also stated that radiation should be included for modeling MILD combustion in confined furnaces since radiative heat transfer between the flame and the walls can have a large effect on flow and flame characteristics. On the same note, Lewandowski et al [39] explains that in MILD combustion, due to the diluted conditions, radiative heat transfer can be significantly different from conventional combustion processes and therefore, proper radiation modeling is required.

Some studies with advanced radiation models such as the SLW, have been conducted targeting combustion systems, but most of them are using simple enclosures or targeting other types of furnaces [61], [67], [77], [105], [106]. Detailed radiation studies for MILD combustion have not been conducted so far, to the knowledge of the author.

For these reasons, the simulation of a flameless combustion furnace and the comparison of different radiation, turbulence and chemistry models is conducted in the context of this thesis. Huang et al [10] reported MILD combustion experimental results in a lab-scale furnace located in TU Delft, using natural gas as fuel. The objective of his work was to characterize flameless combustion in a labscale furnace that is simple enough to allow measurements while keeping most relevant characteristics that are found in large scale industrial furnaces. This furnace consists of an industrial burner and a thermally insulated combustion chamber. The inlet and exhaust are on same side. This type of furnace is also called reverse flow style burner. Due to the design of the burner, the fuel and the reactants are not premixed and enter the combustion chamber as jets. This configuration forces the incoming reactants to mix with exiting products and radicals prior to ignition and establish a low velocity region downstream. Therefore, stable flameless combustion with lower than autoignition inlet temperature is achieved.

4.1. DELFT LAB-SCALE FURNACE

The Delft lab-scale furnace is a cuboid furnace with internal dimensions of 320 mm x 320 mm X 630 mm. Figure 4.1 presents its detailed design. A commercial WS REKUMAT 150 recuperative Flame-FLOX burner is mounted at the bottom and is fired upwards. The burner has a total diameter of 92 mm and it protrudes 30 mm from the bottom of the combustion chamber, thus making the distance between the tip of the burner and the top wall 600 mm. It creates a central gas lance, from which fuel is introduced, surrounded symmetrically by four oxidizing agent feeds.The fuel and oxidizer feed nozzles have a diameter of 4.5 and 8.6 mm, respectively. The walls are created from 310 stainless steel and the bottom and side walls are insulated by ceramic foam layers with total thickness of 50 mm. The top walls are not insulated and act as heat sinks. Two of the sidewalls include quartz windows with sizes of 280 mm x 100 mm. These windows allow for optical access to obtain measurements. The side walls and windows can be moved along the z axis while the burner, internal top wall and optical setups are fixed. That allows for the measurements to be conducted in different planes along the z axis. The flue gas outlet is a 10 mm slit located between the sidewalls and the bottom wall.

The furnace can operate in both flame and flameless modes. The flame mode is used to preheat the furnace to 1123 K. Once the temperature inside the furnace surpasses that threshold, it switches to flameless mode automatically. In order to sustain flameless combustion, the inlet air is preheated in the built-in recuperator, where the resulting flue gases are utilized after they exit the combustion chamber.

4.2. CASE DESCRIPTION AND MODEL CONFIGURATION

4.2.1. CASE DESCRIPTION

Using this lab-scale furnace, MILD combustion experiments were conducted with natural gas as fuel. The composition of the natural gas is presented in Table 4.1. Three different sets of experiments are reported, with thermal input of 9 kW, at three values of equivalence ratio, namely $\varphi = 0.7, 0.8, 0.9$. For this study, the simulation of the case with equivalence ratio 0.8 was chosen, since previous studies were conducted using the same ratio [107], [45]. The thermal input power was constant in all the experiments thus, only the air flowrate was varied. The furnace's operating conditions during the case that is simulated as part of this thesis are presented in Table 4.2.

Table 4.1: Dutch natural gas composition

Species	CH_4	C_2H_6	N_2	Rest
[mole %]	81.3	3.7	14.4	0.6

The fuel and air enter the combustion chamber as jets, and combust further

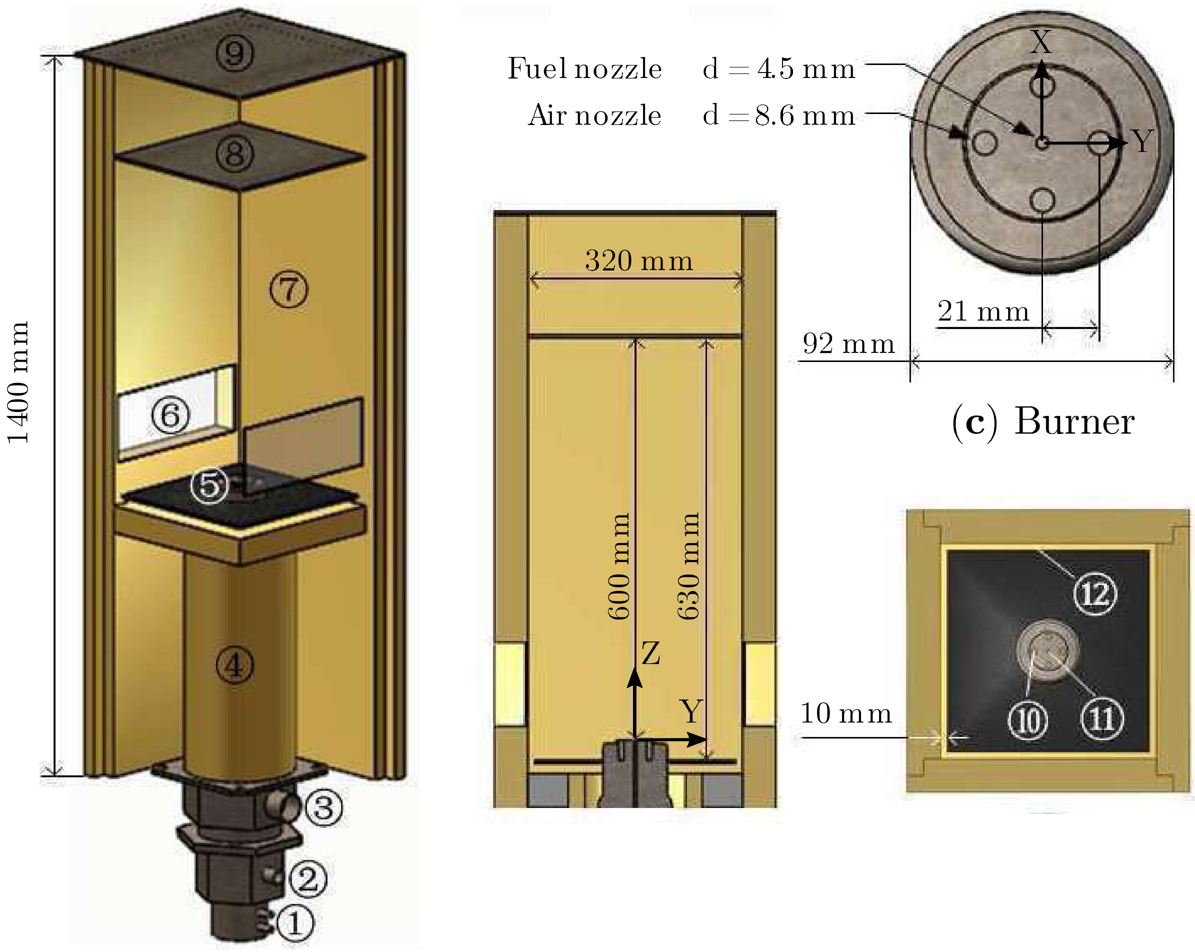

(**a**) front view (**b**) section view (**c**) Burner (**d**) top view

5. Burner nozzle
6. Quartz windows
7. Insulation walls
8. Internal top wall
1. Fuel inlets
2. Air inlet
3. Flue gas exit
4. Recuperator
9. External top wall
10. Air nozzles
11. Fuel nozzle
12. Outlet

Figure 4.1: (a) Schematic of the Delft lab-scale flameless furnace, (b) vertical cross section of the combustion chamber, (c) top view, (b) REKUMAT 150 nozzle [10].

downstream after sufficiently mixing. The flue gas inside the furnace recirculates internally and exits from the slit on the bottom. The burned gas on its way to the exit is entrained by the fast moving air jets, thus decreasing the overall oxygen concentration of the air jets. The momentum of the fuel jet is relatively high and therefore, the fuel-oxidant mixing is delayed. Consequently, the reactions take place further upstream and there is sufficient time for enough gas flue gas entrainment, which leads to flameless combustion. The regime was found to be sustained by autoignition.

During the experiments, temperature and velocity measurements were made. The velocity and temperature profiles were measured using Laser Doppler Anemometry (LDA) and Coherent Anti-stokes Raman Spectroscopy (CARS), respectively.

Table 4.2: Furnace operating settings. $\dot{V}_f$ and $\dot{V}_a$ are the fuel and air flowrates, respectively. T_f and T_a are the fuel and inlet temperatures, respectively.

P [kW]	φ	$\dot{V}_f$ [nl/min]	$\dot{V}_a$ [nl/min]	T_f [K]	T_a [K]
9	0.8	17.27	180.4	416	816

The reported accuracy for the LDA was 2-8% and for the CARS was 20 K. The measurements were conducted through the optically accessible windows that are fixed on the side walls. For each z plane measurement they were moved upwards and fixed in place until the measurements were completed. The gases flow rates were controlled by Bronkhorst mass flow controllers with an inaccuracy of ±0.5% on the reading plus ±0.1% on the full scale range. Lastly, three super OMEGACLAD$^{\mathrm{TM}}$ XL sheathed ungrounded type K thermocouples were used in order to measure the wall temperatures. The temperature drift of these thermocouples is less than 5 K. One was mounted on the internal top wall surface and two were mounted on one of the side walls. With this setup, when moving along the z axis different temperature measurements can be obtained at the corresponding locations of the axis.

4.2.2. MODEL CONFIGURATION

For the modeling of this case the commercial CFD code ANSYS Fluent 19.2 was used. Only half of the geometry of the furnace needs to be simulated since it is mirror-symmetric along the y-z axis. Using this, steady state RANS modeling studies were conducted in order to estimate the furnace temperatures and velocities. The same geometry was utilized in other studies that were performed in the same furnace by Bao et al [44] and Romero-Anton et al [45] and it presented in Figure 4.2.

The 3D computational domain extends 320 mm on the y axis, 160 in the x axis and 630 mm in the z axis. The burner protrudes from the furnace 30 mm and the start of the x-y-z axis is from the center of the circular fuel inlet. Out of the five total inlets, the halves of the two air inlets and the fuel inlet, as well as one whole air inlet is inside the computational domain. Furthermore, an inlet pipe of 90 mm in length was included to let the flow develop before it enters the furnace. In Figure 4.2 the outlet is denoted with red colour and black arrows represent the direction of the flow. The walls are denoted with gold colour and the quartz windows with light blue. The symmetry plane shows a temperature contour.

MESH

The simulations were conducted in the aforementioned geometry using an adequately fine mesh. Since in this case round geometries must be combined with a large cuboid, a non-uniform mesh must be constructed. The O-grid strategy was used in order to handle the circular nozzles and in the rest of the domain hexahedral cells were constructed using the multi-block approach. The structured grid around the inlet

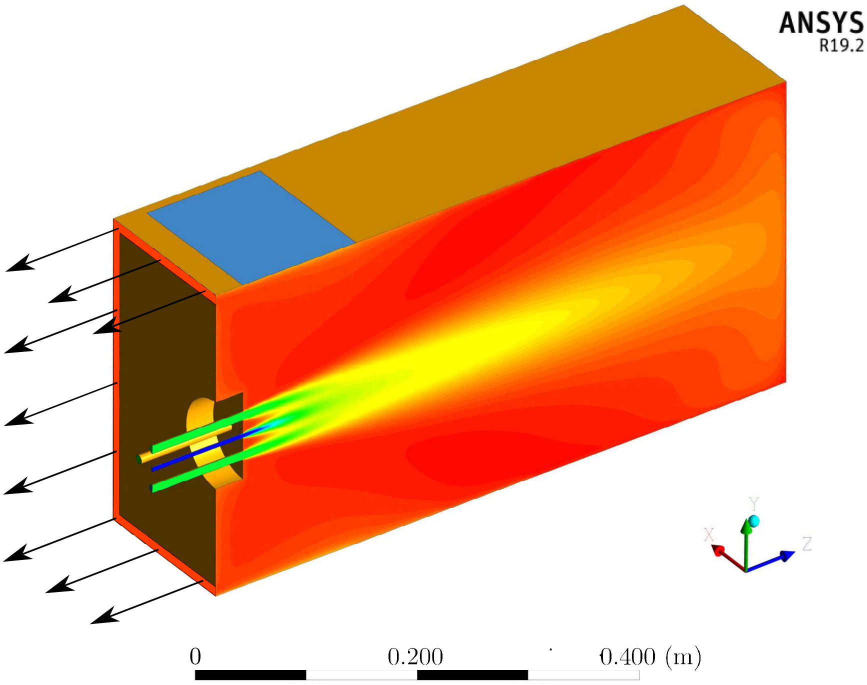

Figure 4.2: Geometry used to simulate the Delft Lab-scale furnace.

is presented in Figure 4.3b. In the zone where the jets were expected to merge, the grid was clustered in order to get more accurate results for the jet diffusion. Thus, in the end, 805014 cells were created in total. The full grid in the symmetry plane, along with the clustering in the mixing region can be seen in Figure 4.3a.

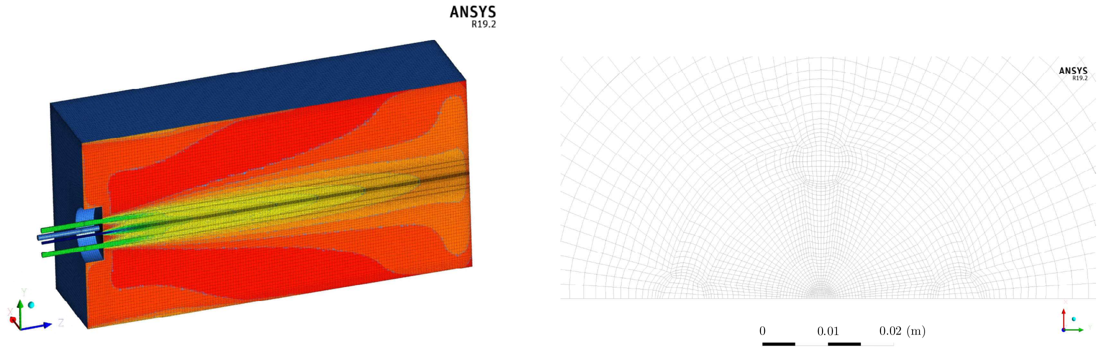

(a) Grid on the projected symmetry plane.

(b) Structured grid in the inlet.

Figure 4.3: Structured grid in the inlet.

Moreover, a grid independence study was conducted by Romero-Anton et al [45], in order to assess the importance of the grid discritization on the solution. This analysis, in which the same models were used for all the different grids, compared three different mesh sizes, a very fine mesh with 1.78 million elements, the aforementioned 800 thousand cell mesh and a coarse mesh of 350 thousand cells. Using a discretization error quantification method, the grid of 800 thousand cells was finally selected, since it met the criteria required by the method (Grid Convergence Index [108]).

BOUNDARY CONDITIONS

A very important aspect in any RANS simulation is the correct definition of the boundary conditions. The natural gas enters from the fuel inlet with mass flow of $\dot{m}_f = 2.37 \times 10^{-4}$ kg/s based on the experimental analysis. However, since only half of the domain is simulated only half of this amount is required. Thus, the inlet flowrate is set to $\dot{m}_f = 1.185 \times 10^{-4}$ kg/s. The inlet temperature is 446 K and the inlet species are specified as 85% CH_4 (the addition of methane and ethane) and 0.6% CO_2 (as the rest) and the remaining is automatically set to N_2. As for the turbulence specification method, the intensity and hydraulic diameter are used, with the fraction of intensity 0.1 and diameter 4.5 mm.

The total air mass flow is $\dot{m}_a = 3.87 \times 10^{-3}$ kg/s. However, it is distributed among 4 inlets thus for each air nozzle, $\dot{m}_{a,n} = 0.9675 \times 10^{-3}$kg/s. For the two halves of the fuel inlet, also half of the nozzle air mass flowrate is required, thus $\dot{m}_{a,\text{half}} = 0.48375 \times 10^{-3}$kg/s. The inlet temperature was also specified following the experiments and was 843 K. For the inlet species concentration 21% O_2 was specified, the remaining 78% is automatically set to N_2 and for the turbulence specification method, the intensity and hydraulic diameter are used again, with the fraction of intensity 0.1 and diameter 8.6 mm.

In order to properly simulate the combustion process, adequate care must be given to the temperatures along the wall. Since CARS calculations and thermocouples calculations are available, the temperature profile along the walls will be based on those data. Firstly, the thermocouples temperatures were collected from the work of Huang et [95]. There are two temperatures available for every thermocouple, thus two for the top wall and two for each position along the sidewalls. These temperatures are averaged for each plane and subsequently 7 temperatures along the wall and one top temperature are calculated. In order to find a good fit for the side wall temperature function a third order polynomial was used. However, these temperatures were found to be in some cases more than 200 K lower than the bulk CARS temperatures inside the furnace. Since the furnace is operating in MILD combustion, and one of its characteristics is a uniform temperature field all the temperatures were raised by 200 K, in order to match the measured ones using CARS at 40 mm away from the wall. The same process was conducted by Fortunato et al [75], in order to simulate a flameless combustion furnace. In the cases where the temperature was found to be higher on the wall than on the actual bulk of the flow, it was lowered to match the CARS measurement. This discrepancy between the CARS and thermocouple measurements is probably because of radiative heat transfer away from the wall and to the environment, as well as conductive heating to the ceramic foam layers. The resulting third order polynomial and the points it was based on can be seen in Figure 4.4. This polynomial was imported into ANSYS Fluent via a UDF. The top wall is assumed to have uniform temperature and is set at a constant temperature of 1314 K based on the same method used above.

The bottom wall is assumed to be adiabatic. All wall emissivities were assumed 0.8 based on the suggestion of Huang et al [95]. Nonetheless, the value of 0.3 was also tested in order to evaluate the sensitivity of the calculations on the emissivity and the difference was negligible. Finally, the shear condition in all walls was assumed no-slip.

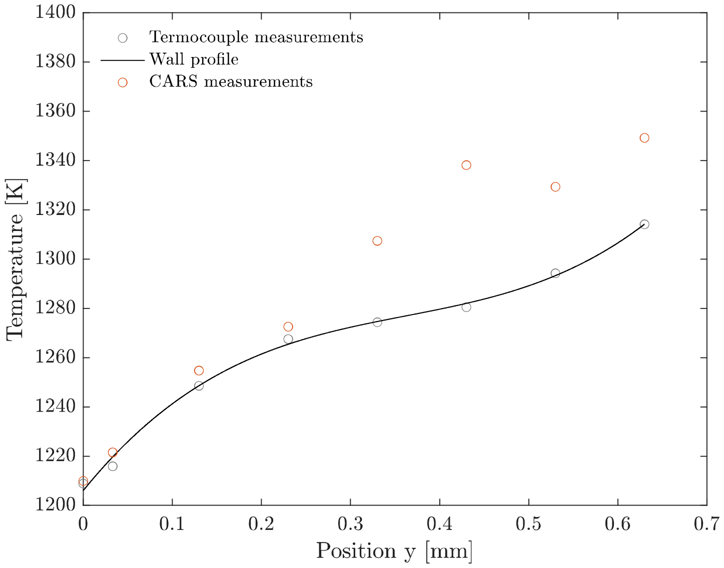

Figure 4.4: Resulting Wall temperature profile along the z axis for fixed x and y, based in CARS and thermocouple measurements.

MODELS

Since the main goal of this thesis is the comparison of different models and the assessment of their influence in MILD combustion, several turbulence chemistry and radiation models were used. A comprehensive table of the sets of models used in each case are presented in Appendix B. Here, a brief overview of these models will be provided, as well the justification behind their use.

The most integral part in any CFD simulation is the calculation of the flow field. Since in this case the flow is turbulent and moreover, there are jet streams present, several models, which are usually used in such types of flow were investigated. These models were briefly presented in Section 2.4. They are namely, the Standard $k-\varepsilon$ Model, the Modified Standard $k-\varepsilon$ Model, the Realizable $k-\varepsilon$ Model and the $k-\omega$ SST Model. While the standard $k-\varepsilon$ model is known to be not accurate in round jet turbulent flows, it will be examined, as its implementation is quite simple and the comparison with the others could be possibly quite insightful. In conjunction with the aforementioned models, standard wall functions were employed to treat the flow near the walls.

Another very important part of turbulent reacting flows is adequate chemistry modeling. Moreover, since MILD combustion will be modeled, which is more complex than ordinary flames, more care must be given in terms of chemistry modeling. For the cases that will be simulated in this thesis the EDC model was used to model the turbulence chemistry interaction. The EDC is the preferable choice in this case since it is able to account for the finite-rate effects and thus, it can incorporate detailed kinetic schemes. In this particular furnace design, the use of the EDC model was investigated in the past by Romero-Anton et al[45] and good results were presented albeit with modified volume fraction constants. The effect of the change of the volume fraction constant will be discussed in section 4.3.2 Moreover, several chemistry mechanisms for CH_4 combustion were used in order to explore their effects in MILD combustion. The investigated mechanisms are the the GRI-Mech 1.2, the GRI-Mech 3.0, the DRM-19, the KEE58 mechanism, a 30 species mechanism developed by Lu et al [60] (Lu-30) and automatic 27 species mechanism developed by Chen et al [59]. Lastly, a GRI-Mech 3.0 scheme without the NOx reactions, that are normally included in the original formulation, was used with 36 species and 217 chemical reactions. The use of these models will assess whether detailed, reduced or automatic mechanisms are preferred to model this kind of combustion process. The gases that participate in all these reactions were assumed incompressible ideal gases based on the suggestions of the ANSYS Fluent operating manual, since the Mach number was always lower than 0.1. All their properties were obtained based on ideal gas mixing laws.

The solution of radiative heat transfer equation was calculated using the discrete ordinates method. Based on the ANSYS Fluent manual [21], for optically thin problems, only the P-1, the DTRM and the DO models are appropriate and will produce correct solutions. However, only the DO model allows the computation of non-gray radiation using a gray band model. Thus, since such models were included for the calculation of the radiative gas properties, the discrete ordinates method was ultimately used. In order to model the angular discretization needed for the DO method, four θ and φ divisions and three θ and φ pixels were specified. For every RTE iteration, 10 energy equation iterations are performed, in order to speed up the convergence. The radiative gas properties modeling, was conducted using the standard domain-based WSGG, a 4-RTE domain-based WSGG (4 grey gases), a 5-RTE (5 grey gases) SLW model with tabulated ALBDF data and a cell-based WSGG, in which the gas layer thickness is provided by the average length of the cells. Also, it must be mentioned that the influence of turbulence radiation interaction TRI is not included in this study.

Lastly, it is also important to mention the discretization schemes that were used for the solution of the case. The pressure-velocity coupling was computed using the SIMPLE algorithm. The spacial discretization for the gradient was evaluated with the least squares cell based method. For the spacial discretization of the pressure, density, momentum, swirl velocity, turbulent kinetic energy, turbulent dissipation rate, energy, discrete ordinates and species, the second order upwind scheme was used. The simulations were conducted in the Reynolds cluster in TU Delft and each one was iterated until the residuals for all resolved quantities became constant over a couple of thousand iterations. In all cases the residuals of all the variables decreased for up to five orders of magnitude. The convergence was also monitored by inspecting three report plots. These plots calculated for every iteration the minimum and maximum temperature in the outlet and the area weighted average of the temperature along the centerline. When these plots as well as the residuals were constant for the aforementioned iterations the case was considered converged.

4.3. RESULTS AND DISCUSSION

In the following sections, the influence of the different models will be presented and compared. The available LDA and CARS measurements that are available for the Delft lab-scale furnace will be used as benchmarks for these comparisons. In each section, relevant contours will be presented in order to qualitatively assess the different models and subsequently, relevant plots will be provided to assess them quantitatively. In the contours that will be presented, the domain from $z = 0.03$ m to $z = 0.63$ m, will be shown, thus from the tip of the burner to the top wall. In the graph figures that will be presented another convention is used, with z the distance of the plane from the tip of the burner in mm.

Usually, in order to identify the reaction zones in reactive flows, either by imaging or in simulations, radical species are used. Since these species are mainly produced in the reaction zones and have very fast reaction rates they can be indicators of where the reaction zone is located [109]. The most commonly used radical is the hydroxyl radical (OH), since it is an intermediate species for all types of flames that leads to the creation of water. However, several studies have underlined the importance of formaldehyde (CH_2O) as a precursor species in MILD combustion [110]. These studies highlight that formaldehyde is an important pathline species in MILD combustion, relevant for the occurrence of auto ignition and can be used regardless of flame chemistry and liftoff height [110], [111], [112]. For this reason, both species will be used to represent the location of the reaction zones, denoted as "Formylradicals". The mass fraction of CH_2O indicates when the reactions start and the OH indicates that high temperatures have been reached. The formylradicals are calculated by the product of the concentrations of CH_2O and OH as suggested by Medwell et al [111].

Additionally, concerning the experimental results another parameter must be mentioned. Due to the symmetrical design of the furnace, mirror symmetry was expected. However, the experimental results are not completely symmetric and are slightly tilted to the positive y direction. This was explained by asymmetry in the fuel and air supply system that is upstream of the furnace. Since this discrepancy cannot be quantified and modeled, and in order to get an adequate comparison between the experimental and modeled profiles, the experimental profiles were moved in the negative y direction by a distance of $z \times \tan(\theta)$. The value of the angle θ is determined by the position where the shear stress value is equal to zero and in this case $\tan(\theta) \approx 0.03$. This change was conducted based on the suggestion of the publisher of the experiments, Huang et al [95] and has also been used by Romero-Anton et al [45].

4.3.1. INFLUENCE OF TURBULENCE MODELING

Since the scope of this section is the comparison between different turbulence models, the chemistry and radiation models must remain constant for all the cases. For this reason, the standard EDC model in conjunction with the GRI-Mech 3.0 mechanism was used, for the chemistry modeling. The GRI-Mech 3.0 was selected out of the various other mechanisms, since it is the most modern of the detailed mechanisms that where investigated. Though the use of this mechanism will be more computationally expensive, since it is more complex, it is expected that it will be more accurate than skeletal or older mechanisms. For the radiation modeling, the standard WSGG formulation provided by Fluent was used.

In Figure 4.5 the velocity and formylradicals contours for the turbulence models are presented. In all velocity contours there is a high velocity magnitude area starting from the inlet that diffuses downstream. The recirculation of the gases is also visible after the stream splits when it encounters the top wall. All the formylradicals contours exhibit reaction zones that become greater closer to the top wall. This can be explained by the fact that more mixing has taken place further downstream and therefore more reactions are occurring.

Out of the four models, the standard $k-\varepsilon$ seems to calculate the lowest velocities downstream of the burner. This is in agreement with the known overprediction of the spreading rate that this model presents. Moreover, the momentum diffusion is larger between $z = 0.2$ m to $z = 0.5$ m. In terms of the formylradicals the standard $k-\varepsilon$ seems to predict a very wide reaction zone that exists in the majority of the simulated domain. This can be explained by the increased diffusion mentioned earlier. Increased gas mixing leads to more reactions happening. The modified $k-\varepsilon$ seems to calculate the highest velocities overall. This effect is translated to less mixing downstream and therefore a smaller reaction zone, which is evident when looking at the formylradicals contour. The realizable $k-\varepsilon$ also appears to calculate high velocities, albeit lower than the modified $k-\varepsilon$. This is also translated to a smaller reaction zone. However, while the shape of the zone is similar to the modified $k-\varepsilon$ the number of the occurring reactions is greater. Therefore, also in this case the direct connection between mixing and number of reactions is established. Lastly, the $k-\omega$ SST seems to calculate slightly larger velocities than the standard model. It also presents a rather big reaction zone. Compared to the standard $k-\varepsilon$, the reaction zone is narrower and starts earlier. Additionally, in this model the flow seems to split earlier. In conclusion, it seems that there is a significant correlation between the turbulence models and the location and intensity of the reaction zones in the domain. This can be translated as direct result of the turbulence combustion interaction.

In order to choose the most appropriate turbulence model for this case, comparisons between the experiments and the calculated velocities must be made. As described before, The LDA measurements for the velocity were taken in 7 different planes along the z axis. There are mean axial velocity measurements for 3 mm, 50 mm, 100 mm, 200 mm, 300 mm, 400 mm and 500 mm away from the burner. The first profiles that are close to the burner and are mainly dominated by the

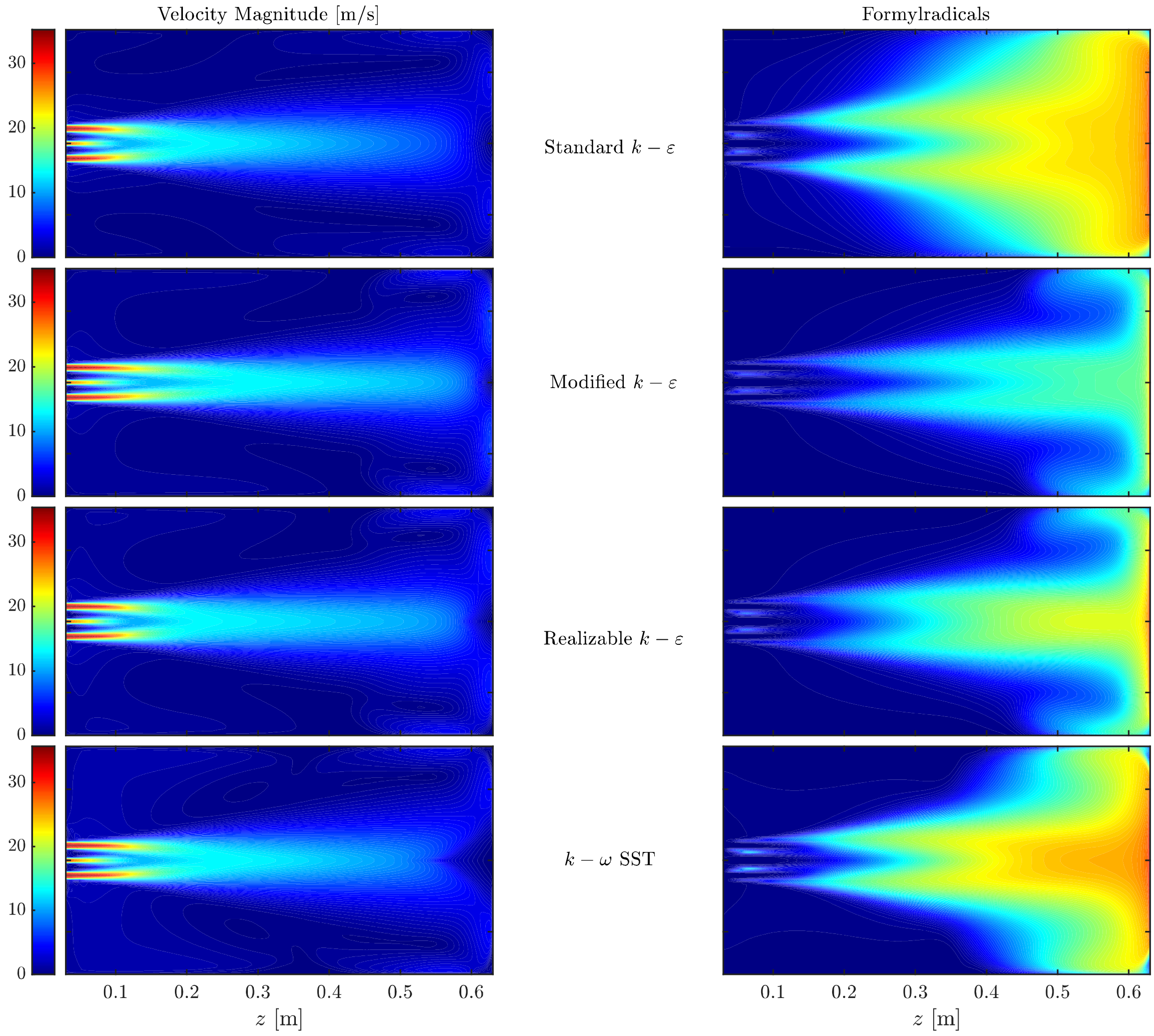

Figure 4.5: Velocity and formylradical contours for the different turbulence models.

jet flowrate. Therefore, the differences between the models are expected to appear further downstream in the domain.

In Figure 4.6, the profiles of the mean axial velocity that were extracted from the models, as well as the experimental results are presented. At the first location, which is very close to the the burner, all turbulence models predict the same profile. This is expected, since near the inlet the structure of the jet dominates the flow field. However, all models underpredict the maximum velocity in all the jets. In the second position ($z = 50$ mm), which can be also considered close to the burner, all the models accurately predict the velocity profile. In Figure 4.6b, it is evident that the velocity profile tends to tilt to the right (the velocity at the left air inlet is larger than the velocity at the right inlet). This not symmetric behaviour was discussed in section 4.2.1. Another takeaway from this plot is that the jet streams are starting to merge. In the position $z = 100$ mm the fuel streams have merged with the air streams except in the case of the modified $k-\varepsilon$ and $k-\omega$ SST. Here, only the realizable model manages to accurately capture the entirety of the velocity profile. The $k-\omega$ SST and the modified $k-\varepsilon$ overpredict the velocity at its peak, while the standard $k-\varepsilon$ underpredicts it. In Figure 4.6d the experimental inlet streams appear to have been fully merged. In the case of the $k-\omega$ SST and the modified $k-\varepsilon$ this has not happened yet. The standard $k-\varepsilon$ slightly underpredicts the peak velocity.

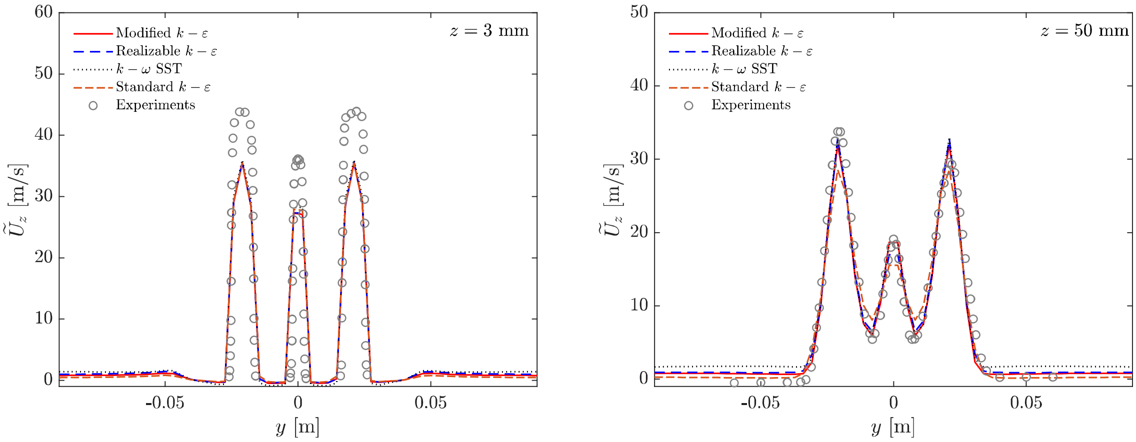

(a) $z = 3$ mm

(b) $z = 50$ mm

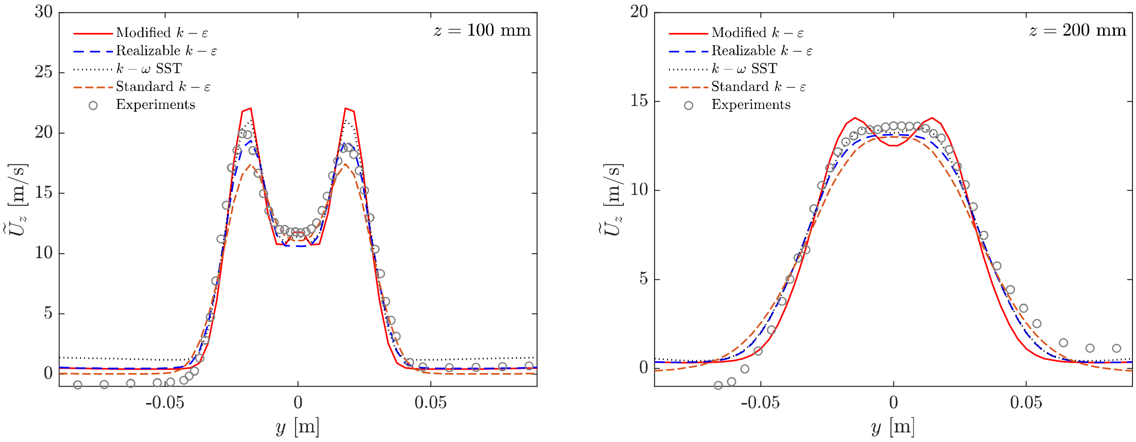

(c) $z = 100$ mm

(d) $z = 200$ mm

Figure 4.6: Mean axial velocity profile comparison of different turbulence models for $z = 3, 50, 100, 200$ mm.

In Figure 4.7a, only the standard model slightly underpredicts the measured peak velocity. All other models seem to accurately predict it. Additionally, all the jet streams in all cases have merged. It seems that halfway through the domain of the furnace all models manage to capture more or less the velocity profile with slight variations. In the position $z = 400$ mm, and for the first time pronounced differences in the calculated profiles are apparent. It seems that both the modified and realizable $k-\varepsilon$ models overpredict the peak velocity. Consequently, this substantiates the assessment from the contours that these two models predict higher velocities further downstream of the domain. The standard model seems to slightly underpredict the peak velocity, while the $k-\omega$ SST slightly overpredicts it. All models except the modified $k-\varepsilon$ seems to also accurately predict the velocity of the bulk flow.

In Figure 4.7c, the final velocity profile measurements are presented. As it can be observed, the modified and the realizable models $k-\varepsilon$ overpredict the velocity by a large margin. At this point it is apparent that the modified $k-\varepsilon$ cannot capture the flow inside the domain adequately. So far it has failed to capture the merging of the jet streams and consistently overpredicts the peak velocity. Thus, it is considered unsuitable for use in this case. Moreover, the realizable $k-\varepsilon$ seems unable to capture the velocity profile as well. While up to this point it presents adequate results, it fails to handle the diffusion of the jets in this location, thus producing higher velocities. The standard model and the $k-\omega$ SST both predict the bulk flow adequately. However, the standard model underpredicts the peak velocity and the $k-\omega$ SST overpredicts it, while both manage to capture the bulk flow velocity correctly. So far, both of these models seem to capture the profile adequately for the entirety of the domain. Thus, in order to choose which model is better for this MILD combustion furnace, another parameter must be investigated.

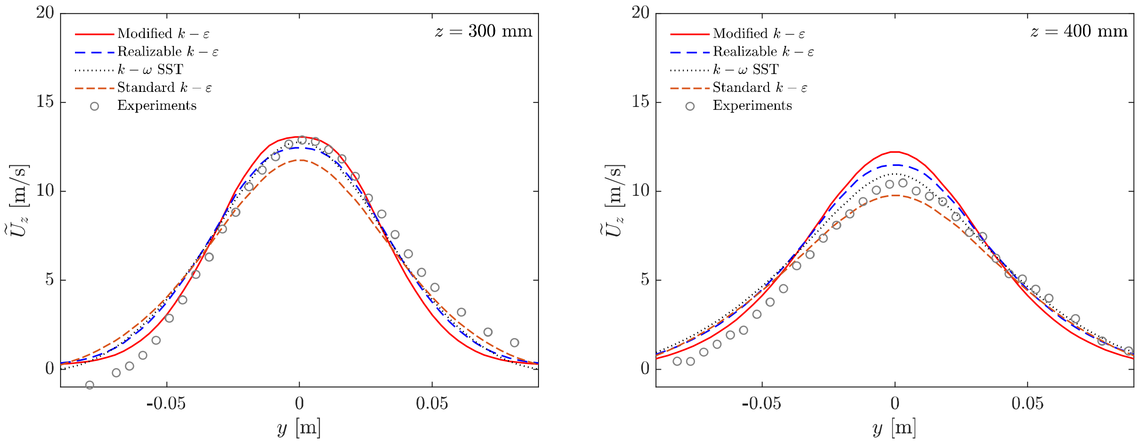

(a) $z = 300$ mm

(b) $z = 400$ mm

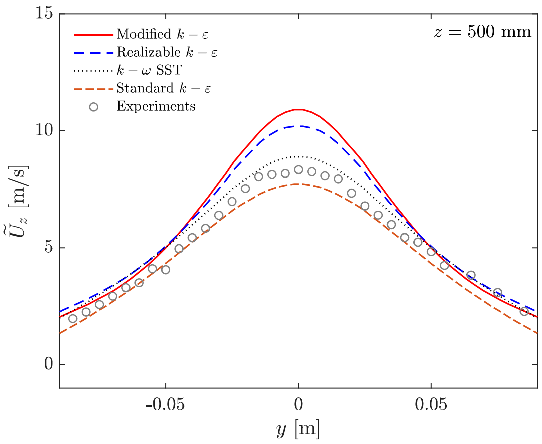

(c) $z = 500$ mm

Figure 4.7: Mean axial velocity profile comparison of different turbulence models for $z = 300, 400, 500$ mm.

It is already established that turbulence directly influences the resulting species by influencing the reactions. As it is evident from Figure 4.5, the majority of the reactions are taking part after $z = 500$ mm in all cases. Therefore, to finally conclude on which turbulence model is better for this case, a temperature contour for $z = 500$ mm will be presented. The temperature contour is used as a means to illustrate the results of the heat release due to the chemical reactions since there are temperature measurements for this location.

In Figure 4.8 it is evident that all models fail to predict the correct temperature. A different chemistry or radiation treatment might remedy this. However, only the profile that is calculated by the $k-\varepsilon$ manages to capture the shape of the experimental profile correctly. On the study by Ferranotti et al [103], also in MILD combustion furnaces, the $k-\omega$ SST and the standard $k-\varepsilon$ also produce comparable results. The researchers concluded to use the standard $k-\varepsilon$ as a basis for their other models. Fortunato et al [75], on her work on a semi-industrial flameless furnace concluded that the standard $k-\varepsilon$ is the best fit. Finally, Lewandowski et al [39], in his elaborate work in the DJHC flame also concluded on the use of the standard $k-\varepsilon$ for his simulations. Since in this case, the choice is between $k-\omega$ SST and the standard $k-\varepsilon$, the standard $k-\varepsilon$ will be used as the basis of the flow field modeling in the next sections.

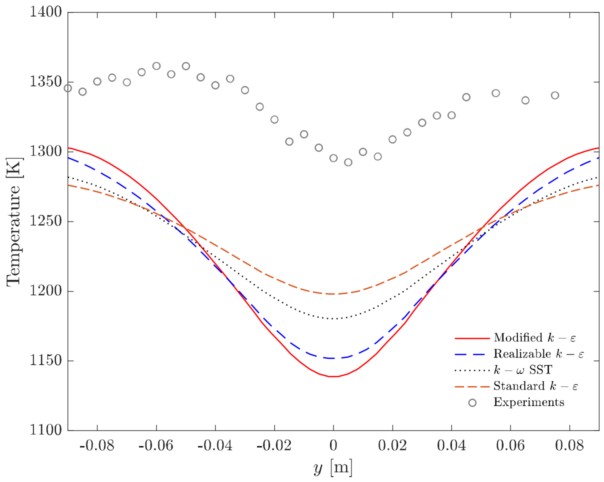

Figure 4.8: Temperature profile at $z = 500$ mm.

4.3.2. INFLUENCE OF CHEMISTRY MODELING

The investigation of the influence of the chemistry modeling in the Delft lab-scale furnace, will be described in two parts. Firstly, the effect of changing the model constants of the EDC model will be discussed. Several researchers have tried to tune the model constants of the EDC model in order to achieve good results for MILD combustion. Rehm et al [113] was one of the first researchers who evaluated both values for the model by trying to increase them. De et al [37], suggested increasing the time scale constant (C_τ) to 3 or set the volume fraction constant (C_ξ) to 1 for the simulation of the Delft-Jet-in-Hot-Coflow flame. Aminian et al [114] tried to increase the values of C_τ to 1.5 instead, while keeping the C_ξ close to the original value. Graça et al [96] and Evans et al [115] investigated the effects of changes in C_ξ and the constant $C_{\varepsilon 2}$ of the $k-\varepsilon$ model. Another recent approach on the modification of the EDC model was proposed by Parente et al [43]. This model, named the Extended EDC approach aims to correlate the model constants with the local turbulent Reynolds number and the local Damköhler number. The extended EDC model is further investigated by Evans et al [116], where new proportionality constants are introduced. A new extension to the EDC model is also presented by Bao et al [44] and Romero-Anton et al [45]. This approach again aims to correlate the model constants with the local turbulent Reynolds number and the local Damköhler number, however using a different approach based on different lengthscales. Therefore, it is evident no conclusive results on which constants are optimal has been produced so far. Additionally, the effect of the change of EDC model constants while coupled with different chemistry mechanisms has not been investigated so far.

In order to proceed with the investigation the turbulence and radiation models must remain constant for all cases. Based on the results of the previous section, the standard $k-\varepsilon$ model will be used as a turbulence model. For the gas radiative properties modeling the standard WSGG will be used.

THE EFFECT OF THE VOLUME FRACTION CONSTANT

In this section the contours of the temperature and the formylradicals for some of the chemistry mechanisms will be presented and discussed. For each case, the volume fraction constant of the EDC model was varied. The normal value of the C_ξ is 2.1377. Therefore, to check the effect of the model constant an arbitrary lower value of 2 and an arbitrary value of 3 were selected.

In Figure 4.9, the resulting contours for the KEE58 mechanism are presented. In this case, changing the volume fraction constant seems to have a very big impact on the temperature domain. Lowering the value of C_ξ to 2, results in differences toward the end of the domain, where the temperature is lower than the temperature at the case of with the normal constant. However, when C_ξ is 3, the temperature increase towards the end of the domain is significant. For $z = 0.55$ m for example, the temperature here is several hundred degrees higher than with the normal constant.

Changing the volume fraction constant also appears to significantly impact the location of the reaction zones. For the first case the reaction zone is practically fragmented into two reaction zones that attach to the top wall. For the normal value of the volume fraction constant, the reaction zone is moved upstream. Finally, for $C_\xi = 3$ the reaction zone has again moved upstream. Therefore, it can be concluded one of the effects of changing the value of C_ξ on the KEE58 model is that as the constant is increasing, the reaction zone tends to move upstream. Moreover, it must be noted that the reaction zone in this model closely resembles a flamefront. However, in a MILD combustion application a flamefront should not exist. In such applications autoignition causes the reactants to chemically interact and therefore reactions should appear all over the domain in RANS modeling.

In Figure 4.10, the resulting contours for the skeletal mechanism DRM-19 are

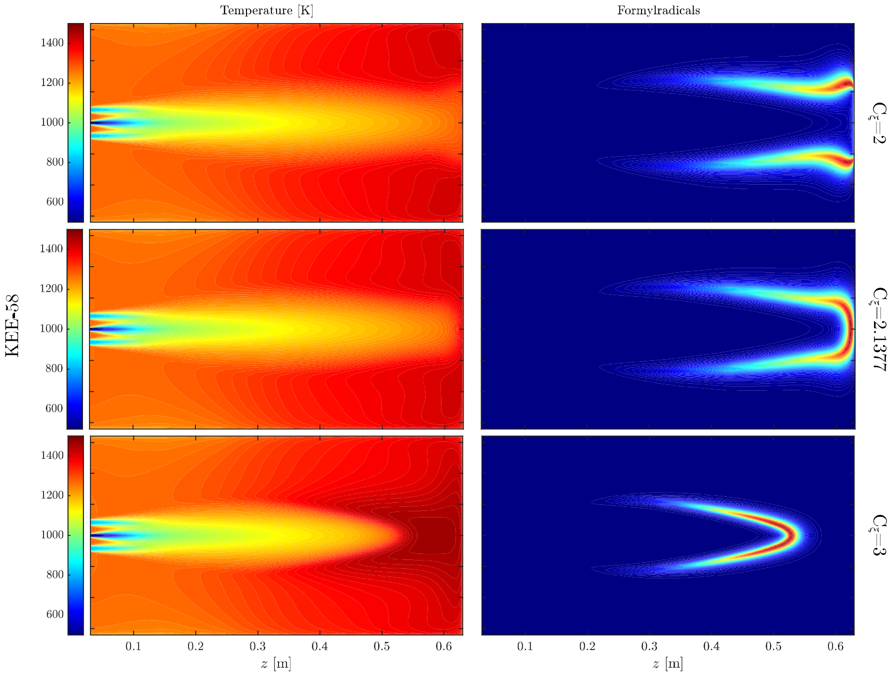

Figure 4.9: Temperature and Formylradicals Contours using the KEE58 mechanism for C_ξ = 2, 2.1377, 3.

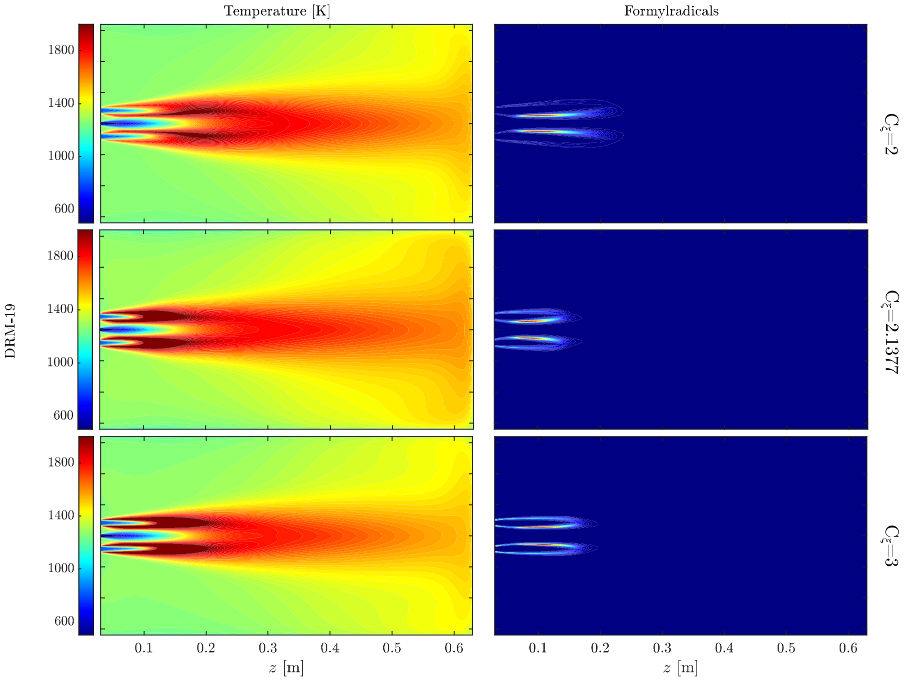

Figure 4.10: Temperature and Formylradicals Contours using the DRM-19 mechanism for C_ξ =2, 2.1377, 3.

presented. In all the presented cases the resulting peak temperature is extremely high. Particularly, for the case $C_\xi = 3$ the peak temperature is exceeding 2200 K. Moreover, in all cases the flame is local and very close to the burner. Such flame behaviour is not conforming with MILD combustion. Therefore, the DRM-19 model is not suitable for the MILD combustion modeling of this furnace.

In Figure 4.11 the effects of changing the EDC model constant on the detailed GRI-Mech 3.0 chemistry mechanism are illustrated. From the temperature contours it can be observed that the changes in the volume fraction constant do not affect the temperature field. The temperature in all cases is lower in the jet mixing region and only after the combustion of the gases it increases.

Despite not affecting the temperature in this mechanism, the change of the C_ξ directly impacts the location of the reaction zone. The GRI-Mech 3.0 presents a large reaction zone that takes up the majority of the domain. This is visible for all the formylradicals contours. In the $C_\xi = 2$ case it can be observed that some of the reactions are happening later in the flow. Therefore, more reactions are happening near the wall and after the flow is split. By increasing the value to $C_\xi = 3$, the reaction zone is displaced upstream. The majority of the reactions is concentrated near the centerline, while the reaction zone is narrower.

While there is no great visible temperature difference in the domain, there is a large displacement of the reaction zone in all cases. That means that the chemical reactions that are taking place during combustion are happening in different places in the domain and thus, in different temperatures. This in turn, could affect the estimation of the NOx production, which is the end goal in any MILD combustion simulation. Therefore proceeding with changing the EDC model constants should be done with care, since the chemistry profile is highly sensitive to these changes.

Lastly, in Figure 4.12 the effects of the automatically reduced chemistry mechanism from Chen et al [59] are illustrated. In this case both the temperature as well as the formylradicals domains are affected by the change of the constant. Lowering of the value of C_ξ to 2, results in differences between $z = 0.45$ m and $z = 0.55$ m. The low value case presents significantly lower temperature in this region, compared to the normal value case. When the volume fraction constant is increased, there is also a significant increase in temperature downstream and the low temperature mixing region is moved upstream.

Furthermore, the formylradicals location zone seems to also get impacted by the changes in C_ξ. The increase in the volume fraction constant directly influences the reaction zone, which is moving upstream. In addition to that, as the value increases, the reaction zone is getting thinner. It must be noted again that the reaction zone here, as in the case of the KEE58 mechanism closely resembles a flamefront. It is probable that both of these models missed an important combustion path that is prevalent in MILD combustion while they were reduced. However, while the investigation of what this path is, is an interesting topic, it is not part of the scope of this thesis.

In conclusion, it seems that the EDC predictions by different mechanisms are extremely sensitive to the value of the C_ξ. In all cases there is a shift in the reaction zone upstream and in the majority of the cases there is an increase in temperature.

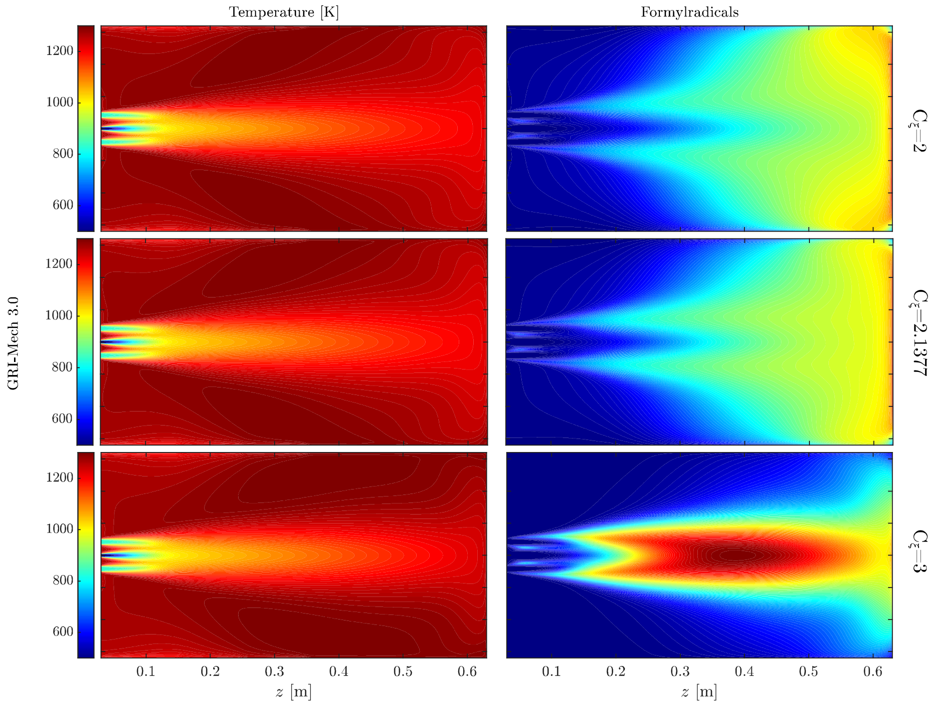

Figure 4.11: Temperature and Formylradicals Contours using the GRI-Mech 3.0 mechanism for $C_\xi = 2, 2.1377, 3$.

The DRM-19 mechanism seems unsuitable for the simulation of MILD combustion in this furnace. The rest of the mechanisms must be further evaluated in order to select the most suitable for further investigations.

THE EFFECT OF THE CHEMISTRY MECHANISM

In order to choose the most appropriate chemistry mechanism for the modeling of the labscale furnace, the temperature profiles that they predict must be compared with the experimental data that were measured. There are 7 temperature data sets available along the z axis obtained by CARS measurements. However, only the profiles at 100 mm, 200 mm, 300 mm, 400 mm and 500 mm away from the burner will be presented for brevity, since differences between the models are expected further downstream. In this section the KEE58, the GRI-Mech 3.0, the Chen and the Lu-30 mechanisms will be compared. Here the standard $k-\varepsilon$, the WSGG and the EDC with the default constants is used for all models.

In Figure 4.13a the mean temperature profiles for $z =$ 100 m are presented. It is immediately noticeable that the mechanism created by Lu et al [60] highly overpredicts the temperature in the furnace. That is also noticeable in Figure 4.13b. Here it must be noted that this exact behaviour was seen in the DRM-19 model, however it will not be presented for brevity. Therefore, the Lu-30 skeletal mechanism is also not suitable for the simulation of this furnace. All the other models appear to capture the the bulk flow adequately. The KEE58 and the Chen mechanisms underpredict the temperature along the centerline, while the GRI-Mech 3.0 also

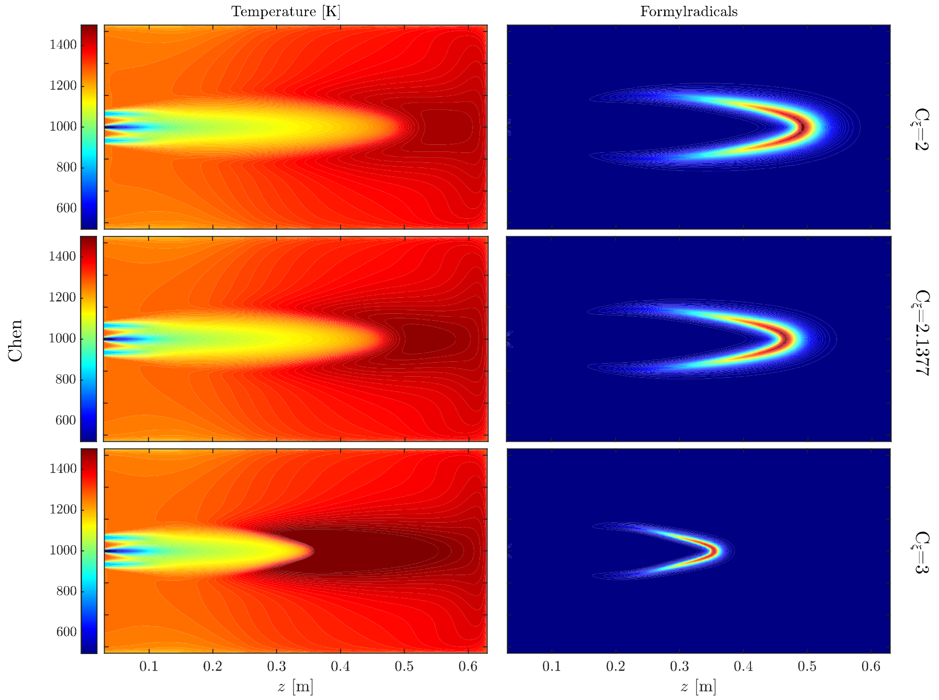

Figure 4.12: Temperature and Formylradicals Contours using the Chen mechanism for $C_\xi = 2$, 2.1377, 3.

underpredicts the temperature for $y = 0.05$ to approximately 0.02 m.

In Figure 4.13b, all the models again manage to predict the temperature of the bulk flow. However, all of them underpredict the centerline temperature. Additionally the Chen mechanism overpredicts the temperature for $y =$ -0.06 to approximately -0.04 m and on the other side for 0.04 to approximately 0.06 m, which coincides with the mixing region. It seems that for this model the gases have started to combust earlier. The Lu-30 mechanism will be omitted from next plots since it found unsuitable.

The next set of Figures (4.14) represents the temperature profiles downstream and specifically at the locations z =300, 400 and 500 mm away from the burner. According to Huang et al [107], in this region autoignition is more frequent and, therefore, the differences between the models are expected to be more pronounced.

In Figure 4.14a the experimental temperature profile is tilted to the right. This as mentioned before is due to the different velocities of the inlet air flow. On the left side the jet is slower, so more returning gas is getting entrained and thus, higher temperatures appear. The opposite applies for the right side. So the expected temperature should be slightly lower than the shown experimental data on the left side and slightly higher of the right side. This observation applies for all the temperature plots above this position.

Considering this observation, it appears that the the GRI-Mech 3.0 model slightly underpredicts the bulk flow temperature and the centerline temperature by approximately 25 K. On the other hand, the KEE58 model seems to better predict the centerline temperature, while it overpredicts the bulk flow temperature.

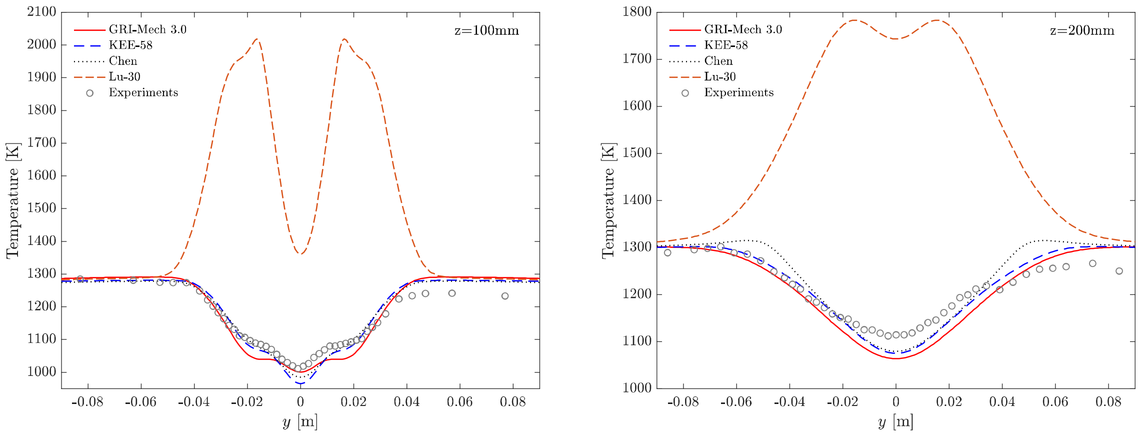

(a) $z = 100$ mm **(b)** $z = 200$ mm

Figure 4.13: Mean Temperature profile comparison of different chemistry mechanisms for $z = 100, 200$ mm.

The automatically reduced model created by Chen cannot capture the temperature profile in the mixing region mentioned above. The peak difference between this model and the experimental results is approximately 100 K. Nonetheless, it is the only model that accurately predicts the centerline temperature.

In Figure 4.14b the automatically reduced model is unable to capture the shape of the tempature profile. The mixing region is overpredicted by 200 K and the the centerline by 50 K. At this point it is safe to conclude that this mechanism is also unable to capture the MILD combustion process of this furnace. Moreover, big discrepancies are starting to arise between the KEE58 and the GRI-Mech mechanisms that up to this point were more or less more able to accurately capture the profile. The KEE58 mechanisms appears to overpredict the bulk flow temperature by 25 K, while on the other hand the GRI-Mech is under predicting it by 25 K (considering the tilt of the profile. Both mechanism are also underpredicting the centerline temperature.

Lastly, the temperatures for $z =$ 500 mm are presented in Figure 4.14c. In this case, the GRI-Mech 3.0 is able to capture the shape of the experimental temperature profile, however it underpredicts it by an average of approximately 90 K. On the other hand, the KEE58 fails to capture the shape of the profile and overpredicts it in the bulk region by 50 K and underpredicts it in the centerline region by 75 K.

According to the observations of Huang et al [95] who conducted these experiments, autoignition kernels were appearing along all heights. These kernels were detected by the measuring the chemiluminescense intensity of OH from $z = 300$ mm to $z =$578 mm. Moreover, it was reported that the stabilized flames that usually appear in the Jet in Hot Coflow flames were not present in the main reaction zone where the chemiluminescense is the highest. Intense narrow reaction zones were not observed in the main reaction zone either.

There are two explanations offered for these two observations. At first, the flame fronts are being streched by the large scale vortices generated by the high speed jets. Secondly, in this furnace a propagating flame cannot survive since the

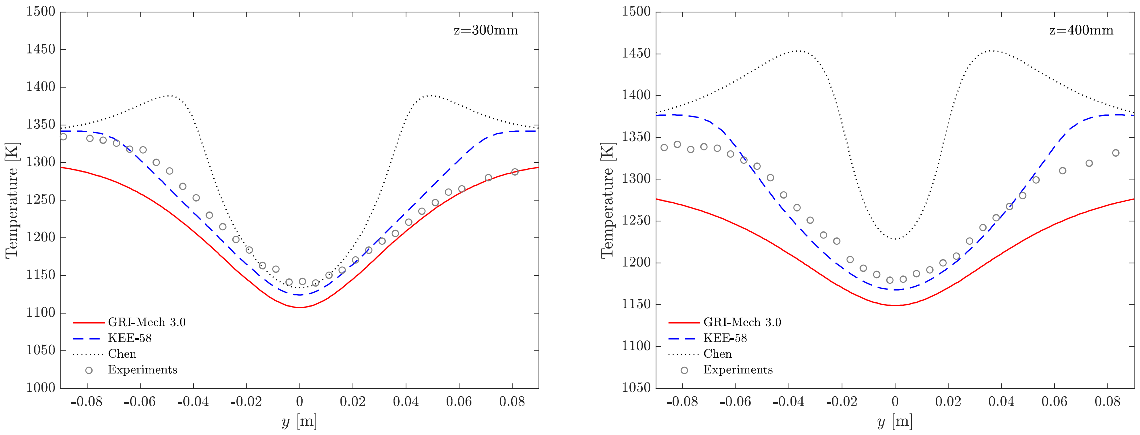

(a) $z = 300$ mm **(b)** $z = 400$ mm

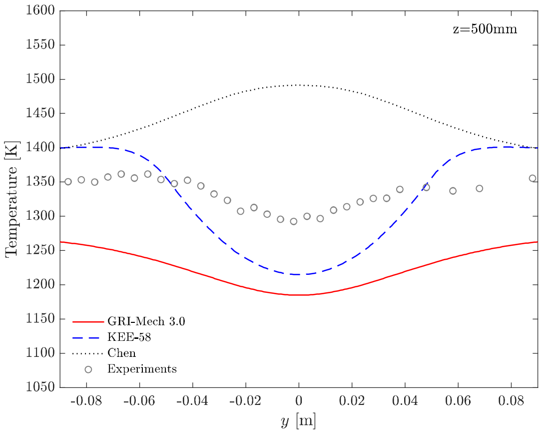

(c) $z = 500$ mm

Figure 4.14: Mean Temperature profile comparison of different chemistry mechanisms for $z = 300, 400, 500$ mm.

mixing is too dynamic to allow a stabilized flame that is continuously fed by fuel and air. Therefore, autoignition of fresh mixture dominates the start of the reactions. This autoignition behaviour should be translated in RANS modeling as wide spread reactions in the domain, while reactions should not happen in the recirculation phase.

Though the GRI model predicts lower temperatures overall, it was selected as the most suitable model based on three reasons. Firstly, it is the only one of the tested models that was able to accurately capture the shape of the temperature profile in the entirety of the domain, albeit at lower temperatures overall. Secondly, it is the only model that resembles what can be expected from widespread presence of ignition kernels, which suggest autoignition is taking place. Finally, since the next modeling target is the radiative heat transfer modeling, the overall temperature is expected to increase overall due to better radiative heat transfer. This mechanism is the only one that leaves room for this increase without severely overpredicting the bulk flow temperature. Moreover, Fortunato et al [101] also predicted the best results with the GRI-3.0. Additionally, Ferranotti et al [103] suggested the GRI-

Mech 3.0 for flameless furnaces with approximately 1300 K. The work of Sabia et al [74], can propably illuminate the reason the GRI-Mech 3.0 predicts lower temperatures overall. In this work auto-ignition delay was reported for the GRI-Mech, compared to other mechanisms.

THE GRI-MECH 3.0 CHEMISTRY MECHANISM

In this section the temperature profiles of the GRI-Mech 3.0 detailed mechanism will be presented for the different values of the volume fraction constant C_ξ. Moreover, a reduced GRI-Mech 3.0 scheme without the NOx reactions, will be added, since it will be used instead of the standard GRI-Mech 3.0 model due to limitations in ANSYS Fluent that will be described in the next section.

In Figure 4.15 the temperature profiles for $z = 100$, 300, 400, 500 mm are presented. As it can be seen in Figure 4.15a, for all the models except for the case with $C_\xi = 3$ there is no visible difference. For $C_\xi = 3$ the model slightly underestimated the entirety of the profile by a few degrees. For a distance of $z = 300$m from the burner, again the difference is almost indistinguishable. Again for $C_\xi = 3$ the bulk flow temperature is slightly overestimated compared to the the other models. This trend continues in Figure 4.15c. The GRI-$C_\xi = 3$ model overpredicts the bulk flow temperature by about 25 K. Another difference in this case is that the slope of the model is larger, since all models estimate the same temperature in the centerline region. Lastly, in Figure 4.15d the entirety of the domain is overestimated compared to the other models. Moreover in this distance, the shape of the profile is not captured that well. However, all these differences can be considered small compared to the differences the other chemistry mechanism exhibit.

There observations coincide with the initial qualitative estimation, that in the GRI-Mech 3.0 mechanism the change in C_ξ does not produce any significant differences in the temperature. While any of the aforementioned constants could be used for the simulations, the default value was selected. Lewandowski et al [39] and Ertesvag et al [38] argue that modified EDC constants may lead to inconsistencies with the turbulence models. They also argue that most of the inconsistencies that are reported in literature, stem from the fact that the research was based on the deviating implementation in Ansys Fluent, which in particular presents notable effects at low turbulent Reynolds numbers and thus, in combustion regimes such in MILD combustion. In this case this effect is not important since in the main combustion region the turbulent Reynolds number is higher than the limit of 65 is the limit denoted by De et al [7]. A contour of the turbulent Reynolds numbers of the computational domain with the final selected models is presented in Appendix C.

Additionally, the contours of the standard and reduced GRI-Mech 3.0 mechanisms are presented in order to evaluate the temperatures and the reaction regions in the entirety of the domain (Figure 4.16). As it can be observed, both the temperature and the formylradical field are identical, as expected from the previous findings. Therefore, the reduced mechanism can be used instead of the standard one for the next investigation.

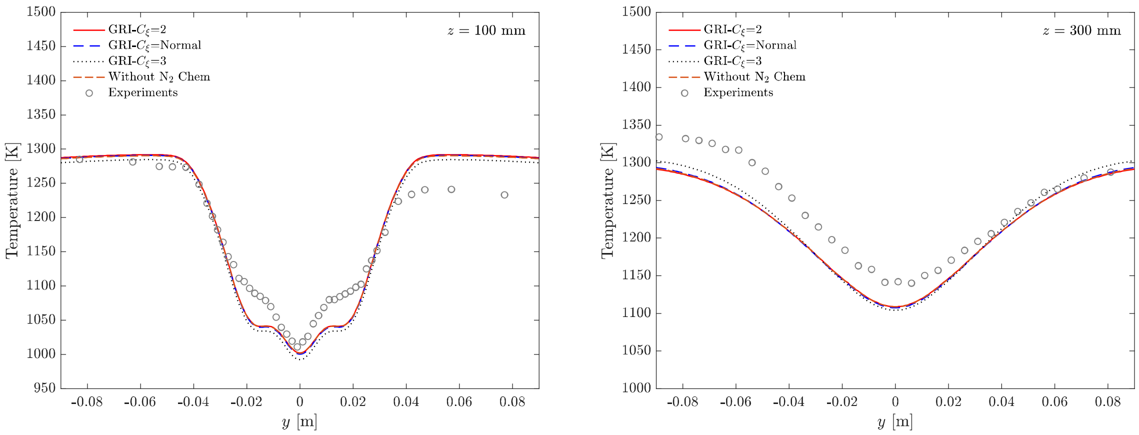

(a) z =100 mm **(b)** z =300 mm

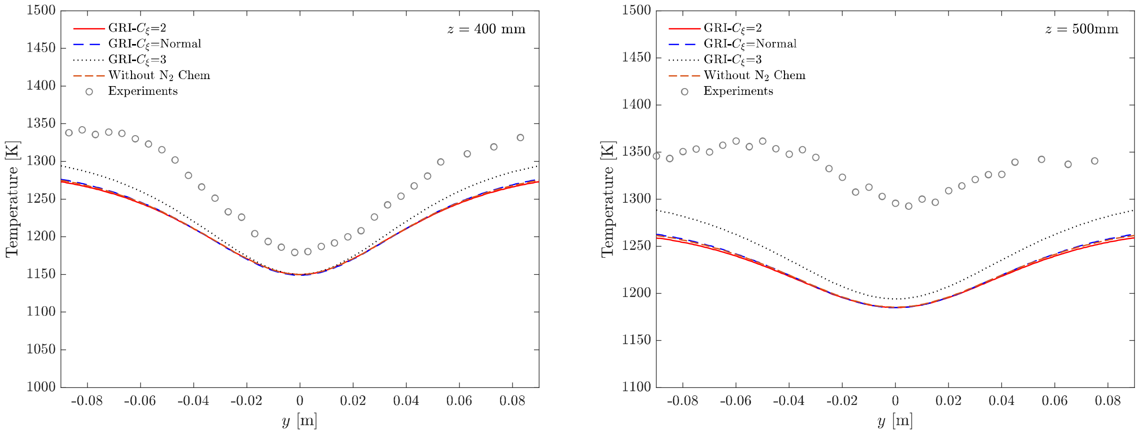

(c) z =400 mm **(d)** z =500 mm

Figure 4.15: Mean Temperature profile comparison of the GRI-Mech models for z =100, 300, 400, 500 mm.

4.3.3. INFLUENCE OF RADIATION MODELING

In this section the effect of the different radiative gas properties models will be investigated. In literature, most researchers either neglect the radiation modeling, [51], [115], [117], [118], or use simple models such as the 1-RTE WSGG formulation ANSYS Fluent provides, [43], [90], [96], [102], [104], [114], [119]. Christo et al [104] on his work on the unconfined JHC flames, concluded that the inclusion of thermal radiation in the model does not play a significant role. However, in his work it was also stated that radiation should be included for modeling MILD combustion in confined furnaces, since radiative heat transfer between the flame and the walls can have a large effect on flow and flame characteristics.

However, no research has been conducted in order to evaluate the impact of using different models to calculate the gas radiative properties. For this reason, a radiative gas properties modeling study was conducted using the standard domain-based WSGG, a 4-RTE domain-based WSGG (4 grey gases), a 5-RTE (5 grey gases) SLW model with tabulated ALBDF data and a cell-based WSGG, in which the gas layer

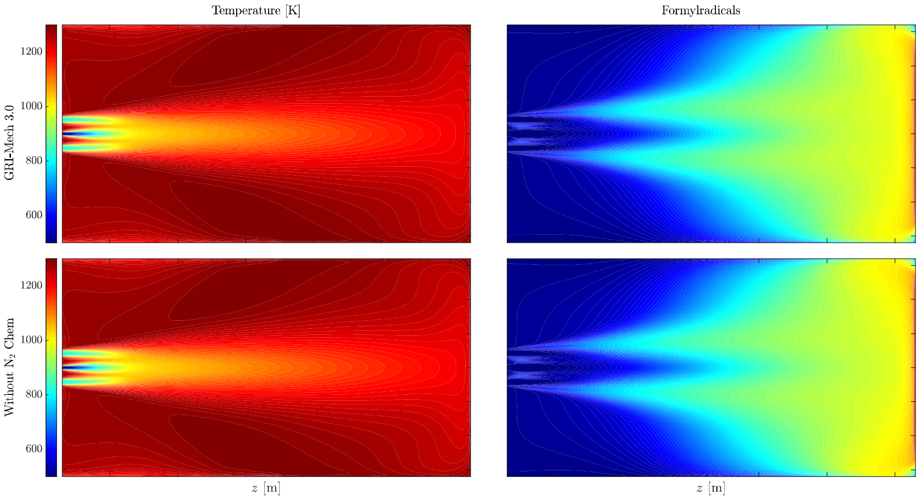

Figure 4.16: Temperature and Formylradicals contours of the standard and reduced GRI-Mech 3.0.

of thickness s is provided by the average length of the cells. In order to effectively conduct this investigation the turbulence and chemistry models must remain constant for all cases. Based on the previous discussion, the standard $k-\varepsilon$ will be used as a turbulence model. The turbulence chemistry interaction will be modeled using the EDC model with the normal constants. Lastly, the GRI-Mech 3.0 model will be used to model the chemistry mechanism. In order to evaluate the influence of radiation modeling, the contours of the temperature and the formylradicals will be presented and discussed. Afterwards, the temperature profiles that are predicted by the different models are compared with the experimental data that were measured.

During the implementation of the radiative gas properties models, it was noticed that the SLW model and the 4-RTE domain-based WSGG cannot be coupled with the GRI-Mech in ANSYS Fluent. ANSYS Fluent cannot model the spectral properties of more than 50 species and it results in segmentation errors due to improper memory allocations. However, since it was already established that the GRI model is the best of the researched models to simulate the chemistry mechanism, another approach was decided. GRI-Mech 3.0 has a total of 53 species that are modeled. Moreover, it includes detailed N_2 chemistry in order to calculate NO formation. Since what is of interest, in order to evaluate the importance of radiation modeling, is the calculation of the temperature profile, and additionally the NOx formations in MILD combustion is low, the reduction of the GRI-Mech 3.0 was decided by removing the N_2 chemistry but of course keeping the N_2 as inert species. This results in a 36 species mechanism with 217 chemical reactions. A similar approach was reported by Fortunato et al [75].

In Figure 4.17 the contours of the temperature and the formylradicals are presented. As it can be observed from the contours, the modeling of the radiative gas properties does not seem to affect the temperature. Only in the case of the single RTE domain based WSGG the temperature is slightly lower towards the end of the domain. On the other hand, radiation seems to slighly affect the reaction zones represented by the formylradicals contours. In the case of the single RTE WSGG model the reaction zone is slightly bigger and there are more reactions happening toward the end and the sides of the domain. The 4 RTE WSGG and the SLW models appear to obtain similar results, whereas for the cell based method (CB), there are less reactions happening in the centerline region.

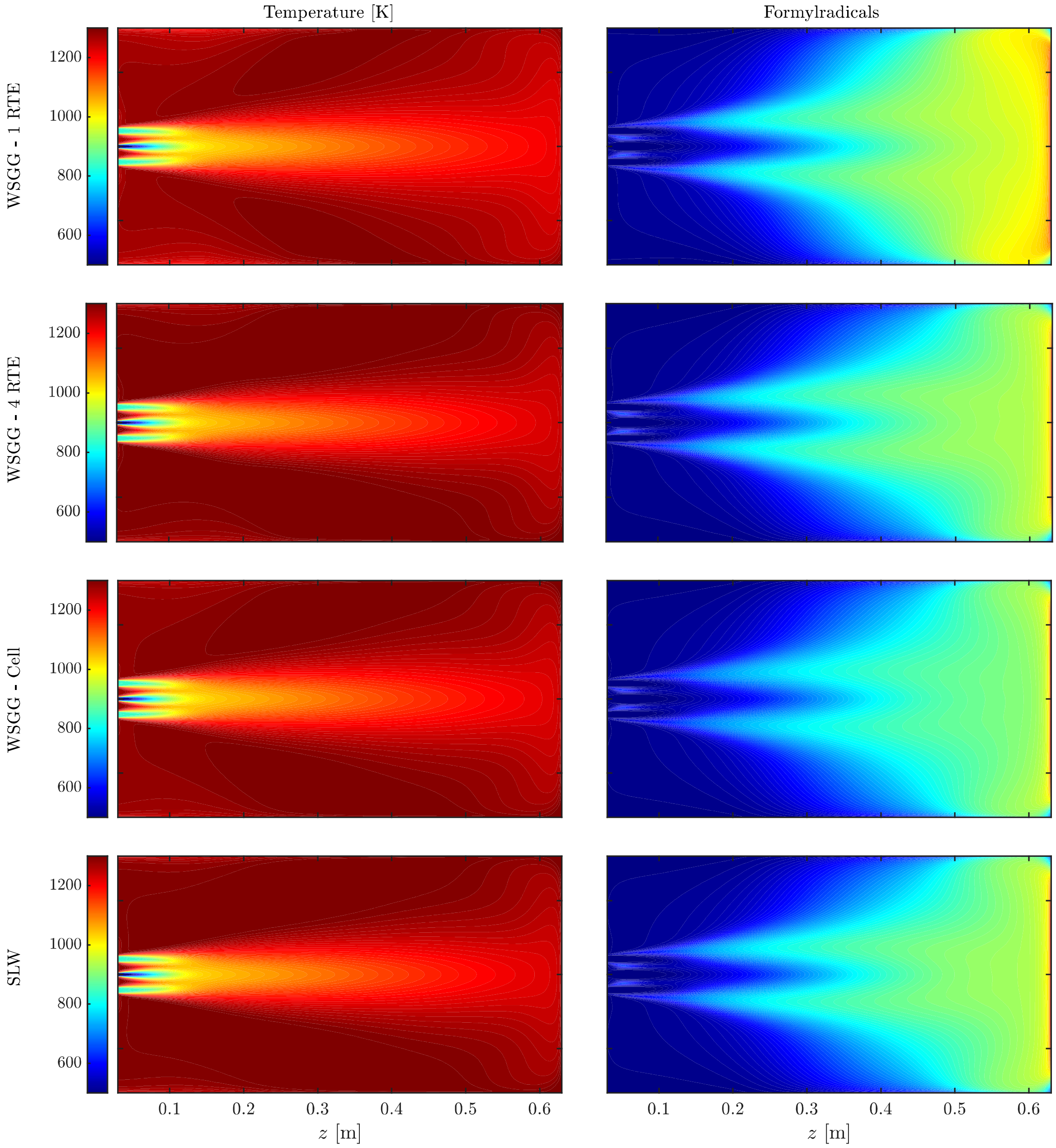

Figure 4.17: Temperature and Formylradicals Contours using the 4 different radiation models.

In Figures 4.18, 4.19 the mean temperature profiles for $z =$ 100 and 200 mm, as well as 300, 400 and 500 mm are presented. In the first Figure, it can be observed that the 4 RTE WSGG and the SLW models predict similar profiles. Both models seem to overpredict the temperature in the bulk flow region by approximately 30 K. However, both models appear to more accurately predict the temperature near the centerline region. The 1 RTE WSGG model is predicting the same profile however, it is shifted to lower temperatures overall. While it predicts more accurately the temperature in the bulk flow region, it underpredicts it in the centerline region. The CB method results stand in between the other models. It appears to capture the bulk flow temperatures better than the 4 RTE WSGG and the SLW models and also capture the centerline region better than the 1 RTE WSGG. Lastly, it must be noted that all models fail to accurately predict the temperature in the mixing region however the maximum difference is 25 K which can again be considered very small.

In Figure 4.18b the mean temperature profile for $z = 200$ mm is presented. All models appear to overpredict the bulk flow region temperature by a few degrees. The SLW model calculates the highest bulk flow temperature overall and the 1 RTE WSGG the lowest. The same trend as before is observed concerning the centerline region. Here, all models underpredict it, with the SLW model by 30 K and the 1 RTE WSGG by almost 50 K. The CB method again seems like a reasonable compromise between the more detailed SLW model and the simple 1 RTE WSGG. Compared to the 1 RTE WSGG model, it calculated a slightly higher temperature in the bulk flow and a few degrees lower than the SLW in the centerline region.

Here it must be noted that more detailed models calculate higher temperatures overall. That can be explained by the "flattening" effect of the added radiative heat transfer mentioned in Chapter 3.3.1. More rigorous radiation treatment, results in more even distrubution of heat in the entirety of the domain.

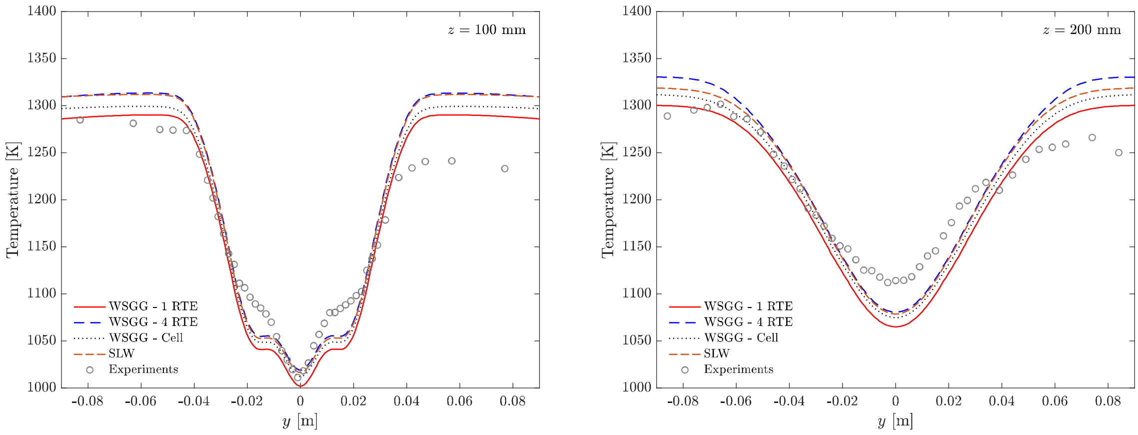

(a) z =100 mm **(b)** z =200 mm

Figure 4.18: Mean Temperature profile comparison of radiation models for z =100, 200 mm.

In Figure 4.19a, the 4 RTE WSGG and CB models appear to be able to accurately capture the bulk flow temperature, considering the tilt of the profile due to the inflow imbalance. The SLW slighly overpredicts it, while the 1 RTE WSGG slighlty underpredicts it. While all the models capture the shape of the profile, they also slightly underpredict the centerline temperature by a few degrees, with the 1

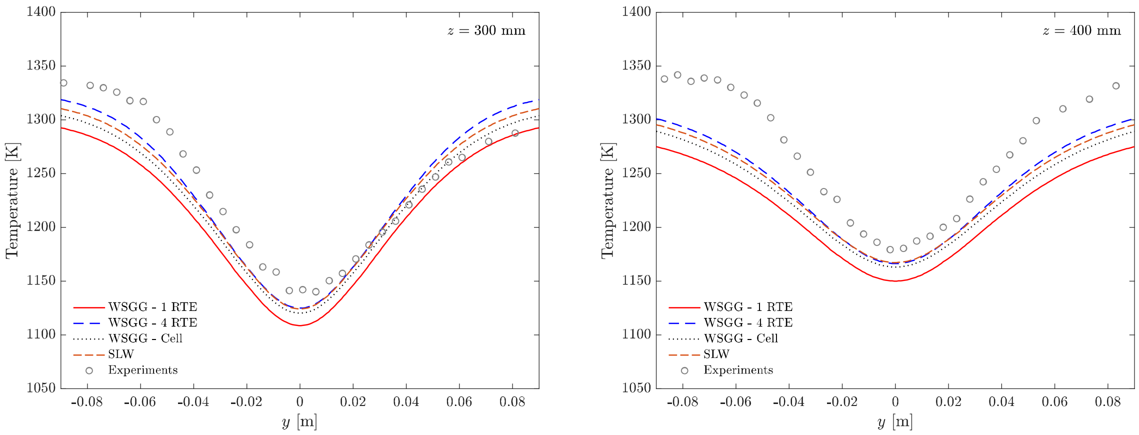

(a) z =300 mm **(b)** z =400 mm

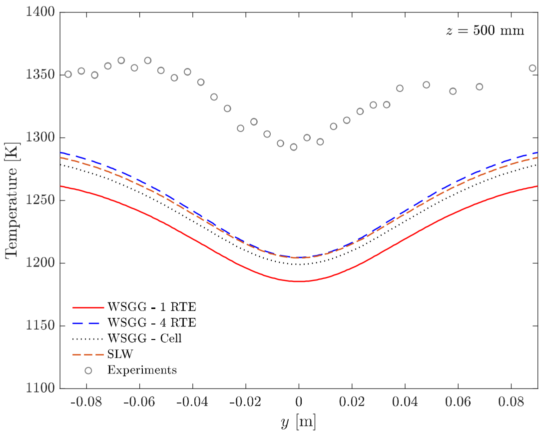

(c) z =500 mm

Figure 4.19: Mean Temperature profile comparison of radiation models for z =300, 400, 500 mm.

RTE WSGG underpredicting it by approximately 30 K.

In Figure 4.19b, the temperature profile for $z = 400$ is presented. In this case, all radiation models underpredict the overall temperature in all the regions. The SLW, 4 RTE WSGG and CB models slightly underpredict the centerline temperature by approximately 10 K, whereas the 1 RTE WSGG by 30 K. Moreover, SLW, 4 RTE WSGG and CB are underpredicting the bulk flow temperature by 40, 45, 50 K respectively, whereas the 1 RTE-WSGG by 75 K. This in turn results in less steep slove in the shape of the calculated profiles.

Lastly, the temperature profile for $z = 500$ is presented (Figure 4.19c). Here, all the models underpredict the temperature profile by approximately more than 70 K. In the case of the 1-RTE WSGG the average difference is 100 K. Again, SLW, 4 RTE WSGG and CB models calculate similar temperatures in the entirety of the profile with the maximun difference between the SLW model and the CB model being less 10 K.

As it is evident from all the calculated temperature profiles, more rigorous treatment of radiation leads to the overall increase of the temperature in the entirety of this case's domain. However, the differences between model predictions and the experiments is larger than the differences between the various models. Only the 1 RTE WSGG stands out, as it displays the worst predictions in the reaction region of the domain. Overall, sometimes the models overpredict and sometimes they underpredict. It cannot be concluded that a particular model agrees more with experiments than the others. Since that is the case, the simplest model should be used, in order to lower the computational costs. Therefore, for the simulation of this furnace the Cell based WSGG is suggested. However, it must be noted that the cell based method is extremely sensitive to the cell size, so extreme care must be given in the creation of the mesh of the domain. Lastly, since the Cell-Based model was selected NO mass fractions can be calculated by using the complete GRI-Mech 3.0. The resulting NO mass fractios are presented in Appendix D.

Nonetheless, the consideration of using a more detailed radiation is important. The discrepancy in the predictions between the different radiation models is larger than the discrepancies observed between different EDC models (E-EDC, NE-EDC) [44], [45]. This could be explained based on the fact that in the EDC models the calculated differences are local, due to the role of local Reynolds and Damkohler number, whereas in the radiation models the calculated differences are because of differences in mean temperature in large regions.

5

CONCLUSIONS AND RECOMMENDATIONS

5.1. CONCLUSIONS

In the present work, a comprehensive comparative study of different radiation, turbulence and chemistry models has been performed. This study was conducted in two steps. Firstly, the importance of radiative heat transfer in furnaces was investigated with the use of advanced radiation models, by simulating an axisymmetric oxy-combustion furnace. Secondly, based on the results of the first step, a detailed numerical simulation of a MILD combustion lab-scale furnace was conducted, with the objective of evaluating different turbulence, chemistry and radiation models and their influence on MILD combustion simulations.

5.1.1. AXISYMMETRIC OXY-COMBUSTION FURNACE

In the study conducted for the case of the axisymmetric furnace, three radiatives gas properties models are evaluated, based on experimental data and data extracted from the work of Webb et al [86]. The effects of the domain-based WSGG, cell-based WSGG and a 10-RTE SLW model on the temperature profiles, the species mole fractions and the radiative heat source are compared. From these comparisons the following can be concluded:

- Firstly, it is shown that more detailed radiative gas properties modeling plays a significant role in the distribution of heat in the bulk region of the computational domain. The simulation of the radiative gas properties is important and directly influences the resulting temperature field.
- Moreover, it is observed that more detailed radiation treatment can alter the temperatures in the flame region. This is especially pronounced in the

regions with high temperatures where near stoichiometric combustion takes place. Thus, it can be expected that these differences will influence the chemical structure or the flame coherence when more complex detailed chemistry mechanisms are used.

- Additionally, the CO_2 and H_2O concentrations in this case are not affected by the more detailed radiation modeling. This is evident by the fact that, even in the extreme scenario of not treating radiation at all, the resulting concentrations are nearly identical.

- Finally, higher absorption coefficients directly impact the volumetric radiative heat source, especially in the combustion region. This also highlights the importance of rigorous treatment of the radiative transfer, particularly around the flame region.

Based on these observations, detailed radiation treatment is suggested in MILD combustion, since calculating the recirculatory bulk flow temperature in this regime is very important. Also, differences in temperatures in this regime mainly exist in the reaction zone and thus, detailed chemistry mechanisms may be affected. Moreover, better radiation treatment leads to more even heat distribution, which is a key aspect of MILD combustion in general.

5.1.2. FLAMELESS COMBUSTION FURNACE

Simulations are made of a natural gas fired lab-scale furnace which operates in the MILD combustion regime. In numerous RANS simulations, different radiation, turbulence and chemistry models are compared in order to accurately model the MILD combustion process.

- Firstly, the turbulence models are compared. The Standard, Modified Standard, Realizable $k-\varepsilon$ and $k-\omega$ SST turbulence models are compared based on velocity measurements. The modified standard and the realizable $k-\varepsilon$ fail to predict the velocity correctly. The standard $k-\varepsilon$ and the $k-\omega$ SST are both good fits for both velocity and temperature, but ultimately the standard $k-\varepsilon$ is selected based on literature.

- The eddy dissipation concept coupled with various different chemistry mechanisms is considered. The effect of changing the model constant C_ξ on the reaction zones of the GRI-Mech 3.0, the DRM-19, the KEE58 and Chen mechanisms is investigated qualitatively, based on the formylradicals concentration. The DRM-19 fails to capture the processes in this furnace. The GRI-Mech 3.0, the KEE58, Chen and Lu-30 are compared based on CARS measurements. Both the GRI-Mech 3.0 and the KEE58 produce satisfactory results up to a point but finally, the GRI-Mech 3.0 is selected.

- Lastly, the influence of the radiative gas property model is investigated using the standard 1-RTE domain-based WSGG, a 4-RTE WSGG, a cell-based

WSGG and the SLW model. The comparison is done based on temperature measurements. WSGG performs significantly worse than the other models. All the other radiative properties models can improve the result of the simulation. The Cell-based WSGG is selected due to lower computational cost.

The resulting combination of the standard $k-\varepsilon$ model for turbulence, EDC with the normal C_ξ constant coupled with the GRI-Mech 3.0 and the Cell-based WSGG model agrees to a satisfactory degree with the experiments in the MILD combustion furnace. This model is the result of rigorous and multi-variable analysis of many possible sources of uncertainties.

5.2. RECOMMENDATIONS

After presenting and discussing the obtained results and the working procedure that was followed in this project, a set of recommendations can be proposed to improve the final results in both cases that were evaluated.

For the Axisymmetric Oxy-Combustion Furnace:

- Since this case was only used in order to assess the influence of the radiation models, simple chemistry and turbulence models were employed. Thus, the results do not agree with experimental data. A reassessment of the choice of those models could potentially significantly impact the results.
- The Cell-based method is very sensitive to the input cell size. A study on the impact of different meshes and thus, different cell sizes on the Cell-based model could prove its robustness and reliability in order to be used in other cases as well.

For the Flameless Combustion Furnace:

- The correct specification of boundary conditions is essential in any numerical simulation. In this case, the biggest uncertainty is related to the side wall boundary condition. A modification of the wall temperature within a reasonable range and the assessment of its influence on the final solution is therefore suggested.
- The combination of the standard $k-\varepsilon$ model for turbulence, EDC with the normal C_ξ constant coupled with the GRI-Mech 3.0 and the Cell-based WSGG model can satisfactorily predict the MILD combustion process in this furnace. However, it should be further investigated whether it can predict similar results in different flameless combustion furnaces or different operating conditions (i.e. different burner configuration, different recirculation ratios)
- The EDC model is a rather simple approach to model the TCI interactions. Another model that is able to take into account finite-rate chemistry is the PaSR model. The combination of PaSR model with the GRI-Mech 3.0 showed

promising results [101]. Therefore, a study based on the PaSR model can be conducted.

- Finally, the modeling of turbulence radiation interaction could be added. The inclusion of TRI will result in the dampening of the fluctuations in the temperature field. Since the temperature of the flow is high, and in the recirculating region there is a high concentration of water vapour and CO_2, a reduction the heat flux mixing at least in the beginning of the flow is expected. This can lead to delays in the reactions, and thus directly influence the simulations results. A turbulence radiation interaction model that can be applied in the RANS framework was recently developed by Silvestri et al [120].

BIBLIOGRAPHY

[1] International Energy Agency. *Key world energy statistics*. International Energy Agency Paris, 2007.

[2] Dieter Helm. “The future of fossil fuels—is it the end?” In: *Oxford Review of Economic Policy* 32.2 (2016), pp. 191–205.

[3] Paris Agreement. “Paris agreement”. In: *Report of the Conference of the Parties to the United Nations Framework Convention on Climate Change (21st Session, 2015: Paris). Retrived December*. Vol. 4. HeinOnline. 2015, p. 2017.

[4] André AV Perpignan, Arvind Gangoli Rao, and Dirk JEM Roekaerts. “Flameless combustion and its potential towards gas turbines”. In: *Progress in Energy and Combustion Science* 69 (2018), pp. 28–62.

[5] JA Wünning and JG Wünning. “Flameless oxidation to reduce thermal NO-formation”. In: *Progress in energy and combustion science* 23.1 (1997), pp. 81–94.

[6] Masashi Katsuki and Toshiaki Hasegawa. “The science and technology of combustion in highly preheated air”. In: *Symposium (International) on combustion*. Vol. 27. 2. Elsevier. 1998, pp. 3135–3146.

[7] M De Joannon et al. “Mild combustion: Process features and technological constrains”. In: *Combustion science and technology* 153.1 (2000), pp. 33–50.

[8] Sudarshan Kumar, PJ Paul, and HS Mukunda. “Studies on a new high-intensity low-emission burner”. In: *Proceedings of the combustion institute* 29.1 (2002), pp. 1131–1137.

[9] PengFei Li et al. “Progress and recent trend in MILD combustion”. In: *Science China Technological Sciences* 54.2 (2011), pp. 255–269.

[10] X Huang, MJ Tummers, and DJEM Roekaerts. “Experimental and numerical study of MILD combustion in a lab-scale furnace”. In: *Energy Procedia* 120 (2017), pp. 395–402.

[11] Thierry Poinsot and Denis Veynante. *Theoretical and numerical combustion*. RT Edwards, Inc., 2005.

[12] Kenneth K Kuo. *Principles of combustion*. TJ254. 5 K85 2005. 2005.

[13] Jurgen Warnatz et al. *Combustion*. Springer, 2006.

[14] Anthony F Mills. *Basic heat and mass transfer*. Prentice hall, 1999.

[15] Michael F Modest. *Radiative heat transfer*. Academic press, 2013.

[16] Yunus Cengel. *Heat and mass transfer: fundamentals and applications*. McGraw-Hill Higher Education, 2014.

[17] D.J.E.M Roekaerts. *Lecture notes in Combustion for Propulsion and Power Systems*. Mar. 2019.

[18] Vladimir P Solovjov, Brent W Webb, and Frédéric André. "Radiative properties of gases". In: *Handbook of thermal science and engineering* 2 (2017), 1069e1142.

[19] Michael F Modest and Daniel C Haworth. *Radiative heat transfer in turbulent combustion systems: theory and applications*. Springer, 2016.

[20] Simone Hochgreb. "Mind the gap: Turbulent combustion model validation and future needs". In: *Proceedings of the Combustion Institute* 37.2 (2019), pp. 2091–2107.

[21] ANSYS FLUENT User Guide. "Release 14.0, ANSYS". In: *Inc., USA, November* (2011).

[22] Warren C Strahle and Subhash BS Chandran. "Pressure-velocity correlation in a reactive turbulent flow". In: *AIAA Journal* 20.1 (1982), pp. 129–135.

[23] Stephen B Pope. *Turbulent flows*. 2001.

[24] B. Launder et al. "Prediction of free shear flows: A comparison of the performance of six turbulence models". In: 1972.

[25] B.E. Launder and D.B. Spalding. "The numerical computation of turbulent flows". In: *Computer Methods in Applied Mechanics and Engineering* 3.2 (1974), pp. 269–289. DOI: `10.1016/0045-7825(74)90029-2`.

[26] JJ McGuirk and W Rodi. "The calculation of three-dimensional turbulent free jets". In: *Turbulent Shear Flows I*. Springer, 1979, pp. 71–83.

[27] BB Dally, DF Fletcher, and AR Masri. "Flow and mixing fields of turbulent bluff-body jets and flames". In: *Combustion Theory and Modelling* 2.2 (1998), pp. 193–219.

[28] SB Pope. "An explanation of the turbulent round-jet/plane-jet anomaly". In: *AIAA journal* 16.3 (1978), pp. 279–281.

[29] Tsan-Hsing Shih et al. "A new $k-\varepsilon$ eddy viscosity model for high reynolds number turbulent flows". In: *Computers & fluids* 24.3 (1995), pp. 227–238.

[30] Tsan-Hsing Shih. *A realizable Reynolds stress algebraic equation model*. Vol. 105993. Lewis Research Center, Institute for Computational Mechanics in Propulsion, 1993.

[31] David C Wilcox. "Reassessment of the scale-determining equation for advanced turbulence models". In: *AIAA journal* 26.11 (1988), pp. 1299–1310.

[32] David C Wilcox et al. *Turbulence modeling for CFD*. Vol. 2. DCW industries La Canada, CA, 1998.

[33] Florian R Menter. "Zonal two equation kw turbulence models for aerodynamic flows". In: *23rd fluid dynamics, plasmadynamics, and lasers conference*. 1993, p. 2906.

[34] Florian R Menter. "Two-equation eddy-viscosity turbulence models for engineering applications". In: *AIAA journal* 32.8 (1994), pp. 1598–1605.

[35] Bjørn F Magnussen and Bjørn H Hjertager. “On mathematical modeling of turbulent combustion with special emphasis on soot formation and combustion”. In: *Symposium (international) on Combustion*. Vol. 16. 1. Elsevier. 1977, pp. 719–729.

[36] B Magnussen. “On the structure of turbulence and a generalized eddy dissipation concept for chemical reaction in turbulent flow”. In: *19th aerospace sciences meeting*. 1981, p. 42.

[37] Ashoke De et al. “Numerical simulation of delft-jet-in-hot-coflow (djhc) flames using the eddy dissipation concept model for turbulence–chemistry interaction”. In: *Flow, Turbulence and Combustion* 87.4 (2011), pp. 537–567.

[38] Ivar S Ertesvåg. “Analysis of some recently proposed modifications to the Eddy Dissipation Concept (EDC)”. In: *Combustion Science and Technology* 192.6 (2020), pp. 1108–1136.

[39] Michał T Lewandowski and Ivar S Ertesvåg. “Analysis of the Eddy Dissipation Concept formulation for MILD combustion modelling”. In: *Fuel* 224 (2018), pp. 687–700.

[40] Markus Bösenhofer et al. “The eddy dissipation Concept—Analysis of different fine structure treatments for classical combustion”. In: *Energies* 11.7 (2018), p. 1902.

[41] Ivar S Ertesvåg and Bjørn F Magnussen. “The eddy dissipation turbulence energy cascade model”. In: *Combustion science and technology* 159.1 (2000), pp. 213–235.

[42] Inge R Gran and Bjørn F Magnussen. “A numerical study of a bluff-body stabilized diffusion flame. Part 2. Influence of combustion modeling and finite-rate chemistry”. In: *Combustion Science and Technology* 119.1-6 (1996), pp. 191–217.

[43] Alessandro Parente et al. “Extension of the Eddy Dissipation Concept for turbulence/chemistry interactions to MILD combustion”. In: *Fuel* 163 (2016), pp. 98–111.

[44] Hesheng Bao. “Development and validation of a new eddy dissipation concept (EDC) model for MILD combustion”. In: (2017).

[45] Naiara Romero-Anton et al. “New extended eddy dissipation concept model for flameless combustion in furnaces”. In: *Combustion and Flame* 220 (2020), pp. 49–62.

[46] Marco Mehl et al. “Kinetic modeling of gasoline surrogate components and mixtures under engine conditions”. In: *Proceedings of the Combustion Institute* 33.1 (2011), pp. 193–200.

[47] Tarek Echekki and Epaminondas Mastorakos. *Turbulent combustion modeling: Advances, new trends and perspectives*. Vol. 95. Springer Science & Business Media, 2010.

[48] WP Jones and RP Lindstedt. “Global reaction schemes for hydrocarbon combustion”. In: *Combustion and flame* 73.3 (1988), pp. 233–249.

[49] Benedetta Franzelli et al. “Large eddy simulation of combustion instabilities in a lean partially premixed swirled flame”. In: *Combustion and flame* 159.2 (2012), pp. 621–637.

[50] Jicang Si et al. “Optimization of the Global Reaction Mechanism for MILD Combustion of Methane Using Artificial Neural Network”. In: *Energy & Fuels* 34.3 (2020), pp. 3805–3815.

[51] Ju Pyo Kim, Uwe Schnell, and Gunter Scheffknecht. “Comparison of different global reaction mechanisms for MILD combustion of natural gas”. In: *Combustion Science and Technology* 180.4 (2008), pp. 565–592.

[52] Feifei Wang et al. “A refined global reaction mechanism for modeling coal combustion under moderate or intense low-oxygen dilution condition”. In: *Energy* 157 (2018), pp. 764–777.

[53] G P. Smith. *GRI-Mech 3.0 Mechanism*. URL: `http://combustion.berkeley.edu/gri-mech/version30/%5C%5C%20text30.html` (visited on 10/07/2020).

[54] M Frenklach et al. “GRI-Mech—an optimized detailed chemical reaction mechanism for methane combustion”. In: *Gas Research Institute Topical Report No. GRI-95/0058* (1995).

[55] C.T. Bowman. *GRI-Mech 2.11 Mechanism*. URL: `http://combustion.berkeley.edu/gri-mech/new21/version21/text21.html` (visited on 10/07/2020).

[56] A. Kazakov and M. Frenklach. *DRM-19 Mechanism*. URL: `http://www.me.berkeley.edu/drm/` (visited on 10/07/2020).

[57] Tim WJ Peeters. “Numerical modeling of turbulent natural gas diffusion flames.” PhD thesis. 1997.

[58] Tianfeng Lu and Chung K Law. “Toward accommodating realistic fuel chemistry in large-scale computations”. In: *Progress in Energy and Combustion Science* 35.2 (2009), pp. 192–215.

[59] Yulin Chen and Jyh-Yuan Chen. “Towards improved automatic chemical kinetic model reduction regarding ignition delays and flame speeds”. In: *Combustion and Flame* 190 (2018), pp. 293–301.

[60] Tianfeng Lu and Chung K Law. “A criterion based on computational singular perturbation for the identification of quasi steady state species: A reduced mechanism for methane oxidation with NO chemistry”. In: *Combustion and Flame* 154.4 (2008), pp. 761–774.

[61] Mitchell D Smoke and Vincent Giovangigli. “Formulation of the premixed and nonpremixed test problems”. In: *Reduced kinetic mechanisms and asymptotic approximations for methane-air flames*. Springer, 1991, pp. 1–28.

[62] RW Bilger, SH Starner, and RJ Kee. “On reduced mechanisms for methanefixme air combustion in nonpremixed flames”. In: *Combustion and Flame* 80.2 (1990), pp. 135–149.

[63] Luc Vervisch and Roekaerts Dirk. *ERCOFTAC Best Practice Guidelines" Computational Fluid Dynamics of Turbulent Combustion"*. 2015.

[64] Thomas Christen, Frank Kassubek, and Rudolf Gati. “Radiative heat transfer and effective transport coefficients”. In: *Heat Transfer-Mathematical Modelling, Numerical Methods and Information Technology* (2011).

[65] Michael F. Modest. “The weighted-sum-of-gray-gases model for arbitrary solution methods in radiative transfer”. In: *Journal of Heat Transfer (Transactions of the ASME (American Society of Mechanical Engineers), Series C); (United States)* 113.3 (1991).

[66] MK Denison and BW Webb. “Spectral line-based weighted-sum-of-gray-gases model for arbitrary RTE solvers”. In: *Journal of Heat Transfer (Transactions of the ASME (American Society of Mechanical Engineers), Series C); (United States)* 115.4 (1993).

[67] J Meulemans. “An assessment of some non-gray global radiation models in enclosures”. In: *Journal of Physics: Conference Series*. Vol. 676. 2016, p. 012017.

[68] Jean Taine and Anouar Soufiani. “Gas IR radiative properties: from spectroscopic data to approximate models”. In: *Advances in heat transfer*. Vol. 33. Elsevier, 1999, pp. 295–414.

[69] Hoyt Clarke Hottel and Adel F Sarofim. *Radiative transfer*. McGraw-Hill, 1967.

[70] TF Smith, ZF Shen, and JN Friedman. “Evaluation of coefficients for the weighted sum of gray gases model”. In: (1982).

[71] A Coppalle and P Vervisch. “The total emissivities of high-temperature flames”. In: *Combustion and Flame* 49.1-3 (1983), pp. 101–108.

[72] Martin K Denison and Brent W Webb. “An absorption-line blackbody distribution function for efficient calculation of total gas radiative transfer”. In: *Journal of Quantitative Spectroscopy and Radiative Transfer* 50.5 (1993), pp. 499–510.

[73] Martin K Denison and Brent W Webb. “The spectral-line weighted-sum-of-gray-gases model for H 2 O/CO 2 mixtures”. In: *Journal of heat transfer* 117.3 (1995), pp. 788–792.

[74] Pino Sabia et al. “Modeling Negative Temperature Coefficient region in methane oxidation”. In: *Fuel* 91.1 (2012), pp. 238–245.

[75] Valentina Fortunato et al. “Influence of modelling and scenario uncertainties on the numerical simulation of a semi-industrial flameless furnace”. In: *Applied thermal engineering* 76 (2015), pp. 324–334.

[76] A Soufiani and E Djavdan. “A comparison between weighted sum of gray gases and statistical narrow-band radiation models for combustion applications”. In: *Combustion and Flame* 97.2 (1994), pp. 240–250.

[77] PD Nguyen et al. “Application of the Spectral Line-based Weighted-Sum-of-Gray-Gases model (SLWSGG) to the calculation of radiative heat transfer in steel reheating furnaces firing on low heating value gases”. In: *Journal of Physics: Conference Series*. Vol. 369. 1. IOP Publishing. 2012, p. 012008.

[78] Chungen Yin et al. “New weighted sum of gray gases model applicable to computational fluid dynamics (CFD) modeling of oxy- fuel combustion: derivation, validation, and implementation”. In: *Energy & Fuels* 24.12 (2010), pp. 6275–6282.

[79] Narayanan Krishnamurthy, PJ Paul, and Wlodzimierz Blasiak. “Studies on low-intensity oxy-fuel burner”. In: *Proceedings of the Combustion Institute* 32.2 (2009), pp. 3139–3146.

[80] Gautham Krishnamoorthy et al. “Radiation modelling in oxy-fuel combustion scenarios”. In: *International Journal of Computational Fluid Dynamics* 24.3-4 (2010), pp. 69–82.

[81] R Porter et al. “Evaluation of solution methods for radiative heat transfer in gaseous oxy-fuel combustion environments”. In: *Journal of Quantitative Spectroscopy and Radiative Transfer* 111.14 (2010), pp. 2084–2094.

[82] Huaqiang Chu et al. “Calculations of radiative heat transfer in an axisymmetric jet diffusion flame at elevated pressures using different gas radiation models”. In: *Journal of Quantitative Spectroscopy and Radiative Transfer* 197 (2017), pp. 12–25.

[83] Klas Andersson et al. “Radiation intensity of propane-fired oxy-fuel flames: implications for soot formation”. In: *Energy & Fuels* 22.3 (2008), pp. 1535–1541.

[84] Stefan hjartstam et al. “Computational fluid dynamics modeling of oxy-fuel flames: the role of soot and gas radiation”. In: *Energy & fuels* 26.5 (2012), pp. 2786–2797.

[85] Adrian Gunnarsson. “Experimental and numerical studies of thermal radiation in gas, coal and co-fired pilot test facilities”. In: (2017).

[86] BW Webb et al. “SLW modeling of radiation transfer in comprehensive combustion predictions”. In: *Combustion Science and Technology* 190.8 (2018), pp. 1392–1408.

[87] J Badger, BW Webb, and VP Solovjov. “An exploration of advanced SLW modeling approaches in comprehensive combustion predictions”. In: *Combustion Science and Technology* (2019), pp. 1–17.

[88] HK Kim et al. “Studies on combustion characteristics and flame length of turbulent oxy- fuel flames”. In: *Energy & fuels* 21.3 (2007), pp. 1459–1467.

[89] E Oldenhof et al. “Role of entrainment in the stabilisation of jet-in-hot-coflow flames”. In: *Combustion and Flame* 158.8 (2011), pp. 1553–1563.

[90] J Aminian et al. “Key modeling issues in prediction of minor species in diluted-preheated combustion conditions”. In: *Applied Thermal Engineering* 31.16 (2011), pp. 3287–3300.

[91] Wojciech P Adamczyk et al. “CFD modeling and thermodynamic analysis of a concept of a MILD-OXY combustion large scale pulverized coal boiler”. In: *Energy* 140 (2017), pp. 1305–1315.

[92] Wang Lin, Liu Zhaohui, and Richard L Axelbaum. “Numerical Analysis of Mild Combustion Regimes Under Air and Oxyfuel Conditions”. In: *ASME Power Conference*. Vol. 57601. American Society of Mechanical Engineers. 2017.

[93] Weihong Yang and Wlodzimierz Blasiak. “Flame entrainments induced by a turbulent reacting jet using high-temperature and oxygen-deficient oxidizers”. In: *Energy & fuels* 19.4 (2005), pp. 1473–1483.

[94] HK Kim et al. “NO reduction in 0.03–0.2 MW oxy-fuel combustor using flue gas recirculation technology”. In: *Proceedings of the combustion institute* 31.2 (2007), pp. 3377–3384.

[95] X Huang. “Measurements and model development for flameless combustion in a lab-scale furnace”. PhD thesis. Delft University of Technology, 2018.

[96] M Graça et al. “Numerical simulation of a reversed flow small-scale combustor”. In: *Fuel Processing Technology* 107 (2013), pp. 126–137.

[97] A Rebola, PJ Coelho, and M Costa. “Assessment of the performance of several turbulence and combustion models in the numerical simulation of a flameless combustor”. In: *Combustion Science and Technology* 185.4 (2013), pp. 600–626.

[98] Chiara Galletti, Alessandro Parente, and Leonardo Tognotti. “Numerical and experimental investigation of a mild combustion burner”. In: *Combustion and flame* 151.4 (2007), pp. 649–664.

[99] P Li et al. “MILD combustion under different premixing patterns and characteristics of the reaction regime”. In: *Energy & fuels* 28.3 (2014), pp. 2211–2226.

[100] D LUPANT* et al. “Numerical and experimental characterization of a self-regenerative flameless oxidation burner operation in a pilot-scale furnace”. In: *Combustion Science and Technology* 179.1-2 (2007), pp. 437–453.

[101] Valentina Fortunato et al. “Experimental and numerical investigation of a MILD combustion chamber for micro gas turbine applications”. In: *Energies* 11.12 (2018), p. 3363.

[102] A Chinnici, GJ Nathan, and BB Dally. “Experimental and numerical study of the influence of syngas composition on the performance and stability of a laboratory-scale MILD combustor”. In: *Experimental Thermal and Fluid Science* 115 (2020), p. 110083.

[103] Marco Ferrarotti et al. “Key modeling aspects in the simulation of a quasi-industrial 20 kW moderate or intense low-oxygen dilution combustion chamber”. In: *Energy & fuels* 32.10 (2018), pp. 10228–10241.

[104] F C Christo and Bassam B Dally. “Modeling turbulent reacting jets issuing into a hot and diluted coflow”. In: *Combustion and flame* 142.1-2 (2005), pp. 117–129.

[105] A Habibi, Bart Merci, and Geraldine J Heynderickx. “Impact of radiation models in CFD simulations of steam cracking furnaces”. In: *Computers & Chemical Engineering* 31.11 (2007), pp. 1389–1406.

[106] Guzide Ozen and Nevin Selçuk. “SLW model for computational fluid dynamics modeling of combustion systems: Implementation and validation”. In: *Numerical Heat Transfer, Part B: Fundamentals* 70.1 (2016), pp. 47–55.

[107] X Huang, MJ Tummers, and DJEM Roekaerts. “Modeling of MILD combustion in a lab-scale furnace with an extended FGM model including turbulence-radiation interaction”. In: *Combustion and Flame* Submitted for publication ().

[108] Ishmail B Celik et al. “Procedure for estimation and reporting of uncertainty due to discretization in CFD applications”. In: *Journal of fluids Engineering-Transactions of the ASME* 130.7 (2008).

[109] Yl Hardalupas and M Orain. “Local measurements of the time-dependent heat release rate and equivalence ratio using chemiluminescent emission from a flame”. In: *Combustion and Flame* 139.3 (2004), pp. 188–207.

[110] Robert L Gordon et al. “Transport budgets in turbulent lifted flames of methane autoigniting in a vitiated co-flow”. In: *Combustion and Flame* 151.3 (2007), pp. 495–511.

[111] Paul R Medwell, Peter AM Kalt, and Bassam B Dally. “Simultaneous imaging of OH, formaldehyde, and temperature of turbulent nonpremixed jet flames in a heated and diluted coflow”. In: *Combustion and Flame* 148.1-2 (2007), pp. 48–61.

[112] Robert L Gordon et al. “A numerical study of auto-ignition in turbulent lifted flames issuing into a vitiated co-flow”. In: *Combustion Theory and Modelling* 11.3 (2007), pp. 351–376.

[113] M Rehm, P Seifert, and B Meyer. “Theoretical and numerical investigation on the EDC-model for turbulence–chemistry interaction at gasification conditions”. In: *Computers & Chemical Engineering* 33.2 (2009), pp. 402–407.

[114] Javad Aminian et al. “Numerical investigation of a MILD combustion burner: analysis of mixing field, chemical kinetics and turbulence-chemistry interaction”. In: *Flow, turbulence and combustion* 88.4 (2012), pp. 597–623.

[115] MJ Evans, PR Medwell, and ZF Tian. “Modeling lifted jet flames in a heated coflow using an optimized eddy dissipation concept model”. In: *Combustion Science and Technology* 187.7 (2015), pp. 1093–1109.

[116] MJ Evans et al. “Generalisation of the eddy-dissipation concept for jet flames with low turbulence and low Damköhler number”. In: *Proceedings of the Combustion Institute* 37.4 (2019), pp. 4497–4505.

[117] Marco Mancini, Roman Weber, and Ugo Bollettini. “Predicting NOx emissions of a burner operated in flameless oxidation mode”. In: *Proceedings of the combustion institute* 29.1 (2002), pp. 1155–1163.

[118] Amir Mardani, Sadegh Tabejamaat, and Mohsen Ghamari. “Numerical study of influence of molecular diffusion in the Mild combustion regime”. In: *Combustion Theory and Modelling* 14.5 (2010), pp. 747–774.

[119] Alessio Frassoldati et al. “Kinetic and fluid dynamics modeling of methane / hydrogen jet flames in diluted coflow”. In: *Applied Thermal Engineering* 30.4 (2010), pp. 376–383.

[120] Simone Silvestri, Dirk Roekaerts, and Rene Pecnik. “Modeling turbulent heat transfer accounting for turbulence-radiation interactions.” In: *Heat Fluid Flow* (2020).

A

AXISYMMETRIC FURNACE VELOCITY PLOTS

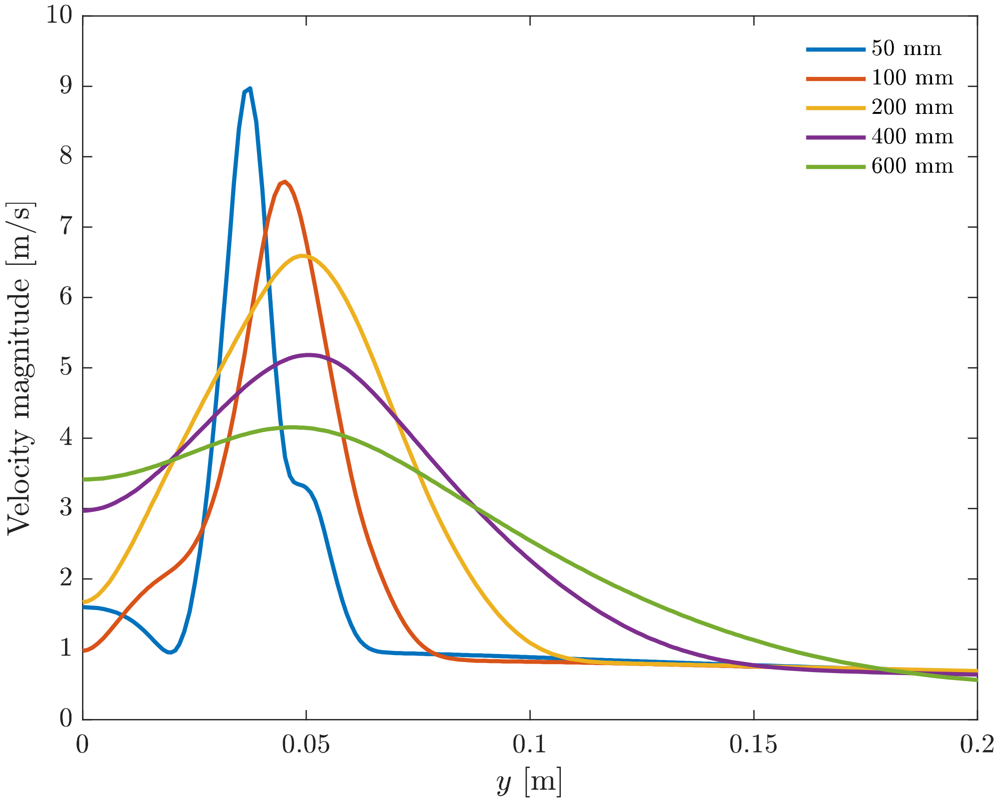

Figure A.1: Velocity magnitude near the burner using the domain based WSGG model.

B

CASES

Table B.1: List of cases required for this study.

ID	Turbulence Model	C_ξ	Chemistry Mechanism	Radiation model
1	Standard $k-\varepsilon$	2.1377	GRI-Mech 3.0	Domain based WSGG
2	Modified $k-\varepsilon$	2.1377	GRI-Mech 3.0	Domain based WSGG
3	Realizable $k-\varepsilon$	2.1377	GRI-Mech 3.0	Domain based WSGG
4	$k-\omega$ SST	2.1377	GRI-Mech 3.0	Domain based WSGG
5	Standard $k-\varepsilon$	2	GRI-Mech 3.0	Domain based WSGG
6	Standard $k-\varepsilon$	3	GRI-Mech 3.0	Domain based WSGG
7	Standard $k-\varepsilon$	2	KEE58	Domain based WSGG
8	Standard $k-\varepsilon$	2.1377	KEE58	Domain based WSGG
9	Standard $k-\varepsilon$	3	KEE58	Domain based WSGG
10	Standard $k-\varepsilon$	2	Chen	Domain based WSGG
11	Standard $k-\varepsilon$	2.1377	Chen	Domain based WSGG
12	Standard $k-\varepsilon$	3	Chen	Domain based WSGG
13	Standard $k-\varepsilon$	2	DRM-19	Domain based WSGG
14	Standard $k-\varepsilon$	2.1377	DRM-19	Domain based WSGG
15	Standard $k-\varepsilon$	3	DRM-19	Domain based WSGG
16	Standard $k-\varepsilon$	2.1377	Lu-30	Domain based WSGG
17	Standard $k-\varepsilon$	2.1377	GRI-Mech 3.0 - Reduced	Domain based WSGG
18	Standard $k-\varepsilon$	2.1377	GRI-Mech 3.0 - Reduced	Cell based WSGG
19	Standard $k-\varepsilon$	2.1377	GRI-Mech 3.0 - Reduced	4-RTE WSGG
20	Standard $k-\varepsilon$	2.1377	GRI-Mech 3.0 - Reduced	SLW

C

TURBULENT REYNOLDS OF LAB-SCALE FURNACE

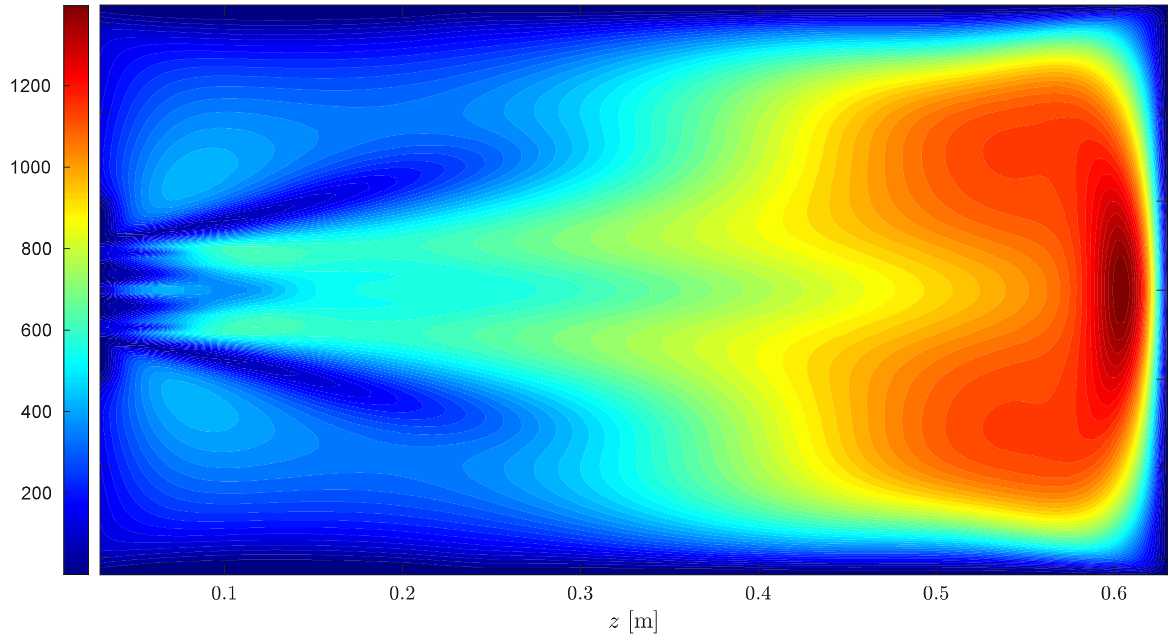

Figure C.1: Turbulent Reynolds Number for the case with the standard $k-\varepsilon$ model, standard EDC with GRI-Mech 3.0 and cell based WSGG.

D

NO EMISSIONS OF LABSCALE FURNACE

The NO concentrations dominate the NOx emissions in this case. In Figure D.1 the NO volume fraction is presented. It can be seen that everywhere the NO magnitude is no higher than approximately 0.4 ppm.

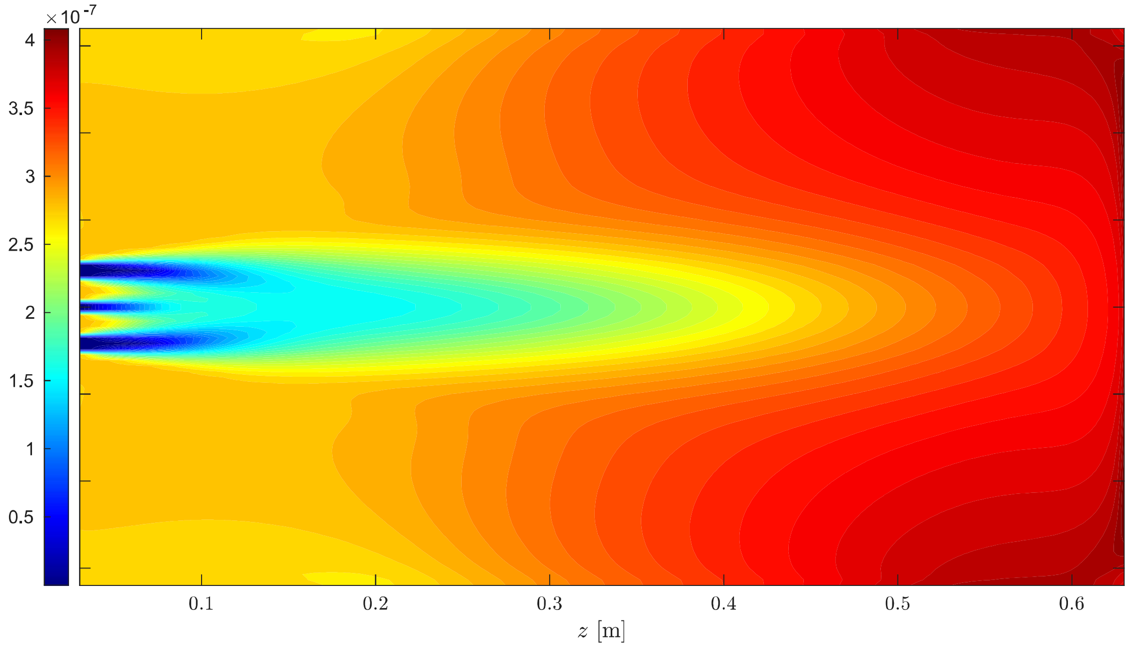

Figure D.1: NO volume fraction for the case with the standard $k-\varepsilon$ model, standard EDC with GRI-Mech 3.0 and cell based WSGG.